Investigation of Interfacial Contact Condition during Resistance Spot Welding of Automobile Sheet Steel

Graz University of Technology
Institute for Materials Science and Welding

Matthew Galler

Abstract

The electrical contact resistance at the electrode/sheet and sheet/sheet interfaces was investigated in this dissertation for zinc coated and uncoated automobile sheet steels using both experimental and numerical approaches. A new, in-situ experimental measurement method was proposed to evaluate the electrical contact resistance as a function of welding current. These experimental results were used in a numerical optimization procedure with the finite element modeling commercial software SYSWELD to numerically estimate the interface temperature in a stepwise approach. The main results of this work provided new electrical contact resistance curves as a function of interface temperature which could be used as input parameter in a resistance spot welding simulation to improve the accuracy of process models.

This dissertation was divided into four different chapters. The first chapter was a literature overview of the resistance spot welding process including all of the process, material, and metallurgical variables that have an influence on the weld quality in terms of size and strength. Also, a brief overview of the zinc coatings processes and the problem of electrode wear when welding zinc coated automobile steels was provided since much of the pertinent resistance spot welding research, including that of the project sponsors of this work, focuses on advancing knowledge in this topic to improve the efficiency of the welding process. It was determined the electrical contact resistance was the parameter which had the most influence on the heat generation during welding, weld quality, and electrode wear. Therefore, a main focus of this chapter was the introduction of the concept of electrical contact resistance as well as the current research challenges facing the resistance spot welding scientific community in this respect. Specifically, the shape of the electrical contact resistance curve as a function of temperature was discussed here in detail, as well as different methods for measuring this parameter. It was determined that a large demand exists in this field for an all encompassing technique to measure the electrical contact resistance during actual welding as a function of interface temperature.

In the second chapter, the newly proposed technique to experimentally measure the electrical contact resistance as a function of welding current using total resistance measurements in the welding electrodes was introduced. This technique included important process modifications such as single sheet experiments with very low welding current and one period of low current application. The purpose of the process modifications was to keep the bulk temperature as low as possible in order to reduce the bulk material resistance contribution in the

total resistance values so that the electrical contact resistance curve shape could be investigated. The total resistance curve shape was found to be very sensitive to the welding force value as well as the material/coating being analyzed. With lower welding forces, the curve was found to have a decreasing nature. As the welding force increased, the electrical contact resistance curve flattened and, in some cases, even increased. A peak was also found in the total resistance curve for DP600-copper and low carbon steel-copper contacts. The total resistance curve for zinc coated steel-copper contact had an increasing nature.

In the third chapter, the experimental measurement technique was validated with the finite element modeling program SYSWELD. In order to validate this measurement technique, the input electrical contact resistance and bulk material resistance curves were numerically manipulated in the simulation program. The purpose in doing this was to determine at which current values the bulk material resistance played a role in the total resistance measurements, and on the other hand in which current range the electrical contact resistance could be measured without the influence of bulk material resistance. As the welding current increased, the bulk material resistance contribution was found to play a role in the measurement. With the help of the numerical simulation, a low current range was found in that the electrical contact resistance curve shape could be experimentally measured with this technique. It was also determined that the electrical contact resistance for galvanized and electrogalvanized coated steels at the electrode/sheet interface was negligible. Additionally, the input SYSWELD electrical contact resistance curves were found to be significantly inaccurate with regards to their shape and values.

The fourth and final chapter was the numerical determination of the contact interface temperature at the electrode/sheet and sheet/sheet interface using a numerical optimization procedure. Specifically, the finite element method was used to calculate, in a stepwise manner, the interface temperature in the simulation which allowed for good matching between numerical and experimental total resistance values. Additionally, the contribution of the electrical contact resistance and the bulk material resistance was numerically separated from the total resistance value to assist in the technique. Due to its complexity and possibilities for future applications, the optimization procedure was described in this chapter in detail. The newly created electrical contact resistance curves as a function of temperature were presented and compared to literature

for accuracy and validity. The procedure could be implemented in the future for all material and coating combinations.

Kurzfassung

Im Rahmen der vorliegenden Dissertation wird der elektrische Kontaktwiderstand der Elektroden/Blech und der Blech/Blech Oberflächen von verzinkten und blanken Automobilstählen mittels experimentellen und numerischen Verfahren untersucht. Eine neue Messmethode wird vorgeschlagen: Der elektrische Kontaktwiderstand wird während des Schweißprozesses gemessen. Im Zuge dieser Messmethode wird die Finite Element Methode mit der Software SYSWELD verwendet, um die Temperatur der Kontaktoberfläche zu kalkulieren. Die Hauptergebnisse dieser Arbeit sind neue elektrische Kontaktwiderstandskurven als Funktion der Temperatur für verschieden verzinkte sowie blanke Automobilstähle. Diese Kurven können in weiterer Folge in einer Widerstandspunktschweißsimulation verwendet werden, um die thermischen und mechanischen Ergebnisse zu verbessern.

Mit diesem Vorhaben beschäftigt sich diese Dissertation in vier Kapiteln. Das erste Kapitel umfasst eine Literaturrecherche, in der die wichtigsten Prozesse, Materialien und metallurgischen Einflüsse auf die Schweißpunktqualität – Punktdurchmesser und Schmelzzonenform – diskutiert werden. Des weitern beschäftigt sich dieses Kapitel mit verschiedenen Zinkbeschichtungen und deren Einfluss auf den Elektrodenverschleiß. Im Zuge dieser Literaturrecherche stellte sich heraus, dass der elektrische Kontaktwiderstand der wichtigste Parameter für die Wärmeeinbringung, die Schweißpunktqualität und den Elektrodenverschleiß darstellt. Daher befasst sich ein großer Teil dieses Kapitals mit der Vorstellung dieses Konzeptes, sowie die hauptsächlichen Schwierigkeiten um dieses Thema. Gerade die Form der elektrischen Kontaktwiderstandskurven als Funktion der Temperatur wurden in der letzten Zeit intensiv diskutiert, sowie verschiedene Messmethoden, um diese Parameter genau zu bestimmen.

In dem zweiten Kapital wird eine experimentelle Messmethode vorgestellt, in der der Gesamtwiderstand zwischen zwei Elektroden als Funktion des Schweißstroms gemessen wird. Das Ziel dieser Methode ist die genaue Bestimmung der Form der Kontaktwiderstandskurve während des Schweißprozesses. Diese Messmethode hat folgende Vorteile: Erstens werden Einzelblechversuche durchgeführt, um den Kontaktwiderstand an der Elektroden/Blech

Oberfläche genau zu messen. Zweitens wird ein niedriger Schweißstrom verwendet, um den Stoffwiderstand während des Messens so niedrig wie möglich zu halten. Es wird herausgefunden, dass die Schweißkraft auf die Form der Kurve einen wesentlichen Einfluss hat: Eine Steigerung der Schweißkraft bewirkt eine ansteigende Kurve, eine Verringerung derselben eine abfallende Kurve. Während des Messvorgangs von DP600 Stahl und weichem Stahl wird ein Höhepunkt der Widerstandskurve festgestellt. Außerdem ist das Ergebnis des Messens des zinkbeschichteten Stahls eine ständig ansteigende Kurve.

Das dritte Kapital beschäftigt sich mit dem Überprüfen der experimentellen Messmethode unter der Verwendung des Simulationsprogramms SYSWELD, um herauszufinden, in welchem Strombereich der Kontaktwiderstand und ab welchem Stromwert der Stoffwiderstand dominiert. Je höher der Stromwert, desto mehr spielt der Stoffwiderstand in den Messungen eine Rolle. Es wird herausgefunden, dass die vorgeschlagene Messmethode die genaue Form der Kontaktwiderstandskurve in einem niedrigen Strombereich zeigt. Weiters ist der Kontaktwiderstand an der Elektroden/Blech Oberfläche für feuerverzinkten Stahl zu vernachlässigen.

Das vierte und abschließende Kapitel beschäftigt sich mit den Ergebnissen der Kalkulation der Kontaktoberflächentemperatur für Elektrode/Blech und Blech/Blech. Ein schrittweises numerisches Optimierungsverfahren zur Temperaturberechnung mit dem Programm SYSWELD, wird an dieser Stelle aufgrund seiner Komplexität sehr ausführlich beschrieben. Im Zuge dieses Verfahrens werden neue elektrische Kontaktwiderstandskurven ermittelt, welche mit der einschlägigen Literatur verglichen und in weiterer Folge in einer Simulation verwendet werden. Die oben erwähnte experimentelle Messmethode in Verbindung mit dem numerischen Optimierungsverfahren stellt einen neuen Weg dar, eine elektrische Kontaktwiderstandskurve als Funktion der Temperatur zu ermitteln. Damit kann sowohl die Genauigkeit zukünftiger Simulationen gesteigert, als auch die Effizienz des Schweißprozesses durch die Optimierung von Schweißparametern verbessert werden.

Table of Contents

Chapter 1: Introduction to Resistance Spot Welding: A Literature Overview

1.1 Process overview

Resistance spot welding (RSW) is the principal method for joining sheet metal in the automotive, building, transportation, office furniture and domestic appliance industries. There are many advantages of the RSW process including the ease and speed at which the process can be automated for high production, the high quality of welded joints, and the relative low operating cost. One of the main disadvantages of the process is the difficulty controlling weld nugget formation after a certain number of welds have been produced. The reason for this is the large number of process variables that can influence the heat generation and weld formation.

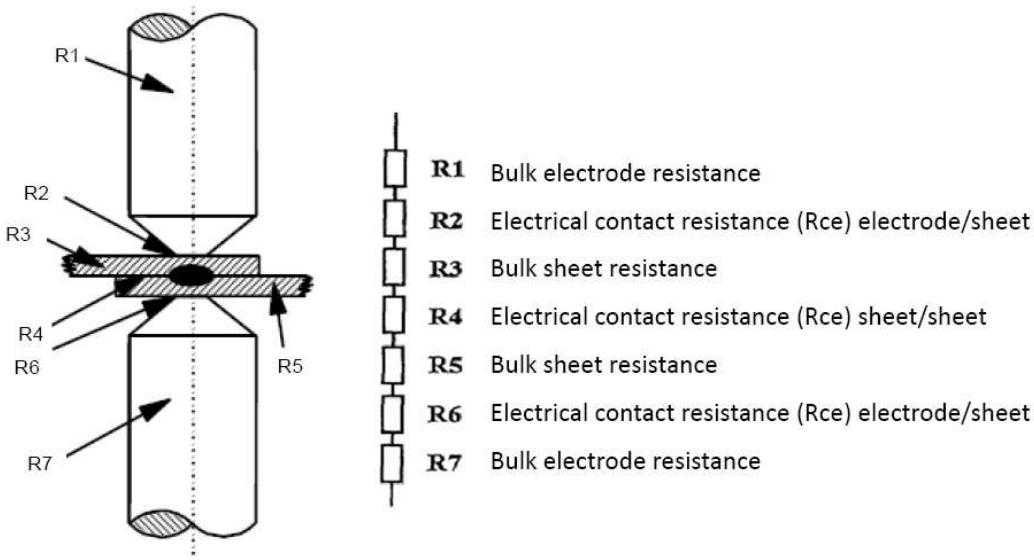

Figure 1.1: Overview of the RSW process with contributing bulk and contact resistances [1].

In RSW, heat is generated by the resistance of parts being welded to the flow of electric current. The total heat production Q (J) comes from Joule heating:

$$Q = I^2 R_{tot} t \tag{1.1}$$

where I is the welding current in ampere, R_{tot} is the total resistance of the contributing resistance values in ohm, and t is the welding time [1-2]. The total resistance is the summation in series of the bulk material resistances of the electrodes and the sheets, and the electrical contact resistance

(Rce) at the electrode/sheet (E/S) and sheet/sheet (S/S) interfaces. An overview of the contributing resistance values is presented in Figure 1.1, where a total of seven different resistances acting in series are shown. The Rce at the S/S interface should be the largest resistance value to ensure melting occurs at this location for the weld to be made between two sheets.

A schematic representation of the RSW process is shown in Figure 1.2 [3]. There are three stages in the process: squeezing, welding, and forging. During the squeezing cycle, two copper alloy electrodes are pressed together against metal sheets with a force around 2.5-3.5 kN. During the welding stage, relatively high currents (7-10 kA) are applied to generate the heat for melting with a welding time of around 20-40 ms. The actual welding current and force values are dependent many variables including the materials being joined, the surface coating, and the thickness of the sheets. When the current application is over, the electrode force still remains during the forging step so water cooled electrodes can provide adequate cooling for the weld.

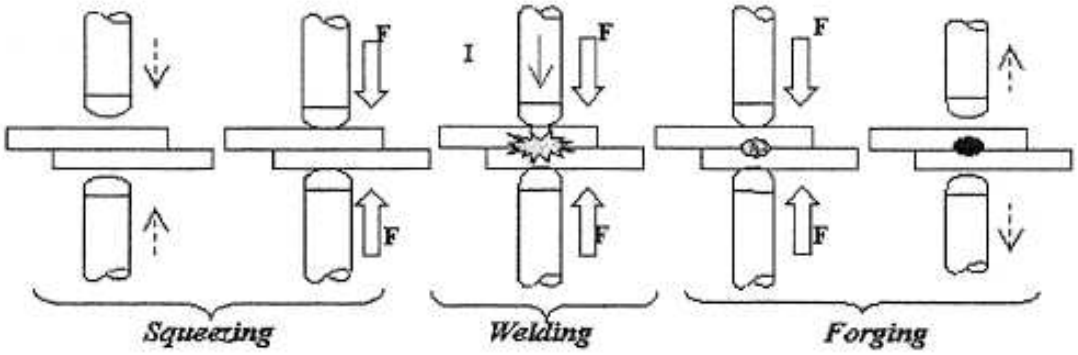

Figure 1.2: Schematic diagram of the 3 stages of the RSW process [3]

1.2 General motivation for resistance spot welding research

The weldability of sheet metal components using the RSW process is of particular interest in the automotive industry, since every car has between 4000-6000 welds in its assembly process [4]. A modern automobile production line produces approximately seven million welds per day. In a well controlled manufacturing operation, more than 99% of these welds would meet the requirements put forth in standards. However, due to the high volumes encountered, a 100% acceptance level is the goal since a rejection rate of even less than 0.1% would represent a large number of defective components. To ensure and maintain the structural integrity of critical

components in an automobile body, the possibility of producing even one defective weld must be eliminated [1].

Recently, there have been severe requirements by car industries to have more corrosion resistant coatings, which increased the use of zinc coatings on steel sheets for corrosion resistance in order to extend product life and improve product quality. Typical zinc coatings used in the automobile industry are galvanized, galvannealed, electrogalvanized, and corrosion protection primer coatings. The presence of zinc on the steel sheet surface has a great influence on the weldability. A pair of spot welding electrodes can manufacture significantly fewer welds in zinc coated steels compared with uncoated steels. Specifically, the presence of a zinc coating results in an accelerated electrode wear rate and a decrease as well as an uncertainty in electrode lifetime. For hot dip galvanized steels, the electrode lives may be as low as 1500 spot welds, compared to the lives in excess of 10,000 welds for bare steels [5]. The mechanisms of electrode wear of zinc coated steel are an important topic with regards to weld formation and quality and will be discussed later in this chapter.

In a high productivity process like RSW, the costs of replacing electrodes and the time associated with changing and or dressing worn electrodes can be very high. Also, the uncertainty in electrode lifetime can lead to the production of weak, undersized welds in critical automotive components, which raises product reliability concerns for automobile manufacturers as well as safety concerns for passengers. It is therefore important for manufacturers to know exactly when the electrode lifetime has expired. This can be very difficult, however, considering the variability and inconsistency in testing results for different sets of materials and zinc coating combinations. Therefore, one of the main motivations for RSW research is the advancement of knowledge for the prevention of undersized welds as well as the prediction of weld size and strength for a certain set of materials being joined throughout the life of a pair of welding electrodes.

Numerical simulation provides a great tool for the optimization of the welding parameters as well as the prediction of thermal, mechanical, and metallurgical aspects of the RSW process. With the help of numerical simulation, understanding the relationship between welding and process variables and electrode degradation is the general focus of this project in order to optimize the production in terms of weld quality and predictability. More specifically, this work focuses on the interfacial contact conditions during the welding of zinc coated automobile steels. The important parameter is the Rce at the E/S and S/S interface. The influence of temperature

and interfacial pressure on the Rce curve was investigated using both experimental and numerical techniques with the assistance of the finite element modeling (FEM) program SYSWELD. The experimental and numerical results of this work will be presented in chapters two, three, and four, while this chapter focuses on a review of the important aspects of the RSW process as well as the impetus for this research.

1.3 Selection of the optimal welding parameters

The procedure for selecting welding parameters (force, time, and current) will now be discussed in order to understand weldability. The resistance spot weldability of automotive sheet steels is characterized by a two dimensional weldability lobe as shown in Figure 1.3 [6]. In order to define a weldability lobe, the current range and weld time must be determined for acceptable weld size at a constant force. From the line *t* (constant time) in Figure 1.3a and starting with a low weld current, the weld diameter is measured for successive increases in welding current. The upper bound for acceptable weld formation is defined by weld nugget splash or expulsion, which is when molten metal bursts out from between the sheets at high welding currents. The lower bound of the current range is defined by the weld diameter. In most cases, an acceptable weld nugget must have a diameter $d \geq 4\sqrt{t}$, where *t* is the thickness of the steel sheet. This procedure is then repeated for a new time t_1, and this leads to the determination of a lobe of acceptable welds in terms of weld time and current value. A material which has good weldability exhibits a large area of the weldability lobe. It is important to note that weld current ranges and weld lobe determination are highly variable and depend on a number of factors which will be described later.

For zinc coated steels, the welding current range is shifted towards higher values for two reasons. More welding current is needed to produce an acceptable weld compared to uncoated steels because the Rce at both the E/S and S/S interfaces for zinc coated steels is lower. Since the resistance is lower, more current is needed for heat production. Also, during the formation of a weld in zinc coated steels, the zinc melts and gets pushed to the edge of the contact diameter, forming a zinc annulus encircling the weld. This annulus shunts some of the current around the weld zone, leaving less current available for weld formation [5].

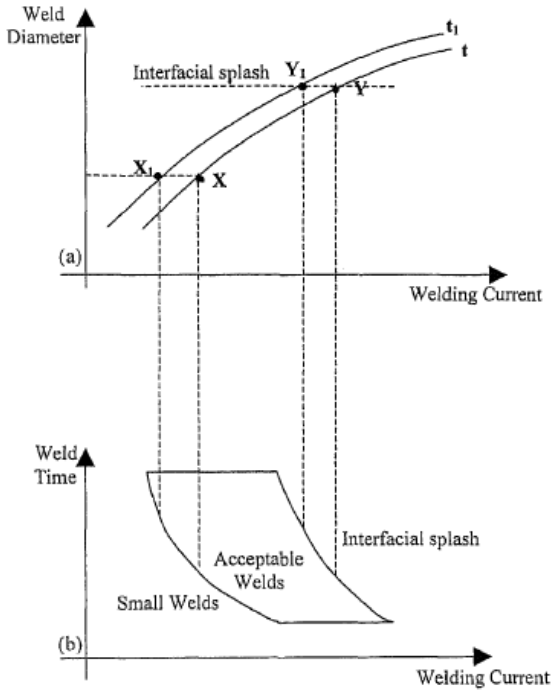

Figure 1.3: a) Weld growth curve for determining welding range in minimum and maximum current. b) Typical weldability lobe for RSW, showing the welding time and current range for acceptable welds [6].

1.4 Zinc coatings for automobile applications

The application of zinc and zinc alloy coatings on a steel surface is one of the most important techniques used to protect steel components from aqueous corrosion. The corrosion resistance of zinc coated steel is improved by two methods: barrier protection and galvanic protection. In barrier protection the zinc coating will first corrode before the corrosive environment reaches the steel. In galvanic protection, zinc is anodic to iron at ambient condition and will sacrificially corrode to protect the steel substrate [7]. Typical processing methods used in producing zinc coatings include hot-dip galvanizing, thermal spraying, and electrodepositing. A brief overview of the three main zinc coatings investigated in this work will now be given.

1.4.1 Hot-dip galvanized coatings

Hot-dip galvanizing of a coiled sheet steel product involves the emersion of steel in a liquid bath of zinc or a zinc alloy using a continuous process. In the continuous hot-dip process, welded coils of steel are coated at speeds of up to 200 m min^{-1}. There are many steps that occur during hot-dip galvanizing, and the processes may differ depending on the hot-dip galvanizing

line. The following discussion is what generally occurs at an industrial hot-dip galvanizing plant. Prior to emersion in the liquid zinc bath, the steel is first cleaned to eliminate any surface oxides and surface carbons that may react in the zinc bath. This is usually accomplished with pickling and brushing operations. The sheets are then put through an annealing furnace in a reducing atmosphere that will reduce organic contaminants and surface oxides and will provide optimal strip entry temperature for the sheets before immersion in a zinc bath. Both horizontal and vertical furnaces are used in this step, and the heating rate, hold times, and final temperatures are important process steps in determining the final coating properties. The steel is then immersed in a zinc bath at a temperature around 450 °C. During this process the zinc begins to react with the steel to form the coating, and many different Fe-Zn and Fe-Al intermetallics can form during dipping. Aluminum is added to the zinc bath for different reasons and is a very important parameter for controlling the microstructure of the coating [7-9]. This will be discussed in further detail in chapter 1.6.2.

There are several reactions taking place at the same time during the dipping stage, including dissolution of steel by the zinc, solidification of Fe-Al-Zn intermetallic compounds, solid state diffusional phase transformation, and solidification of the liquid zinc alloy. All of these transformations are diffusion controlled, and are governed by the diffusion of zinc into the iron substrate, although iron diffuses a bit through the alloy phases at a much slower rate. Typical dipping times range from 4-8 s and vary depending on the speed of the strip and desired microstructure of the strip. Typical zinc coating thicknesses and masses are usually around 200 µm and 150 g m^{-2}, respectively. After hot-dipping, the steel is removed and put through a controlled cooling process or a heat treating process called galvannealing. The bath time, temperature and the bath chemistry are important variables because they affect the metallurgy of the overlay coating and the interfacial layer between the steel and the coating [7-9].

The anatomy of the zinc coating is shown in Figure 1.4 along with the corresponding aluminum distribution in the coating in wt %. At the steel/zinc interface, an interfacial layer of $Fe_2Al_5(Zn)$ is usually present [10]. This layer forms first and prevents any Fe-Zn intermetallic phase formation, thus acting as a so-called inhibition layer. Consequently, this layer has a significant influence on the resistance spot weldability of galvanized steels because it influences the alloying and degradation rate of the electrodes. The presence and thickness of this interfacial layer is very dependent on the aluminum content in the bath. Above the inhibition layer is the

overlay layer, which has a structure consisting of very large grains galled spangles. This layer is made of dendrites of pure zinc eta (η) and appears as a polycrystalline structure. The surface of galvanized coatings has a very small, continuous Al_2O_3 oxide layer around 5 nm in thickness. This layer inhibits further oxidation by acting as a protective barrier [11].

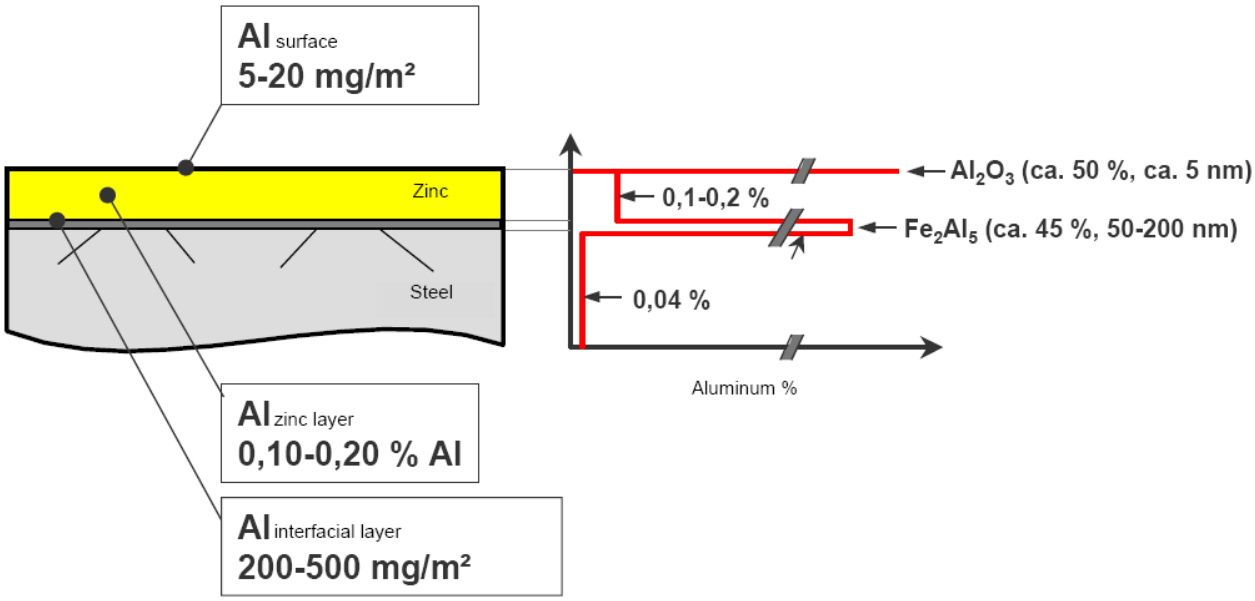

Figure 1.4: The anatomy of a galvanized coated steel with corresponding aluminum content in the coating [10].

1.4.2 Galvannealed coating

Galvannealed coatings are essentially diffusion coatings that expose hot-dip galvanized sheets to temperatures around 500 °C in order to produce a coating microstructure consisting of Fe-Zn intermetallic phases. The important variables affecting the reaction kinetics are the heating rate, hold temperature and time, and cooling rate. Since the Fe-Zn reactions are diffusion controlled, care must be taken with the galvannealing process in using optimal parameter to produce desired coating microstructures. There are several intermetallic compounds that can form as a result of the galvannealing process, the most common being the zeta (ζ) phase (6 % Fe), the delta (δ) phase ($FeZn_{10}$), and the gamma (Γ) phase (20 % Fe) [12]. The electrode lives associated with hot-dip galvannealed steels are improved compared with galvanized steels due to the different phases that result on the electrode surface as well as higher hardness for galvannealed coatings [5].

1.4.3 Electrogalvanized coatings

Electrogalvanized steel is produced by electrodepositing a zinc film onto the surface of the steel sheet. Coating weight on sheet steels ranges from 30 to 100 g m^{-2} per side. The production of electrogalvanized steel involves electroplating, which is running a current of electricity through a saline/zinc solution with a zinc anode and steel conductor. The part to be plated, the steel sheet for example, is the cathode of the circuit and the anode is the zinc. Both components are immersed in a solution containing ions that permit the flow of electricity. A current is applied to the cathode causing the metal ions in solution to lose their charge and plate out on the cathode. As the electrical current flows through the circuit, the anode slowly dissolves and replenishes the ions in the bath. Due to a difference in microstructure and different interactions with zinc and the copper electrodes used in RSW, electrogalvanized steels are proposed to have improved weldability results compared to galvanized steels. There are many advantages of the electrogalvanizing process compared to the hot-dip galvanizing process. Due to the nature of electrodeposition, the coatings produced are smooth and have excellent adherence to the sheet. They are therefore easily painted and remain intact after heavy deformation. Unlike galvanized coatings, the structure of electrogalvanized coatings is homogeneous and consists of pure zinc [13].

1.5 Electrode wear during welding of zinc coated steels

The end of an electrode lifetime is the point in the RSW process when the electrodes can no longer produce a satisfactory weld nugget under the welding conditions chosen for the test. Electrode wear is directly related to the time duration at temperature, the magnitude of the maximum temperature experienced at the electrode tip during welding, and the materials that are in contact at the E/S interface. The heat diffusion characteristics of the electrode body are important in determining the maximum temperature of the electrode, as well as the Rce and thermal contact resistance between the electrode and sheet.

The mechanisms of electrode wear of zinc coated steels are well documented in literature [5, 14-20]. There are three main mechanisms of electrode wear that occur during RSW: Mushrooming or growth of the electrode at the electrode surface, alloying between the sheet coating and the electrode, and pitting at the electrode surface. Mushrooming is a mechanical phenomena resulting from high welding temperatures and the applied force during the RSW

process coupled with microstructure changes at the tip of the electrode. At higher temperatures the copper electrode material at the surface of the electrode will begin to recrystallize and soften. The forging force during welding will result in material being pushed to the outer edge of the electrode. The extent of the softening will depend on the maximum temperature developed at the E/S interface, the amount of previous cold work in the electrode material, and efficiency of the electrode cooling. The amount of mushrooming is also dependent on the amount of soft alloy layers that form on the electrode surface. Alloying between the electrode and the zinc coated steel is dangerous because it leads to a depletion of copper at the face of the electrode and wastage of the electrode material. Depending on the zinc coating, the base metal, and the thermal cycle that the electrode experiences, certain phases form at the tip of the electrode due to zinc and iron diffusion. The Zn-Cu phases that form on the surface have a lower melting point than the original electrode and local melting will occur more readily. Also, most iron rich phases that form are brittle, and thermal cycles and welding forces cause cracking and pitting of the brittle phases, leaving an uneven electrode surface. Due to the conical shape of the welding electrodes, all of these electrode wear mechanisms eventually result in the increase in the electrode face area, and, if for given welding parameters, will cause a reduction in the current density delivered through the electrode and lead to a smaller weld nugget diameter.

Figure 1.5 shows a cross section of a welding electrode after welding 500 spot welds on galvanized steel sheets. The three electrode wear mechanisms are clearly visible. Mushrooming of the alloy layers is seen in Figure 1.5a, where the softer zinc rich phases are pushed to the edge of the electrode due to the welding force. Pitting and material loss mechanisms are shown in Figure 1.5b. These mechanisms form an uneven contact surface of the electrode, and the missing alloy products are left behind on the surface of the steel sheet. This process of pitting tends to develop non-uniform electrical current density concentration around the pit, resulting in further increases in electrode face temperature [21]. The influence of zinc coating on the alloy layer formation and subsequent weldability will be discussed in the next section.

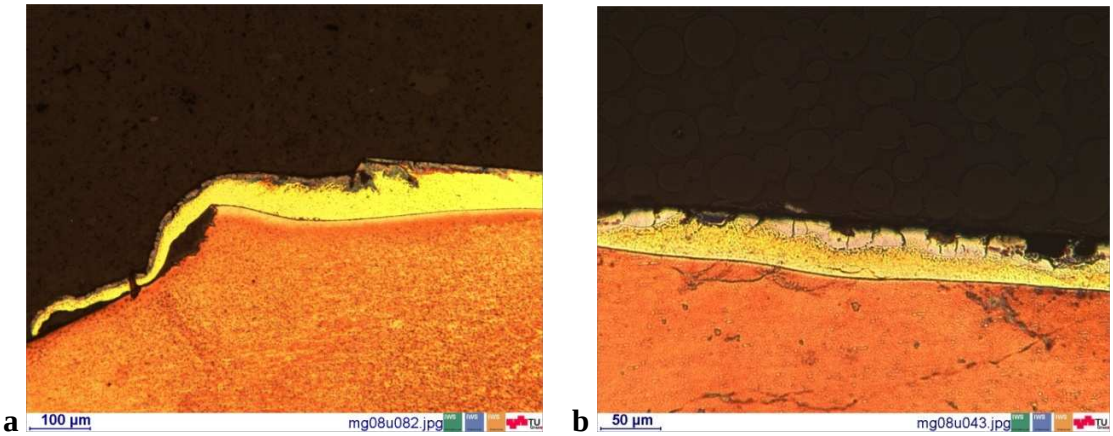

Figure 1.5: Light optical microscope images of the surface of a cross section of a welding electrode after 500 welds on galvanized steels. Mushrooming, pitting, and alloying are visible on the surface (image made by author).

1.6 The main factors influencing electrode wear and electrode lifetime

There are numerous RSW process variables that influence the weld quality, the rate of electrode wear and thus the end of an electrode lifetime. The most important of these parameters were separated into four different categories and displayed in Figure 1.6. The influence of the most important of these variables on electrode wear and weld quality will now be briefly discussed. It is important to note that factors which have a large influence on electrode wear may or may not be beneficial for weld quality. The one parameter that stands above the rest regarding its importance to heat generation and electrode wear is the Rce. This parameter will be discussed in detail under the section surface parameters.

1.6.1 Material parameters

The material parameter displayed in Figure 1.6 with the greatest influence on the rate of electrode wear is the zinc coating type. One of the first investigations into the electrode lifetime of zinc coated steels was performed in 1950 [22], where it was stated that electrode tip deformation was the main cause of the production of undersize welds. Recommendations were made for a Cu-Cr electrode to resist deformation. In more recent work investigating the wear of galvanized and galvannealed steels, Holliday et al. [14-15] evaluated electrode wear with change in electrode mass and length through an electrode life test. The fastest rate of electrode face growth was observed when welding the hot-dip galvanized coated steel, with galvannealed and uncoated steels performing much better. With galvanized steels, the dominant electrode wear mechanism was mushrooming and for galvannealed steels, the dominant mechanism was pitting

and material loss. The poor weldability results of zinc coated steels compared to bare steels was attributed to the lower melting point of zinc and to the alloy products on the surface of the electrodes.

Parker [16] proposed electrode tip growth was the rate of hardness decrease at the electrode tip during welding, which can lead to the phenomenon of mushrooming. A large reduction in material hardness at the electrode tip face due mostly to recovery and also some small areas of recrystallization were observed. The rate of hardness decrease was dependent on the electrode material and the strengthening condition of the electrode. Electrodes that resisted ageing and that were not affected by exposure to high temperatures performed better in electrode life tests results. The use of dispersion strengthened Cu-Al_2O_3 electrodes, for example, would result in longer electrode life due to the electrodes ability to retain its hardness and resist deformation.

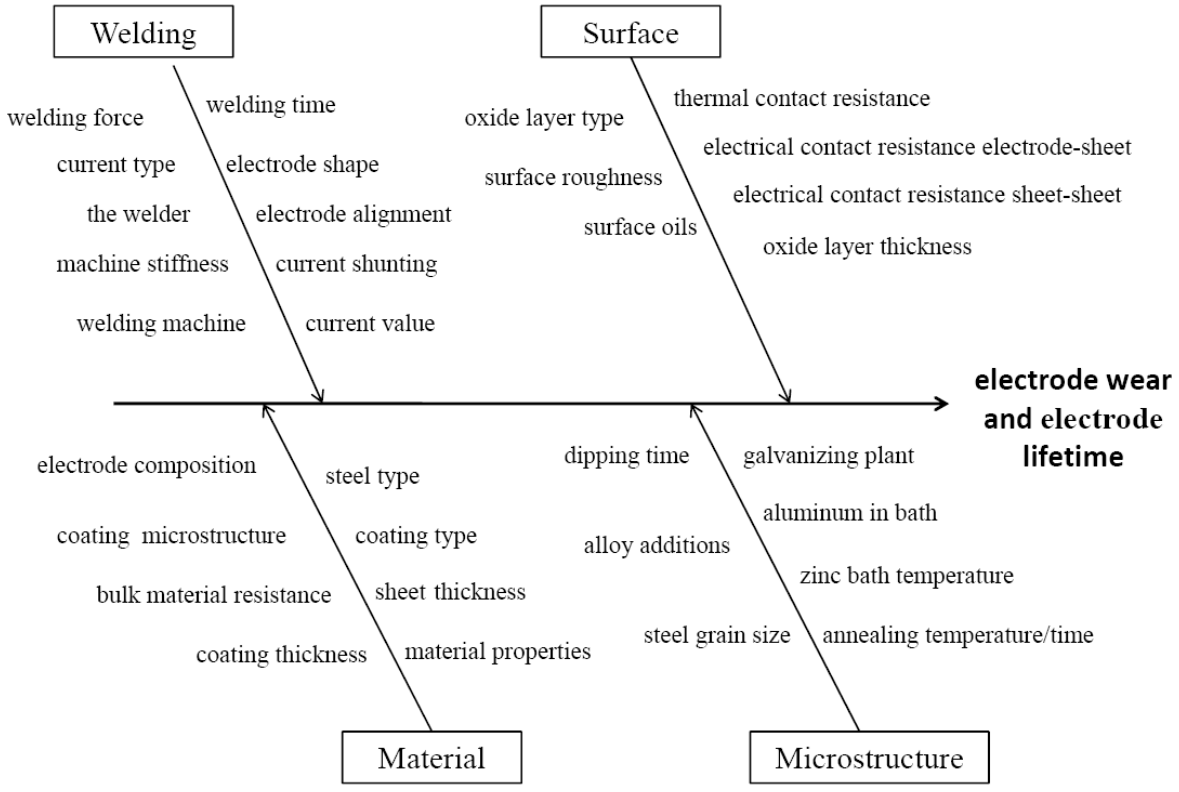

Figure 1.6: The main factors influencing electrode wear and electrode lifetime (figure made by author).

Howe and Kelly [5] compared the resistance spot weldability of the 3 different zinc coated steels and found that electrogalvanized and galvannealed steels exhibited the best electrode lives. The result was also verified by other authors [14-18]. The main reason for the improved electrode life of galvannealed and electrogalvanized steels was due to differences in the alloy products formed, which affected the electrode wear mechanisms.

The actual coating thickness was determined to influence the electrode life as well. The thicker and softer the zinc coating, the more the welding electrodes tend to indent the coating, resulting in pick up at the sides of the electrode tip and greater wear. The current range and values was also affected by coating weight [23], with both the range and values increasing with increasing coating weight. This was related to the presence of a larger zinc halo which formed around the weld, which in turn affected both the Rce and the sealing ability. The electrode life was not directly related to coating weight.

1.6.2 Microstructural parameters

The microstructure of the zinc coating has a strong influence on the resistance spot weldability of coated steels. In order to gain a better understanding of the influence of the microstructure on the electrode wear and weldability, it is important to look closer at the interfacial reactions occurring between the coating and steel during galvanizing. One of the most influential parameters on the microstructure and also the weldability of galvanized zinc coated steels is the presence of a Fe-Al interfacial layer, which in turn is strongly influenced by the amount of aluminum in the zinc bath. In fact, Howe et al. [19] determined the aluminum content in the bath to be the most significant factor affecting electrode life of galvanized coatings. Additions between 0.1-0.3 wt% aluminum are added to the bath to improve the reflectivity of the coating, to reduce the oxidation of the zinc bath, and to obtain a ductile coating by suppressing the formation of brittle Fe-Zn phases. However, the most important function of aluminum addition is for microstructure control by promoting the formation of a Fe-Al interfacial layer between 50-200 nm thickness (see Figure 1.4) between the steel substrate and the zinc. A transition point exists at approximately 0.15 wt% aluminum in the bath, above which a stable Fe_2Al_5 layer is formed and remains intact [7]. A detailed investigation into the microstructure and morphology of the interfacial layer of galvanized coating can be found elsewhere [24-28].

In terms of the resistance spot weldability of galvanized steels, it is important to avoid the presence of this inhibition layer to achieve longer electrode lifetimes. The reason is the layer

inhibits iron diffusion and prevents Fe-Zn alloying in the coating, which in turn produces a low melting point zinc product in contact with the copper electrode during welding. It was shown by Matasuda et al. [29] that iron-rich alloy layers on the surface of the electrode are beneficial to the prolongation of the electrode lifetime due to their higher melting point and resistance to the mechanisms of electrode wear.

Since most of the hot-dip galvanizing reactions are diffusion controlled, any variables that influence the time and temperature of the galvanizing process will affect the interfacial layer and thus the microstructure of zinc coatings and the weldability. In a galvanizing line, there are many different variables to mention and consider. According to Faderl et al. [30] the most significant parameter affecting the aluminum content in the interface layer and the interface layer thickness was found to be the difference between the bath temperature and the initial strip temperature.

Substrate solute additions are known to affect the rate of attack of zinc on steel during hot-dip galvanizing, and thus inhibit the formation of Fe-Zn phases. Some important solute additions to the steel substrate and/or the zinc bath include aluminum, carbon, manganese, titanium, niobium, and phosphorus. Alloying additions can be separated into elements that segregate to the grain boundaries, like carbon and phosphorus, and those that form compounds that will precipitate through the grain, leaving the grain boundaries clean and pure. Hisamatsu [31] suggested the chemical nature of grain boundaries increases the thermodynamic activity at grain boundary sites on the steel surface during galvanizing, resulting in preferential nucleation sites and growth of Fe-Zn phases at these sites. Clean grain boundaries have no barrier to Fe-Zn formation while segregated grain boundaries limit their activity and inhibit Fe-Zn compound formation. Interstitial-free steels have grain boundaries that are essentially carbon free due to the precipitation of titanium and niobium carbides within the grain and are therefore more sensitive to Fe-Zn outburst formation. Phosphorus is also known to segregate to ferrite grain boundaries and block the diffusion of zinc along those boundaries. It was proposed that substrate grain boundary cleanliness is the dominant steel substrate feature that controls the kinetics of the Fe-Zn reaction during galvanizing [32].

Jordan and Marder [33] also determined the influence of grain size of the substrate steel on the Fe-Zn alloy phase reaction kinetics during hot-dip galvanizing. In their experiments, steels substrates with two grain sizes, 15 and 85 μm, were tested in a decarburized low-carbon steel

and hot-dipped galvanized in 0 wt % and 0.2 wt% Al-Zn baths. In aluminum-free galvanizing baths, the substrate steel grain size had no influence on the kinetics of phase growth on Fe-Zn compounds. However, in the 0.20 wt% aluminum bath there was a strong influence of grain size on the phase growth. The 15 µm grain size steel showed numerous areas of Fe-Zn outbursts, while the 85 µm grain size steel showed no Fe-Zn phase growth over the same reaction times. This phase growth thus corresponds to the location of substrate grain boundaries, and more grain boundaries promote the Fe-Zn reaction.

There is also an influence of the substrate steel on the electrode life, and this is related to the material properties, specifically the bulk material resistivity, as proposed by Howe [34]. Higher bulk resistivities result in lower current requirements and longer electrode lives. Also, higher bulk resistivities shift the resistance and resistive heating away from the E/S interfaces, and into the bulk. If less resistive heating occurs at the E/S interface, the rate of alloying and electrode wear decreases.

1.6.3 Welding parameters

The welding current value and welding time have the greatest influence on the temperature of the electrode surface and therefore the extent and rate of electrode wear during welding. These parameters are determined in the manner as shown in chapter 1.3 and usually do not change during welding experiments (unless current stepping occurs). The electrical and mechanical factors, specifically current type (alternating current (AC) or direct current (DC)) and welding force will be briefly discussed with regards to their influence on weldability and electrode wear.

The differences in the welding performance of AC and DC welding systems are related to the precise shape of the current waveform. According to Nishiguchi and Matsuyama [35], for a fixed value of root mean square (rms) current and time, the total energy input to the weld zone would be larger for DC than for AC currents. As a result the weld nugget growth commences at an earlier stage and grows at a slightly faster rate when using DC currents and a lower welding current can be used to create the same size weld nugget. This relationship was supported by Li et al. [36], who examined the differences between AC and DC waveforms on the weld size using a finite element simulation model. Podrzaj et al. [37] found that high peak AC values are much more likely to cause expulsion than welding currents with lower peak values but the same rms. Thus the welding current ranges for a certain set of materials is wider for welding with DC. It is

also important to mention the influence of thermoelectric effects such as the Peltier and Thomson effects, which can have an influence on the shape of the weld nugget and differences in electrode wear between the top and bottom electrodes when using DC welding setups [38-39].

Regarding the mechanical aspects, the machine stiffness and welding force are the most important variables with respect to weld formation. The machine stiffness has a big influence on the weldability range, specifically on the expulsion limits during current range tests. Machines should be sufficiently rigid as to minimize skidding of the electrodes or deflection of the electrode arms. High stiffness increases the current for weld metal expulsion and also reduces electrode misalignment and is therefore recommended. Electrode head assembly friction adversely influence weld quality because it leads to the formation of internal discontinuities in the weld such as porosity [40-42].

The effect of mechanical loading on the Rce was investigated by James et al. [43] and Crinon and Evans [44]. During welding, when there is no microscopic sliding at the contacting surfaces, the Rce of that surface remained very high. When sliding occured at the E/S or S/S, the Rce was much lower. The sliding and shear stress disrupt the insulating oxide surface layer, producing metal to metal contact. Contact pressure alone in not enough to disrupt the surface film, but a shear stress at the interface is needed to crack the film. The amount of breakdown that is experienced by the oxide layer is dependent on the oxide thickness, the surface roughness, and the amount of shear stress on the surface.

1.6.4 Surface parameters

Any variable which affects the temperature evolution at the E/S and S/S interfaces is considered here. Since the temperature evolution at the interface is directly related to the Rce, any parameter which influences Rce will have a significant influence on the temperature evolution. These include surface roughness, zinc coating type, and surface oxides. The presence of oil on the sheet surface can either increase or decrease the Rce, depending on the type of oil, the length of time the oil is exposed to the surface, and the chemical reaction of the oil and the surface [45]. Oils that break down surface oxide layers or prevent their formation decrease the Rce, while oils that promote oxide layer formation tend to increase Rce. The next section will go into more detail the theory of Rce.

1.7 Electrical contact resistance theory

The Rce between two metals is a complex physical property. For this reason scientists have been extensively studying the Rce for over 70 years. The Rce is known to be a function of several different variables including the following: the real contact area, the contact pressure, yield stress of the contact surfaces, the interface temperature, surface characteristics such as roughness and oxide layer thickness, and the bulk resistivity of the contacting materials [46]. A detailed review of Rce theory and important concepts will now be discussed. First, the nature of contact surfaces and contact asperities will be introduced. Then, the physical aspects of the film and constriction resistance will be explained followed by the classical equation for Rce. Next, a description of the different experimental measuring techniques will be discussed as well as the pertinent research challenges facing the RSW community. Finally the motivation and impetus for this current work will be presented at the end of this section.

1.7.1 The nature of contact asperities

In order to understand Rce of metals, it is important to first discuss the nature of contact surfaces. Real surfaces are not atomically flat, rather they are rough and are composed of a large number of small, but discrete, contact points called contact asperities [47]. Therefore, when two metals come into contact, the entire area of the contact surface is not touching, rather only a small area. This true area of metallic contact occurs at the contact asperities. In a ductile material, the number of these surface asperities supporting an applied load increases with increasing temperature and pressure due to yielding of the asperities and thus more coming into contact. The Rce across the surface of two metals is known to decrease with asperity flattening and thus with an increase in the number of asperities coming into contact [46].

A schematic representation of this concept during RSW can be seen in Figure 1.7 [48]. These asperities at the S/S interface are represented by the black dots in the figure, while the circle represents the apparent contact area. Initially, the true contact area will be a small fraction of the apparent contact area and will increase with temperature and pressure, approaching the limit of the apparent contact. This is, of course, not only the case at the S/S interface, but the E/S interface as well. When a current is applied across these contacting metals, it is allowed to flow only through the true areas of metallic contact, or only through the asperities. This can lead to a situation where the current is constricted while passing through these asperities. This concept will be discussed in the next section.

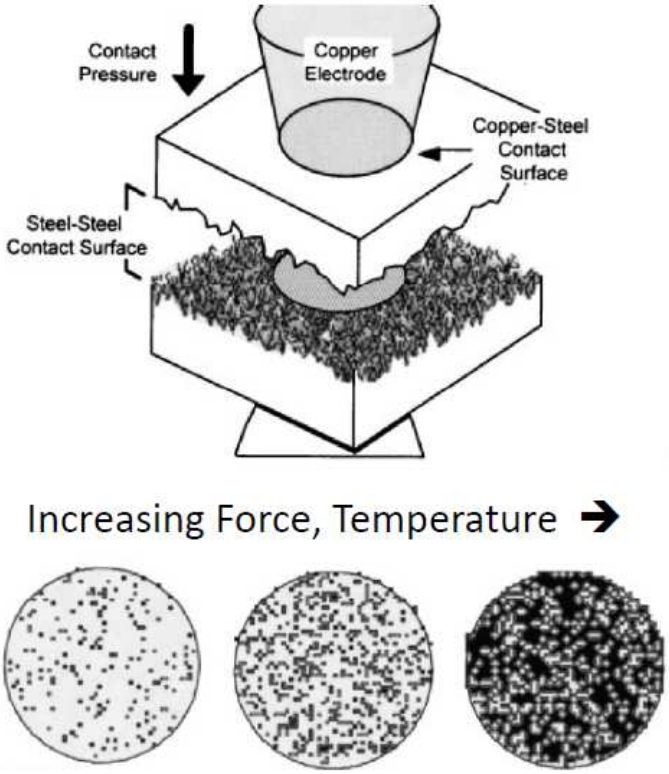

Figure 1.7: True contact area vs. apparent contact area during RSW [48]. The true contact area will initially be a small portion of the apparent contact area, and will approach the apparent contact area with increasing force and temperature.

1.7.2 Film and constriction resistance

One of the first published contributions to Rce in RSW was performed by F. Studer in 1939 [49]. The electrical resistance across the boundary between two conducting surfaces was accounted for in two different ways: the presence of a thin film of foreign material between the surfaces, and the concentration of current through small areas of true metallic contact. Presently, the Rce in RSW is known to be the sum of a high resistance film contact and a low resistance metallic contact [46].

Generally, even a clean metal surface is tarnished with a surface film. The film resistance is mainly due to highly insulating surface oxides, but also grit, surface oils, and other compounds. These films contribute to the resistance of the electrical contact because they decrease the possibility of local metal connection at the asperities. The film resistance will generally start very large, and then decrease with increasing temperature and pressure due to the break down of the highly resistive, insulating layers and the burning off of oils/grit.

The metallic contact is known as and referred to in publications as constriction resistance, as first proposed by Bowden and Williamson in 1958 [50]. If an electric current is passed between two conducting metals, the flow of charge will be greatly constricted in passing the contact interface due to the fact that only a very small fraction of the surfaces will be in electrical contact. This constriction of current lines passing through a contact area is schematically shown in Figure 1.8 [51]. Due to this constriction in the current flow lines, the potential difference across the interface will be greater than that which would have been produced by the same current passing uniformly across the boundary. Thus, the disturbance in the current stream will give rise to an additional increase in resistance in the electrical circuit. As seen in Figure 1.8, the constriction is most severe in the metal close to the interface. Also, most of the energy dissipated as the current flows through the constriction appears as heat generated in the immediate vicinity of the interface.

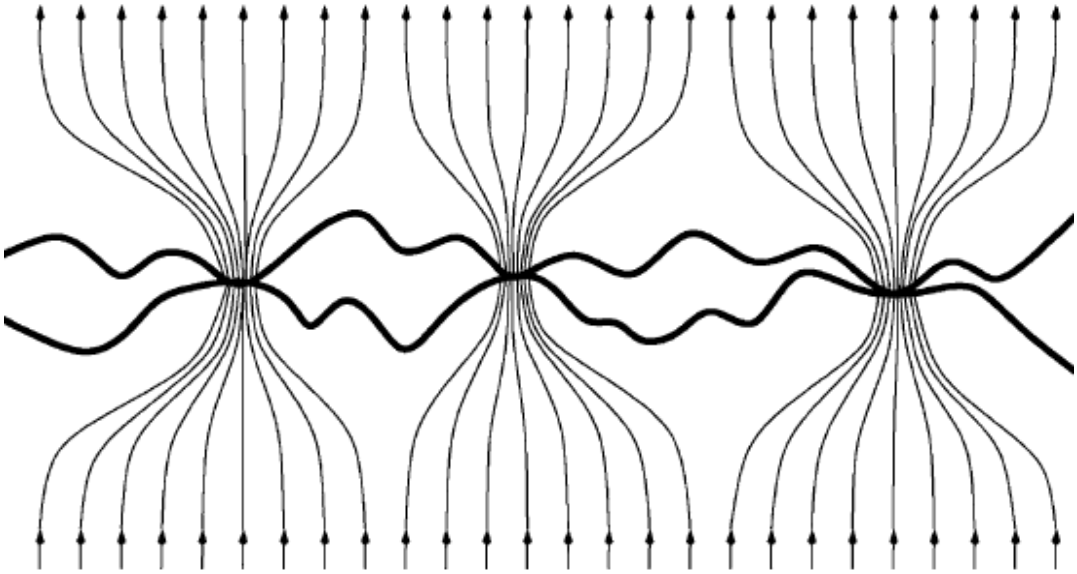

Figure 1.8: Schematic diagram of the physical current flow lines in constriction resistance [51]. The welding current is constricted to minute areas on the contact surface, causing local heating and a rise in resistance.

1.7.3 Classical equation for electrical contact resistance

With the size and number of contact asperities, the specific resistivity of the materials in contact, and the electrical characteristic of any contaminant film, it is possible to estimate the value of Rce (in Ohm) according to the following equation from Greenwood [47]:

$$R_{ce} = \{(\rho_1 + \rho_2)(\frac{1}{4\eta\, a} + \frac{3\pi}{32\eta\, l})\} + \frac{\rho_f\, s}{A_c} \tag{1.2}$$

where η is the number of contact asperities, a is the average radius of contact asperities, ρ_1 and ρ_2 are the specific resistivities of the materials in contact, ρ_f is the resistivity of the surface film, s is the thickness of the surface contaminant, A_c is the contact area, and $2l$ is the average center to center distance between asperities. The first part of the expression is due to constriction effects, and the second is due to surface contaminants or film effects. If the surface is clean and uncoated, the second added term in the equation is not present. It is important to note the load and temperature are not explicitly present in Eq. 1.2, but both influence the values of η and a. With increasing force and temperature the values of η and a will also increase, which will lead to a decrease in Rce. However, if the surface resistivities increase, for example from an increase in temperature through constriction resistance, this will lead to an increase in the Rce.

Calculating accurate values of Rce using this equation requires knowledge of the size and number of contact asperities under a given load at a certain temperature, as well as the thickness, composition, and distribution of contaminants, which in reality is very difficult to obtain. An alternate approach is to measure the Rce directly for a given material, temperature, and load combination. This will now be explained in the next section.

1.7.4 Experimental measurements of the electrical contact resistance and the dependence on temperature and pressure

The importance of measuring and analyzing the Rce for RSW is widely recognized and has been extensively studied [43, 44, 48, 52-63]. The Rce and its variation with temperature and pressure are crucial for the accurate description of the formation of a weld nugget in RSW process models. In order to facilitate the incorporation into RSW process models, the Rce has recently been expressed as a unit area Rce (with the units Ohm m^2). In RSW, the unit area is equivalent to the face diameter of the welding electrodes at the E/S interface and the apparent contact area at the S/S interface.

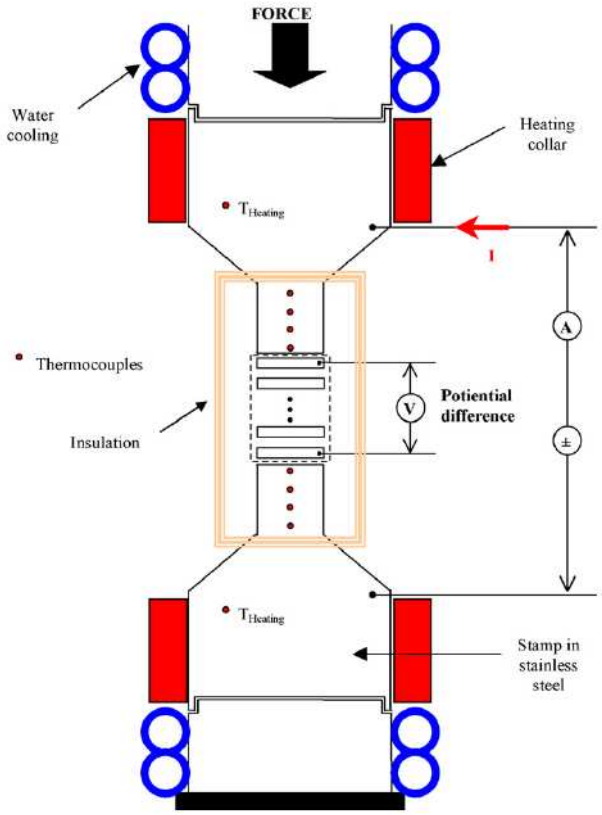

Figure 1.9: Device used to experimentally measure the Rce as a function of pressure and temperature [53].

One of the most widely used methods for experimentally measuring the Rce as a function of temperature and pressure is schematically shown in Figure 1.9 [3, 52-58]. In this ex-situ experiment, the investigated samples are placed in a power press between two stamps connected through electrical wires to a current power supply. Currents are supplied to the measuring circuits and the voltages across the contact interfaces are determined. The measurements of load, current, and voltage are recorded simultaneously using computerized data at different furnace temperatures. The main advantage of this technique is the ability to control the contact interface temperature as well as the contact pressure. Presumably, other advantages include the control of the real area of contact with accurate surface preparations, as well as the ability to investigate both the E/S and S/S contact surfaces simultaneously. However, these experimental conditions are non-realistic compared to actual welding. Specifically, the slow heating rate does not accurately represent the actual welding process, where very fast heating rates and high temperature gradients across all directions certainly play a role in the values of Rce.

Additionally, in these ex-situ experiments, a low current is applied to the device compared to a high welding current used in real welding experiments. As a consequence, the effects of constriction resistance are not accurately accounted for. Also, it was shown that interface sliding during welding can breakdown the film resistance during RSW, and this is not accounted for in the described setup [44]. Despite these drawbacks, the influence of pressure and temperature on the Rce can be experimentally determined.

A standard exist for evaluating the Rce of metals in contact: DVS 2929 [59]. This measurement method takes place during the actual welding process and thus considers the complicated interfacial conditions that are present during welding such as interface sliding, large and uneven contact pressure, rapid heating rates. Voltage leads are attached to the welding electrodes as well as the sheets and the voltage drop is calculated across the electrodes and across the contact interfaces as a function of welding time. Ideally, the resistance should be evaluated as a function of the interface temperature in order to implement the Rce vs. temperature curve into process models, but this is very difficult to experimentally measure due to large temperature gradients at the contact surfaces. Another main shortcoming of this technique is the inability to account for the bulk material resistance contribution. Both the bulk material resistance and the Rce are measured instead of only the Rce. Again, this is impossible to experimentally account for the increase in bulk material resistance with this setup.

In most results published in literature, a decrease in the Rce with increasing pressure and temperature was found for copper-steel, copper-zinc, steel-steel, and zinc-zinc contacts [3, 43, 44, 49, 52, 57-61]. The reasons for this trend were the breakdown of highly resistive surface films and the eventual flattening, yielding, and melting of contacting asperities. Several researchers, however, have recently proposed results contradictory to established theory as to the shape of the Rce curve as a function of temperature [48, 53-56, 62]. Using this same technique as just described, Rogeon et al. [53] measured an increase in the Rce at both the E/S and S/S interface for galvanized coated steels, and a subsequent decrease before melting of the coating. The reason for this increase in Rce was attributed to a very high contact ratio at the beginning of the tests (real contact area : apparent contact area) for zinc coated materials due to a low yield stress of the surface zinc. In other words, the decrease in resistance due to more surface asperities coming into contact was negligible because the initial true contact area was almost equal to the apparent contact area. Thus, an increase in resistance was attributed to surface resistivity effects.

Song et al. [62] also measured a local peak with a Gleeble machine for uncoated low carbon and stainless steels and attributed this trend to an increase in the surface resistivity of the metals in contact from constriction resistance. It should be said that although the experiments with a Gleeble machine more accurately represent the RSW process with regards to heating rates and interfacial pressures, the interface temperature estimation is limited by the distance of the thermocouple from the contact interface. However the measured increasing trend in Rce with temperature is still well-founded.

Babu et al. [48] developed an empirical model which also predicted a peak in the Rce curve at intermediate temperatures for copper-steel and steel-steel contact. Here, the competing effects of bulk material resistance and Rce were the reasons given for this peak.

1.8 Impetus for current research

There still remain doubts as to the actual shape and values of the Rce curve as a function of interface temperature for different material combinations as well as the validity and accuracy of different measuring techniques. It is unclear the exact reason for the presence of a peak in the Rce curve as a function of temperature and, perhaps more importantly, the increasing trend of Rce with temperature for different material combinations. Clearly, if the Rce curve is in fact increasing in nature, this must also be implemented in process models in order to achieve accurate temperature predictions.

Regarding measuring techniques, most efforts take place externally from the actual welding process and thus do not account for important effects such as fast heating rates, uneven pressure distributions, constriction resistance, and electrode sliding which are present during RSW and can greatly influence the Rce. On the other hand, those efforts that take place during the welding process have the following limitations: the inability to separate the contributions of the Rce and the bulk material resistance from the measured total resistance value, and the inability to accurately measure the contact interface temperature.

There is clearly a demand in the RSW field for an all encompassing measuring technique for the Rce, especially considering the growing importance of modeling the RSW process as well as new material/coating joining combinations in automobile bodies. This current work proposes a new experimental-cum-theoretical approach to acquire the Rce curve as a function of interface temperature. An experimental measuring technique will be proposed to measure the total

resistance during welding as a function of welding current. Next, the finite element method will be used to validate this proposed measurement technique. Specifically, the FEM program SYSWELD will be used to find the current value where the bulk material resistance plays a role in the experimental measurements, and current ranges will be determined in which the Rce can be experimentally measured. Finally, the finite element method will be used to predict the contact interface temperature with a numerical optimization technique.

1.9 Summary and conclusions

The RSW process remains the most important joining method for the automobile industry. For this reason, there exists high demand for research in the field regarding the weldability of different material and coating combinations in order to improve process efficiency. One of the main problems for the resistance spot weldability is the wear of the welding electrodes. Electrode wear causes an increase in the contact diameter of the welding electrodes, which in turn leads to a decrease in the current density through the electrodes and the formation of undersized welds in critical automobile components. The electrode wear mechanisms, namely mushrooming, alloying, and material loss/pitting, are greatly accelerated with the presence of zinc coatings on the surface of the steel.

Additionally, the type of zinc coating as well as the coating microstructure has a significant influence on the electrode wear rate during RSW. Generally, softer and lower melting point phases on the surface of the electrode, such as Cu-Zn phases, promote the rapid wear of welding electrodes. On the other hand, Fe-rich phases have higher melting points and promote longer electrode lives because they slow down the wear mechanisms. Galvannealed coating have longer electrode lives than electrogalvanized or galvanized coatings due to the different iron phases present in the coating and thus the Fe-rich alloy products which form on the electrode surface. Regarding the microstructure of galvanized steels, the presence of a Fe-Al interfacial layer between the steel and zinc coating was known to greatly influence the electrode life. A transition point exists at approximately 0.15 wt% aluminum in the zinc bath, above which a stable Fe_2Al_5 layer is formed and remains intact between the zinc coating and steel substrate. This layer is known to inhibit the diffusion of iron and thus prevent Fe-rich phases from forming on the welding electrodes.

A detailed literature review was performed and some of the most important factors influencing the electrode wear and weld quality were discussed. The most important of these factors was determined to be the Rce at the S/S interface for weld size and quality, and at the E/S interface for electrode wear. For this reason, a main part of this first chapter was dedicated to Rce concepts and theory and different measuring techniques to quantify the Rce. The following summary and conclusions can be made from this chapter regarding the Rce:

- The Rce between two metals during RSW has been studied for the last 70 years. It is known to be a function of several different variables including the real contact area, the contact pressure, the yield point of the contact asperities, the interface temperature, surface characteristics such as roughness and oxide layer thickness, surface oils and bulk resistivity of the contacting materials.
- When two metals come into contact, the true contact area will always be less than the apparent contact area because surfaces are not atomically flat. The true area of contact occurs at contact asperities.
- There are two physical contributions to the Rce of metals: the film resistance and the constriction resistance. The film resistance, mainly caused by a surface oxide, will usually decrease with increasing temperature and increasing force due to the breakdown of the highly resistive oxide. The constriction resistance, which is caused by the constriction of current lines through contact asperities, can cause a local increase in the resistance and temperature on the surface.
- The different methods to measure the Rce, both in-situ and ex-situ, where outlined in this chapter. Although these methods can generally quantify the Rce, they all have shortcomings in certain areas.
- The measurement efforts that take place externally from the welding process do not account for important effects such as fast heating rates, uneven pressure distributions, constriction resistance, and electrode sliding which are present during RSW and can greatly influence the Rce.
- Those measurement techniques that take place during the welding process do not separate the contributions of the Rce and the bulk material resistance from the measured total resistance value, and do not accurately measure the contact interface temperature.

- It is generally believed Rce will decrease with increasing interfacial temperature due to the breakdown of the film resistance. However, recently there is measured evidence of an increase and peak in this curve with increasing temperature.
- There exists a demand for an all encompassing measurement technique to measure the Rce as a function of interface temperature.

Chapter 2: Experimental Measurement Technique: Total Resistance as a Function of Welding Current

2.1 The dynamic resistance curve during resistance spot welding

The total resistance in RSW is an important parameter because it can be used to explain many physical aspects about the welding process. It is composed of the Rce at the E/S and S/S interfaces, and the bulk material resistances of the electrodes and sheets. In order to evaluate the total resistance, the voltage drop is experimentally measured during RSW with leads attached to the welding electrodes. This voltage measurement is taken at the peak of the current waveform (both AC and DC) in order to avoid impedance effects in the measurement [61]. Taking both the voltage drop and welding current as a function of time, the resistance can be calculated using Ohm's law. The result is often referred to as the dynamic resistance of the system because the resistance changes with time.

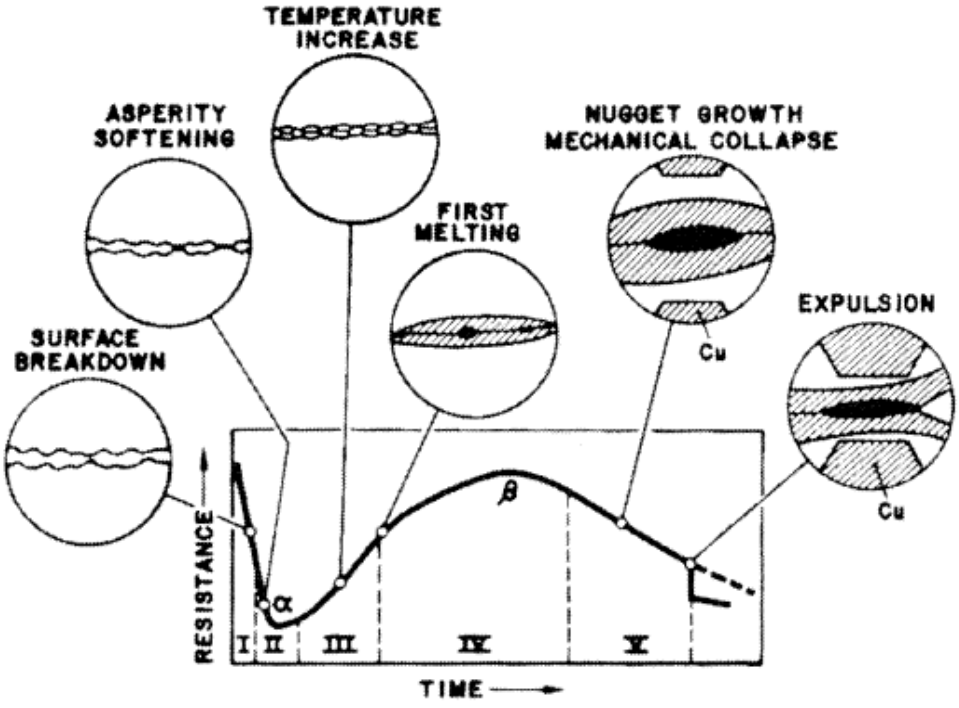

Figure 2.1: A typical dynamic resistance curve for RSW of zinc coated steels [63]. The beginning of the curve describes the physical aspects of the Rce of the system.

An example of a typical dynamic resistance curve for zinc coated steels is given in Figure 2.1 (a similar curve applies for uncoated steels as well) [63]. The initial drop in the curve is

related to the important Rce phenomena including the breakdown of the resistance films such as an oxide layer on the sheet surface, the deformation of asperities and thus the increase in real contact area, as well as the softening and melting of the zinc coating. The subsequent increase in the dynamic resistance curve is mostly related to the temperature increase and bulk material resistance heating. To date, there has been no in-situ experimental measurement technique to separate the contribution of the bulk material resistance and the Rce from the dynamic resistance measurements. In order to do this, one must know the exact temperature at each area in the bulk material in order to estimate the bulk resistance, a situation that seems best suited for FEM.

In this chapter a new experimental measurement method will be introduced to measure the total resistance during the welding process as a function of welding current using resistance measurements in the welding electrodes. This method is similar to DVS 2929 [59], however it differs in the type of welding current application. It will also be shown this technique will be the starting point for the determination of valid current ranges in which the Rce is measured without the influence of bulk material resistance in Chapter three, and the determination of the interface temperature, which will be presented in Chapter four. This chapter will describe the measuring technique and the modifications to the welding current and welding process. The experimental results will be presented and discussed as well at the end of the chapter.

2.2 Description of experimental measuring method

The theory behind the new measurement technique will now be briefly discussed with the aid of Figure 2.2. This figure shows the theoretical shape of the total resistance, the Rce, and the bulk material resistance curves as a function of increasing temperature or increasing welding current. As discussed earlier, the Rce will usually decrease with increasing temperature. This is also the case for the input Rce curves in the SYSWELD database for coated and uncoated steels. The bulk material resistance will always increase with increasing temperature from to the theory of electrical conductivity of metals [64]. Although the total resistance is the sum of the Rce and the bulk material resistance, in the lower temperature range the total resistance is almost exclusively the Rce plus room temperature bulk material resistance. It is desired to stay in this temperature range in the bulk of the materials in the experimental measurements to limit the contribution of the bulk material resistance to just room temperature effects. In doing this, total resistance measured will represent the shape and values of the Rce.

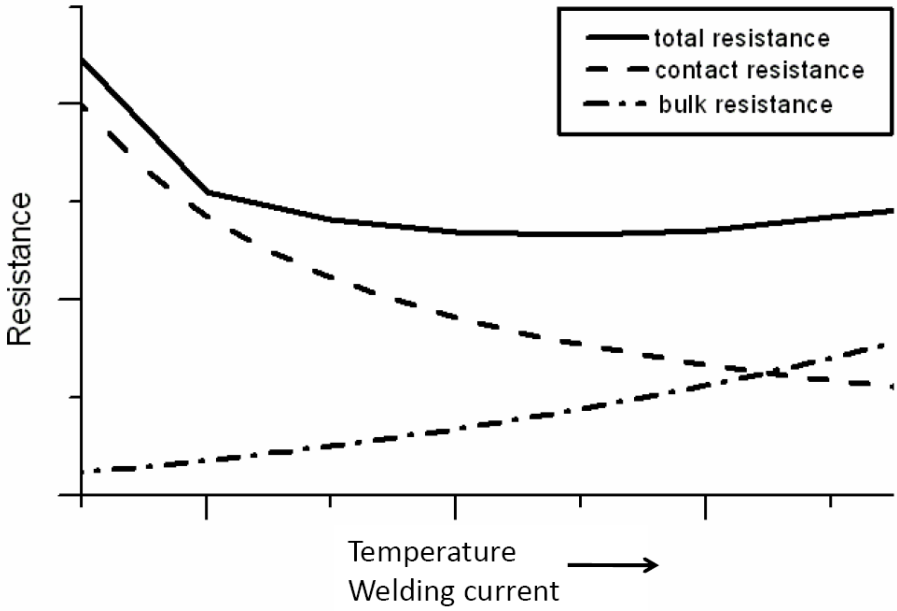

Figure 2.2: Schematic diagram of the contributing resistances during RSW (curve made by author).

A schematic diagram of the new approach with the contributing resistances and the voltage measurement is shown in Figure 2.3. Only one sheet was used in this approach instead of the normal welding with two sheets. The reason for performing an experiment with one sheet was to eliminate the Rce at the S/S interface in order to simplify the problem and focus on the E/S interface. The bulk resistance of one sheet and two electrodes as well as the Rce at the two E/S interfaces are present in the measurement. The current was also modified in this new approach. Instead of the normal 10-12 periods of AC application, only one period AC was used. Relatively low welding currents were also used in this experiment with the range 0.5-9.5 kA effective current. The reasons for the welding current modifications are threefold. Firstly, it was desired to minimize the effects of thermal conduction and therefore the temperature dependent bulk material resistance on the total resistance values measured in the welding electrodes. As mentioned above, it was desired to measure in the lower temperature range to investigate only the Rce. The second reason was to produce an always increasing temperature at the E/S interface with each successive measurement. The final reason was to simplify the implementation of the current waveform into the SYSWELD software.

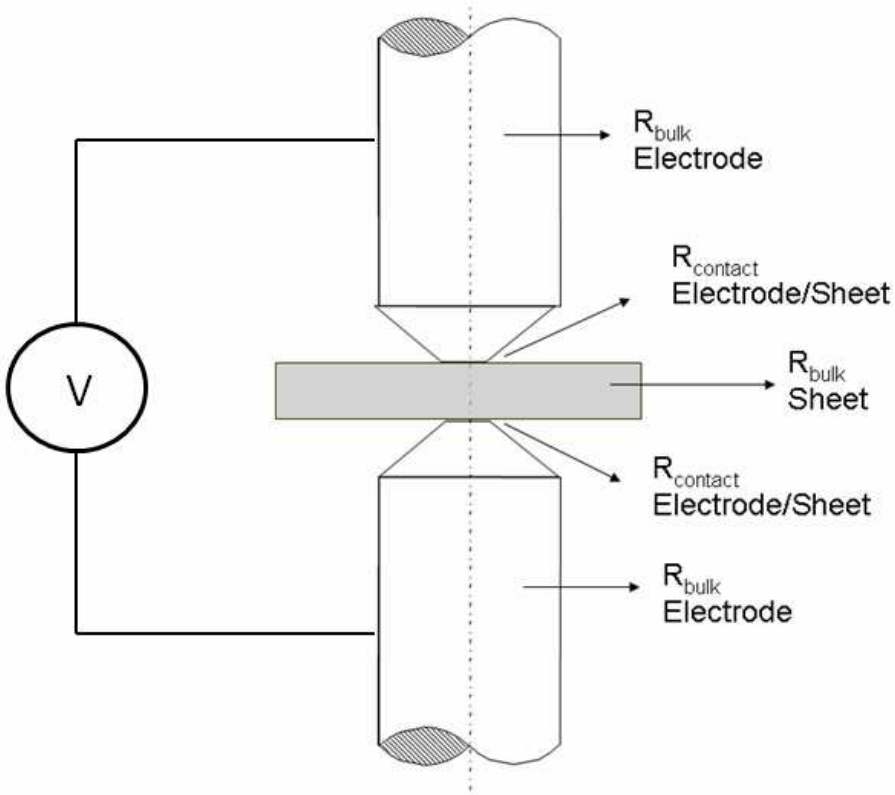

Figure 2.3: Overview of the contributing resistance factors in the modified single sheet welding experiment. The experimentally and numerically measured voltage drop includes all of the contributing resistances in the process (figure made by author).

Figure 2.4 shows the smoothed, real time current waveforms that were used in the measurements. These current waveforms, ranging from 0.5-9.5 kA effective current, were experimentally measured and smoothed so they could be input in the RSW simulation for better accuracy. The points in Figure 2.4 represent the peak in the first half wave of current application. Each point represents one welding experiment in which one total resistance value was calculated with the corresponding voltage drop. As the current increases with each successive step, the interface temperature at the E/S interface also increases. Thus, the resulting data of total resistance versus welding current should look identical to the Rce curve as a function of temperature.

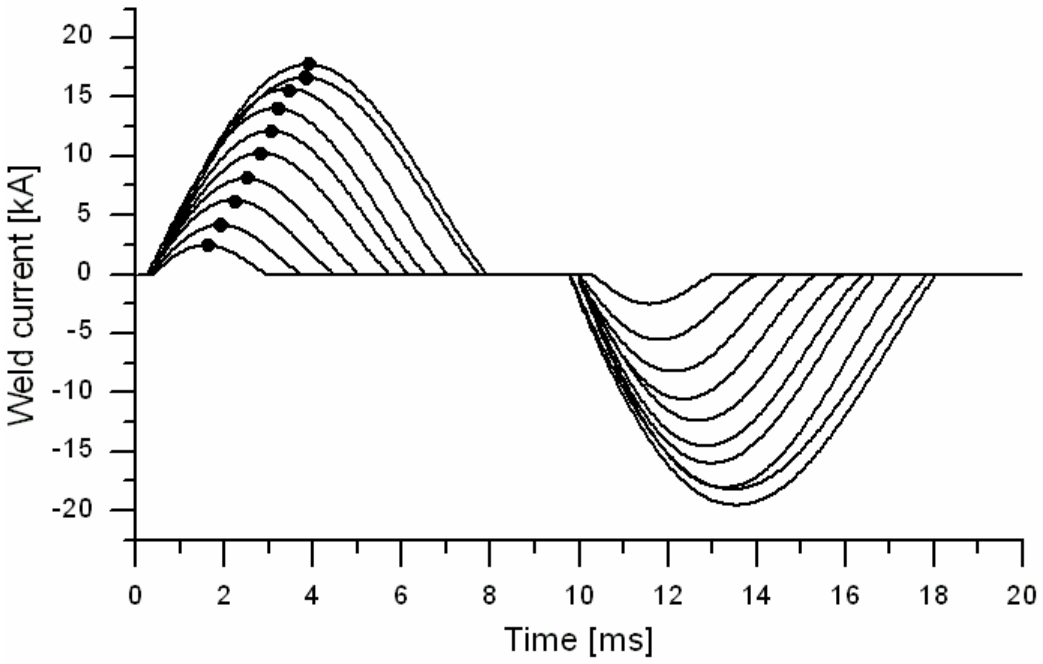

Figure 2.4: Real time current waveforms from the experiment, which were also used in the spot welding simulation (figure made by author).

Table 2.1: Table of materials used in the experimental measurements

material	standard	surface condition	sheet thickness	yield strength	tensile strength	C	Mn	Si	P	S	Ti	Al
			mm	MPa	MPa	wt%	wt%	wt%	wt%	wt%	wt%	wt%
DX54D	EN 10346	Z100	0.8	120-220	260-350	max 0.120	max 0.600	max 0.50	max 0.100	max 0.040	max 0.300	-
DX54D	EN 10346	ZF100	0.8	120-220	260-350	max 0.120	max 0.600	max 0.50	max 0.100	max 0.040	max 0.300	
DC06	EN 10152	ZE75/75	0.8	130-180	270-350	max 0.020	max 0.250		max 0.020	max 0.020	max 0.300	
H180Y	EN 10268	bare	0.8	180-230	340-400	max 0.010	max 0.700	max 0.300	max 0.060	max 0.020	max 0.120	min 0.010
HTC600X	EN 10336	bare	1.0	340-420	min. 600	max 0.170	max 2.200	max 0.800	max 0.080	max 0.010		max 2.000
HTC600X	EN 10336	Z100	1.0	340-420	min. 600	max 0.170	max 2.200	max 0.800	max 0.080	max 0.010		max 2.000

2.2.1 Materials used in the experimental measurements

The chemical composition and mechanical properties at room temperature of the different steels which were experimentally measured with the technique are given in Table 2.1. The reasons for choosing these certain materials for investigation are as follows. Firstly, it was desired to measure the Rce of all of the different zinc coatings, hence the choice of galvanized, galvannealed, and electrogalvanized steels. Secondly, it was desired to determine the influence

of yield strength of the steel on the Rce, hence the choice of a soft, low carbon steel and a stronger DP600 steel. Finally, it was desired to compare the results to simulation, and the SYSWELD RSW database contains material data for low carbon, DP600, and galvanized coated steels (high carbon steel as well).

Table 2.2: Table of pertinent welding parameters

material	welding force kN	welding machine	welding current	welding electrode
DX54D	2.5	AC 170 kVA power source	1 period AC 0.5-9.5 I_{eff}	F1–16-20-50-5.5
DX54D	2.5			
DC06	2.5			
H180Y	2.5, 3.5, 4.5			
HTC600X	3.5			

2.2.2 Experimental procedure

The surfaces of the materials were cleaned to remove any oils and surface grit and were welded in this condition. F1–16-20-50-5.5 electrodes according to EN ISO 5821 were used in the welding experiments [65]. The electrode material was A 2 / 2 according to EN ISO 5182 (Cu with 1 % Cr and 0.1 % Zr) [66]. The squeeze time, weld time, and hold time were 20, one, and 10 periods, respectively, and the welding force was 3.5 kN for the one mm thickness materials and 2.5 kN for the 0.8 mm thickness materials. Additionally, three different welding forces were used for the uncoated H180Y steel to investigate the influence of force on the total resistance values. Table 2.2 shows the pertinent welding parameters in the experimental study. A SCHLATTER Selecta pedestal machine with an AC 170 kVA power source was used as shown in Figure 2.5. Experiments were performed with effective welding currents of 0.5 to 9.5 kA with steps of one kA. The voltage drop was measured between the electrodes using an in-house built computer assisted measurement system which recorded values every 0.1 ms. The total resistance was calculated using the voltage drop measurement at the peak of the first half wave of the welding current (see Figure 2.4). The experiments were repeated four times for each current step. The average total resistance from the experiment was evaluated as a function of current. Electrode imprints on the surface of the metal sheets were examined with a stereoscope and the average diameter was recorded using image analysis from four different measurements.

Figure 2.5: RSW machine, AC 170 kVA used in the welding experiments. All welding experiments were performed at voestalpine in Linz, Austria.

2.3 Experimental results and discussion

2.3.1 Uncoated steel-copper contact

The experimental results of the new measurement technique are shown in Figure 2.6 for single sheet uncoated DP600 steel-copper contact. The maximum weld current on the x-axis corresponds to the points in Figure 2.4 for the peak in the first half wave of current application. Since these are single sheet experiments, the total resistance is the sum of the bulk resistances of two electrodes and one sheet, and two Rce at the E/S interfaces. There is initially an increase in the total resistance until a peak is reached at 4 kA maximum current (or at 1.5 kA effective current). After this peak the curve falls significantly, flattens, and begins to increase as the

welding current increases. It is proposed that the peak in the low current range is most likely a peak in Rce due to the constriction resistance and an increase in surface resistivity. As outlined earlier in chapter one, there are competing effects of asperity deformation and surface resistivity in the Rce of two surfaces. From Eq. 1.2, an increase in surface resistivity will increase the Rce of two metals in contact, while asperity deformation and more asperities coming into contact will decrease the Rce. If the increase in Rce from the surface resistivity outweighs the decrease in Rce from surface area, then it is possible for the Rce curve to increase. The increase in the higher current range is most likely the increase in the bulk material resistance contribution.

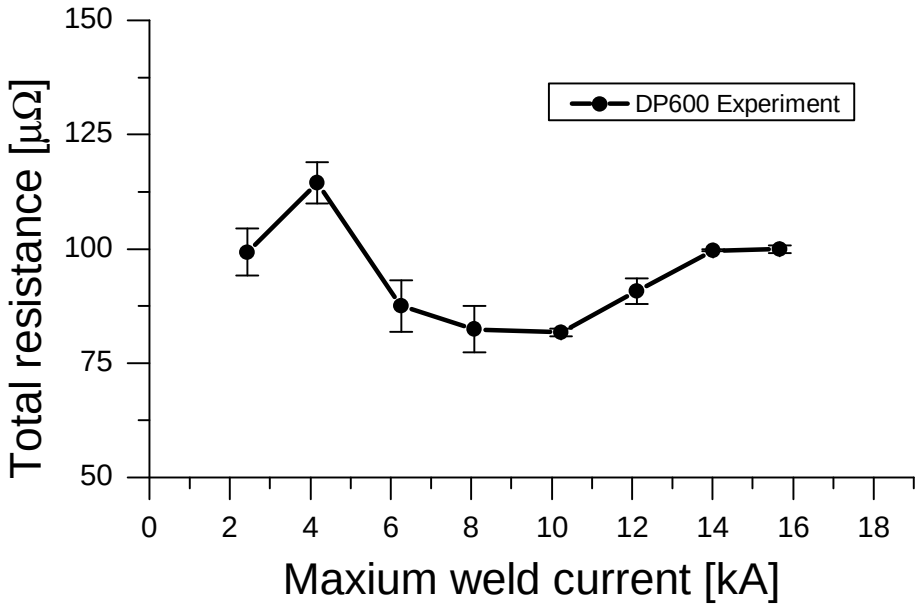

Figure 2.6: Experimental total resistance results for single sheet uncoated DP600-copper contact with new measurement technique. The maximum welding current was taken from the current waveform seen in Figure 2.4.

The experimental results for uncoated low carbon steel-copper contact are shown in Figure 2.7. Three different welding forces were tested which resulted in three different shapes of the total resistance curve. At the lowest welding force of 2.5 kN, total resistance starts at very high values and is always decreasing. This is most likely due to the film resistance contribution from the Rce at the E/S interface. The resistance quickly falls as the oxide lay on the surface breaks down with increasing temperature. At a higher force of 3.5 kN there is a significant

decrease in the total resistance as well as a characteristic peak in the low current range. It is proposed the initial force application in the squeezing stage disturbs the film resistance and flattens the contact asperities which have a result in lowering the resistance. As explained in Figure 2.6, the initial peak is most likely due to surface resistivity and constriction effects. At the highest tested welding force of 4.5 kN, the curve is almost flat, although there is a slight increase at low currents. In this situation the force is large enough to flatten all asperities and eliminate all film resistance.

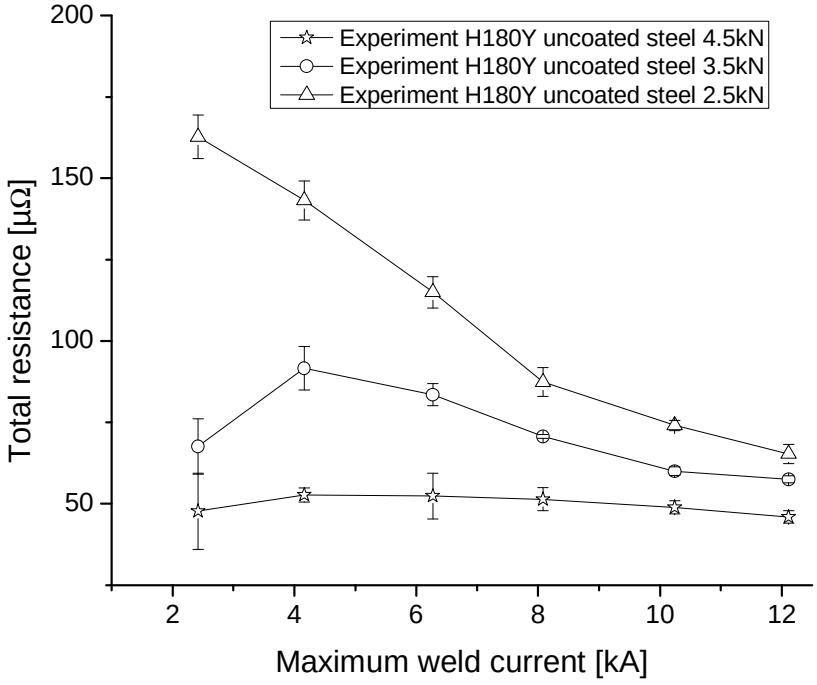

Figure 2.7: Experimental total resistance results for H180Y steel-copper contact using three different welding forces. The higher welding force broke down the film resistance and led to flattening of the curve.

2.3.2 Zinc coated steel-copper contact

The experimental results for galvanized, galvannealed, and electrogalvanized zinc coated steel-copper contact are shown in Figure 2.8. All of the curves are increasing, while the galvannealed steel shows flattening at higher welding currents. Since all of these curves are increasing, it could be said that the film resistance for zinc coated steels is negligible, and the constriction resistance is the only component present. Also, results for galvanized steel and

electrogalvanized steel are similar and very low. This means these zinc coatings have the same Rce values, which is logical because the there is contact between copper and pure zinc in both cases. Due to the low values, it could be the Rce at the E/S interface is completely negligible for galvanized and electrogalvanized coated steels, and thus the only resistance present is the room temperature bulk material resistance. The total resistance values for galvannealed steel are significantly higher, which is most likely due to the increased hardness of the coating from the presence of iron-zinc intermetallic phases and thus difficulty in surface asperity deformation.

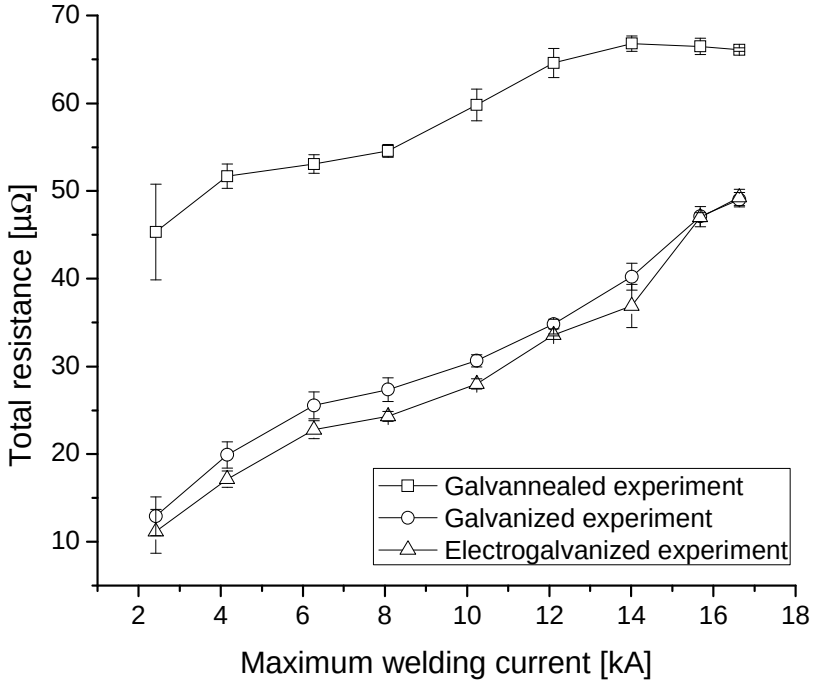

Figure 2.8: Experimental total resistance results for zinc coated steel-copper contact. The total resistance curves show increasing characteristics. Electrogalvanized and galvanized have similar values while galvannealed is significantly higher.

2.3.3 The influence of electrode wear on the Rce curve for galvanized steels

It is also possible to investigate the influence of process variables such as electrode wear with this measurement technique. Figure 2.9 shows two total resistance curves for galvanized steel-copper contact, one test with new electrodes and the second test with worn electrodes after 100 welds. The worn electrodes produced significantly higher total resistance values with a decreasing curve. One possible explanation for an increase in the Rce curve is the slight increase

in contact area from the mushrooming effect. When the electrode contact area increases, the pressure at the E/S interface decreases, and the Rce curve as a function of temperature could perhaps be shifted to higher resistance values due to greater difficulty in asperity deformation. Another more likely explanation for the change in Rce is the possible effect of alloying on the surface of the electrode, specifically the formation of an oxide layer on the surface of the welding electrodes. Gugel et al. [67] proposed the Al present in the Fe-Al-Zn intermetallic layer at the coating substrate interface of galvanized coatings oxidizes during welding to form aluminum oxides that deposit on the electrode face. Since aluminum oxide is a highly resistive coating, elevated electrode face temperatures are expected. This could explain the reason why galvanized steels have the poorest electrode lifetimes. The large Rce values from electrode wear would lead to an increase in the temperature at the E/S interface and thus an increase in the electrode wear mechanisms.

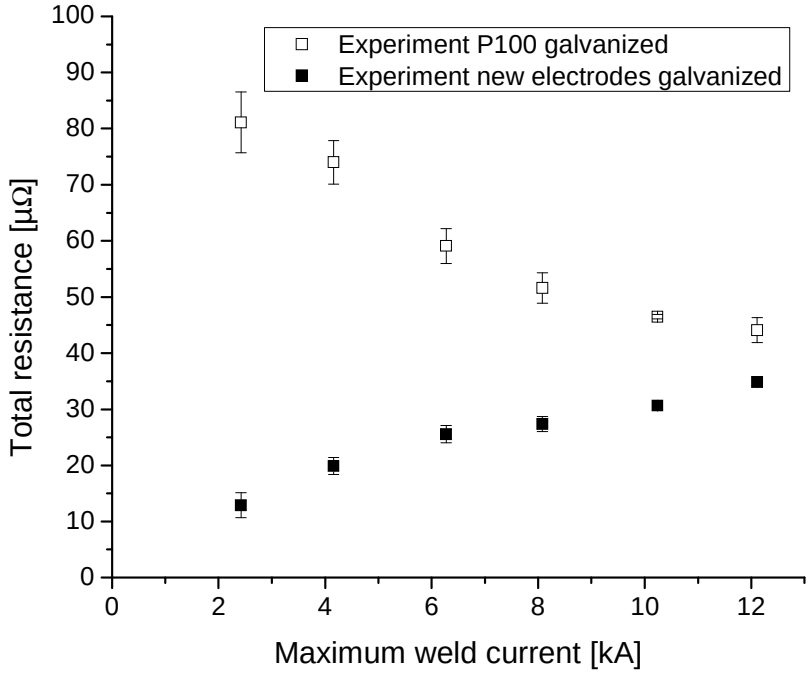

Figure 2.9: Comparison of electrode wear after 100 welding points. The difference in the two data sets is related to electrode wear and the formation of alloy layers on the surface of the electrode which causes an increase in the film resistance.

The experimental results presented in this chapter show the total resistance as a function of welding current. However, it was assumed the welding current and bulk temperature was low enough such that the bulk material resistance did not play a role in the total resistance measurements. If this is the case, then the shape of the Rce curve will be discernable from the proposed experimental results. In order to be sure the total resistance measured in the welding electrodes represents the Rce of the investigated materials, further investigation must be performed to find when the bulk material first becomes measurable. The next chapter will use FEM to find out at which current values the bulk material resistance plays a role in the total resistance measurements.

2.4 Summary and Conclusions

In this chapter an experimental technique to investigate the Rce at the E/S interface was proposed. The total resistance was measured as a function of welding current during the actual welding process using voltage leads in the welding electrodes. Important process modifications including single sheet welding and one period of low AC were made. The advantages of the measuring technique are as follows:

- Single sheet welding experiments which allow for the close investigation of the E/S interface
- Low welding current to limit the bulk material resistance contribution to the total resistance measured in the welding electrodes
- One period of alternating current application and experimental measurements at the peak in the first half wave of current application to create an always increasing temperature at the E/S interface

The experimental results for zinc coated steel and uncoated steel-copper contact are summarized as follows:

- For uncoated DP600 steel-copper contact, a peak in the total resistance was found in the low current range. It is postulated this peak is a real peak in Rce due to competing effects of surface resistivity and asperity deformation.
- The welding force has a significant effect on the shape and values of the total resistance curve. For uncoated low carbon steel-copper contact, low welding forces led to high initial resistance values, while increasing the welding force flattened the total resistance

curve. This is most likely due to the breakdown of surface oxides, which are highly resistive, with increasing force as well as a flattening of surface asperities.

- Zinc coated steel-copper contact showed an increase in total resistance with increasing welding current. Galvanized steel-copper and electrogalvanized steel-copper contacts had very similar resistances, and galvannealed steels had higher total resistances.
- The electrode wear of galvanized steels produced a significantly different total resistance than with new electrodes. The total resistance was much higher for worn electrodes, which could lead to more heating at the E/S surface and an increase in the electrode wear rate.

Chapter 3: A Simulation Based Determination for Measuring Electrical Contact Resistance

This chapter will deal with the validity and verification of the measuring technique which was introduced in Chapter two using the finite element method with the program SYSWELD. Specifically, SYSWELD will be used to find the range of welding currents where only the Rce is measured and not the bulk material resistance. This will consist of numerically manipulating the input Rce and the bulk material resistance curves for each measurement and discovering at which welding current value the bulk material resistance becomes discernable in the total resistance measurements. In doing this, one can be sure the shape of the total resistance curve represents the shape of the Rce for the investigated materials. Also, different shaped input Rce curves will be used in the simulation to determine the influence on the valid welding current range of the measuring technique. Before getting into the numerical results, a brief introduction into the SYSWELD software will be provided.

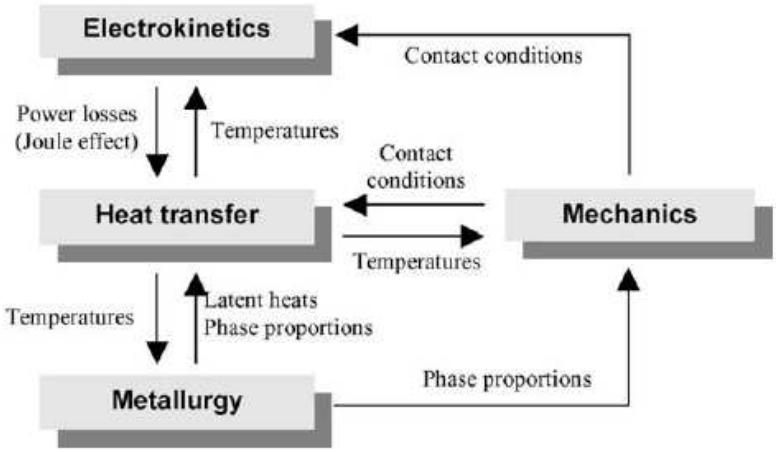

Figure 3.1: Overview of coupling routine in SYSWELD [68].

3.1 Introduction to SYSWELD software

Generally, finite element modeling of the RSW process can be used as a tool to optimize the process parameters such as current, time, and force in order to save production cost and ensure the formation of acceptable welds in terms of size and strength in critical automobile

components. An accurate RSW simulation requires the mathematical coupling of electrical, thermal, metallurgical and mechanical interactions, well-defined boundary conditions, accurate material properties, and, perhaps most importantly, accurate electrical contact radius prediction and the start of the simulation and throughout the current application. An overview of the coupling routine from the FEM program SYSWELD, the commercial software used in this work, is shown in Fig. 3.1 [68].

In RSW there is a significant change in the contact radii between E/S and S/S interfaces during welding due to material softening and electrode sink-in, especially the with spherical tip electrodes which were used in this project. This results in large changes in the temperature evolution and thus nugget formation in the assembly due to changes in the current density distribution. It has been shown the electro-thermal contact conditions related to the evolution of the mechanical contact greatly influence the weld growth mechanism in RSW [69]. The accurate implementation of the coupling procedure between electrical-thermal and thermal-mechanical modules is therefore very important to capture this physical interaction and produce a more realistic predictive model.

3.1.1 Thermal electrical coupling formulation

Electro-kinetics and heat transfer are coupled through the power dissipation from the Joule heating effect with a concentration of the heat generation at the interface between two solid bodies in contact while passing a current. The heat further propagates into these bodies by conduction heat transfer mode associated with the imposed thermal boundary conditions. The electrical phenomena are assumed to be governed by the electro-kinetic model for a frequency close to 50 Hz with temperature dependent electrical conductivity. Considering the Fourier conduction law, the heat transfer in a homogeneous medium is governed by the heat equation with the Joule effect as an internal heat source. A more detailed description including the pertinent differential equation can be found elsewhere [70, 71].

3.1.2 Thermal metallurgical coupling formulation

There are three types of interactions considered between thermal and metallurgical phenomena: metallurgical transformations which depend on the thermal history, metallurgical transactions which are accompanied by latent heat effects which modify temperature distributions, and thermal properties which are phase dependent [72]. The steel materials investigated in this numerical study are characterized by the proportions on the austenite, ferrite,

bainite, and martensite phases. For diffusional transformation, the phenomenological model from Leblond and Devaux was used to reproduce CCT diagram using fast cooling and heating rates [73]. For the martensitic transformation, the Koistinen-Marburger law was used [74]. The thermal conductivity and enthalpy are approximated by means of a linear mixture rule from the thermal properties of each phase, where both thermal inertia effects and latent heat of transformation are considered.

3.1.3 Thermo-metallurgical mechanical coupling formulation

The interactions between thermal, metallurgical and mechanical analyses are due to the following: thermal expansion and thermal strains, the volume changes due to phase transformation, the contact conditions at the E/S and S/S interfaces, and the temperature dependent behavior. The effect of stresses on the metallurgical transformation is not taken into account. Viscoplastic effects are neglected due to the very short times for RSW. The mechanical process is described by the three governing equations, namely the compatibility condition, the constitutive relation, and the equilibrium condition [75].

3.1.4 Contact formulation

The contact states of interfaces are very important in the RSW because they strongly influence the flow of electric current and the heat generation. There are three important parameters that define the contact between two surfaces in SYSWELD: the thermal contact resistance, the electrical contact resistance, and the heat partition coefficient. Thermal electric contact between two surfaces is defined by the user with a threshold value at the E/S interface and an input distance at the S/S interface. If two surfaces are bigger than a threshold distance input by the user, then both surfaces are supposed to exchange heat through radiation and conduction in the air. If two surfaces are smaller, then they coincide and the heat exchange coefficient and the electrical contact resistance depend on temperatures of the surfaces. The model formulation of electro-thermal contact conditions is based on the Gauss quadrature [76]. A more detailed analysis of the contact conditions can be found elsewhere [3, 77-79].

3.1.5 Relevant boundary conditions of RSW model in SYSWELD

Radiative and convective heat transfer coefficients at the boundaries are considered to simulate the heat losses due to the water flow inside the electrode and also the heat flux exchange between the structure and the surrounding. The mechanical boundary conditions are the electrode force applied at the top surface of the upper electrode by assuming a uniform

pressure distribution across the annular end and the vertical nodal displacement of the annular end of the lower electrode [70].

3.1.6 Material properties

The electrical conductivity of the materials and the thermal and electrical contact resistance at the E/S and S/S interface are provided as a function of temperature. The thermal conductivity, density, specific heat, enthalpy, and latent heat are given as a function of temperature and phase. Regarding the metallurgical transformation, the kinetics of the transformation for different heating and cooling rates are given for austenite, ferrite, bainite, and martensite. The mechanical properties are also given as a function of temperature and phase. These include the Young's modulus, Poisson coefficient, thermal strains, yield stress, and strain hardening [71].

3.2 Numerical procedure

A new RSW user interface was created within the framework of this dissertation. It was accepted by ESI company and will now be implemented in all future versions of the SYSWELD software. Appendix A outlines the new RSW interface and further details can be found elsewhere [80]. It was shown that, as well as improving the user friendliness, the efficiency, and the accuracy of temperature prediction compared to the old version, the new interface also allowed for detailed examination and management of the contact surface at the E/S and S/S interfaces.

The goal of the numerical simulation was to determine if the proposed total resistance curve represents the shape of the Rce curve. For simplification purposed, the discussion will first be on one mm uncoated DP600 steel- copper contact. Figure 3.2 shows the simulation mesh used in the analysis as well as the nodes where the voltage drop was measured. Again, as stated in Chapter two, this occurred at the peak of the first half wave of welding current. The mesh was made to match the F1–16-20-50-5.5 electrodes which were used in the welding experiments. The thermal, mechanical, metallurgical, and electrical material properties were taken from the simulation database for DP600 steel. A more detailed explanation of the procedure was published by this author elsewhere [81].

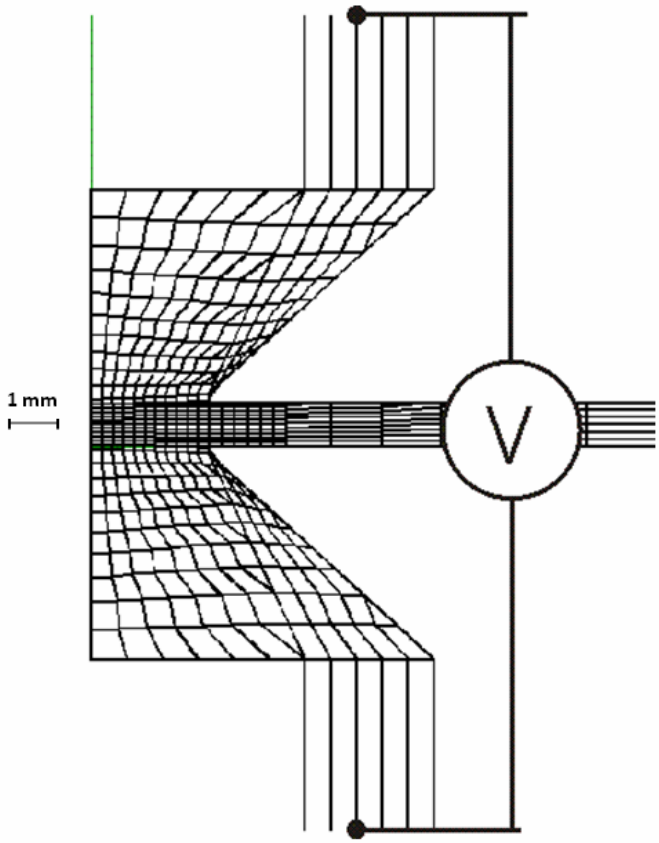

Figure 3.2: Mesh used in the SYSWELD simulation showing nodes where the voltage drop was recorded.

Figure 3.3 shows the important electrical properties of the investigated steel. Three different Rce curves were modelled in the analysis: Rce curve A, Rce curve B, and an Rce curve set to nearly zero (not shown in figure). Rce curve A is the input Rce curve from the SYSWELD database for DP600 uncoated steel-copper contact. This curve was experimentally measured with the device presented in Figure 1.9 [53]. Rce curve B was taken from Babu et al. [48] and has a characteristic peak in Rce. Rce curve B also has relatively higher contact resistance values than Rce curve A. This will allow for the investigation of the Rce value on the welding current in which the bulk material resistance plays a role in the total resistance measurements. For the third curve, the Rce was also set to a near zero value in order to investigate the influence of a RSW simulation with only bulk material resistance effects.

Additionally, two different bulk material resistivity curves were modelled in this analysis: the normal material bulk resistivity curve for steel, which is shown in Figure 3.3 and a second

bulk material resistivity curve set to a room temperature value (not shown on curve). This was performed to investigate only the contribution of the Rce on the measurement values.

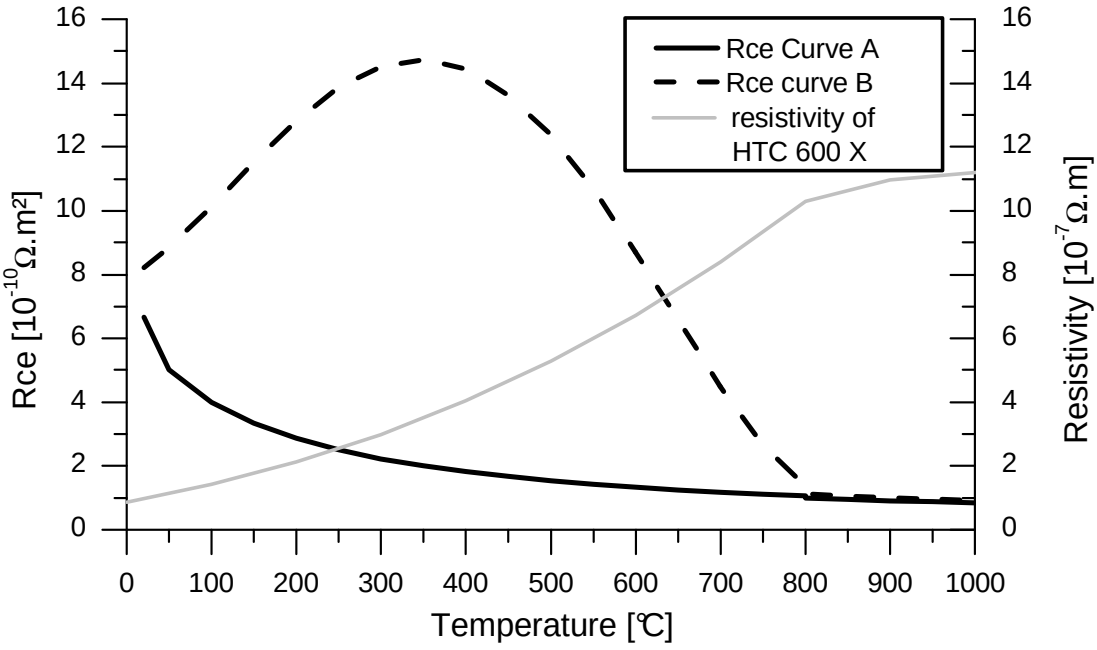

Figure 3.3: Two input Rce curves (A, B) and bulk resistivity used in the simulation of uncoated DP600 steel. Rce curve A: SYSWELD database for uncoated DP600 steel-copper contact: Rce curve B: steel-copper contact from empirical model [48]. The Rce and material resistivity curves were also set to near zero and room temperature values, respectively, for the simulation.

Strong coupling between electrical, thermal and mechanical interactions was used in the simulation which considered sink-in of the welding electrodes during the force application. A strong coupling ratio of 0.1 was used in the simulation, which corresponded to an electro-thermal and mechanical iteration time of two ms. An electrode geometry with 5.5 mm contact face diameter and a curvature of 50 mm was used in the simulation to match the welding electrodes that were used in the experiments. Real time current waveforms of one period AC were input into the simulation ranging from 0.5-9.5 kA in steps of one kA. The new RSW interface also allowed for the implementation of real time current waveforms into the simulation. The welding force used was 3.5 kN, which also matched that from the experiment. The E/S contact radius was altered to match that from the experiment. See Appendix A for more details.

Table 3.1 Overview of single sheet welding simulations

Simulation Test Run	Rce Input Curve A	Rce Input Curve B	Bulk Material Resistance for HTC 600 X	Bulk Material Resistance of constant RT Value
STR 1	**x**		**x**	
STR 2	**x**			**X**
STR 3	**No RCE**		**x**	
STR 4		**x**	**x**	
STR 5		**x**		**X**

Table 3.1 shows an overview of the five different simulation test runs (STR) performed in this analysis. Each of the input Rce curves seen in Figure 3.3 was simulated with normal material bulk resistivity values as well as with only room temperature values. Additionally, a simulation was performed with only bulk material resistance effects.

3.3 Results and discussion of simulation data

The numerically simulated total resistance points from all STR simulations in Table 3.1 are shown in Figure 3.4 as a function of the peak in the welding current of the first half wave of current application. A number of important aspects of this figure must be discussed. The most important is the comparison of total resistance points with standard Rce and material resistivity input values to the total resistance points with only room temperature bulk material resistivity (closed squares/triangles and open squares/triangles, respectively). In the lower current range, the data points from the two different simulations are very close to each other. In fact, the peak in the STR 4 and STR 5 simulations is present. Therefore, regardless of the presence of bulk material resistance, the total resistance values in the lower current range represent the shape of the Rce curve.

The deviation of the total resistance values first starts around six kA for the STR 4 and STR 5 simulations and around 10 kA for the STR 1 and STR 2 simulations. These points represent the first current at which the bulk material resistance plays a role in the total resistance measurements in the welding electrodes. Therefore, there exists a current range below these current values in which the total resistance measured in the welding electrodes is almost exactly the Rce at the E/S interface. This so called valid current range is different depending on the shape and values of the Rce curves. The reason for the different current ranges can be explained as follows. Rce input curve B has much higher values compared to Rce curve A, as seen in

Figure 3.3. This means the interfacial heating in the simulations with Rce curve B is larger. Due to thermal conductivity, the surrounding bulk material heating is also larger, and the bulk material resistance contribution is greater for each current value. Therefore, the bulk material resistance contribution is seen at lower current values for Rce curve B. If the Rce value is higher, the current range where one can measure only the Rce with total resistance measurements in the welding electrodes with the proposed technique will be smaller and shifted to lower welding currents.

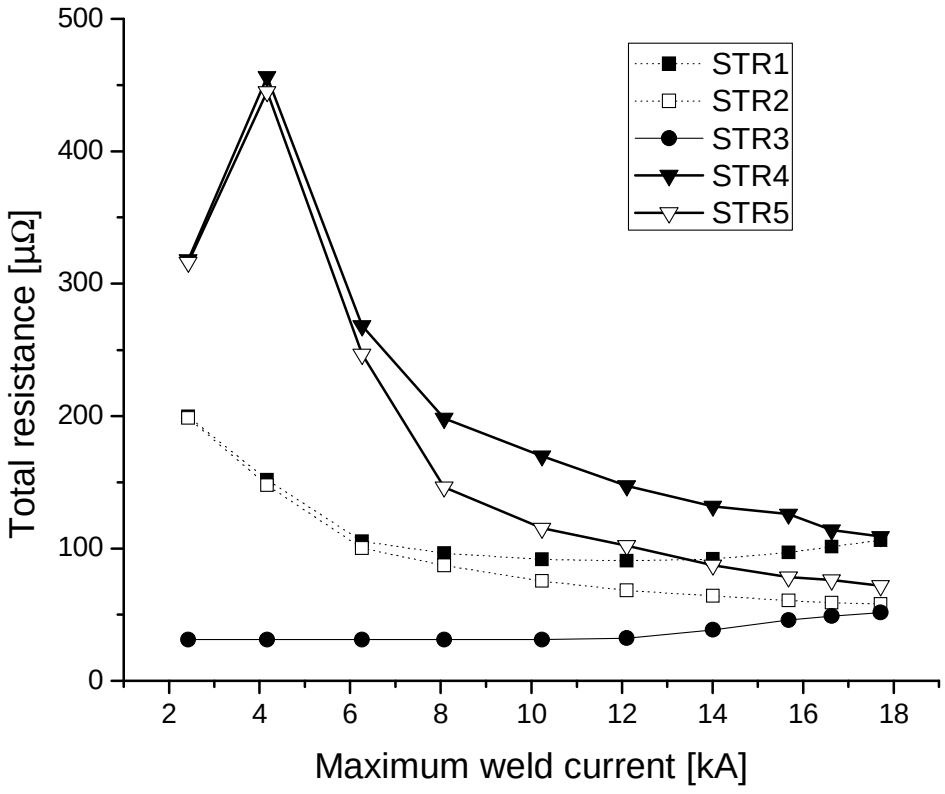

Figure 3.4: Numerical results from all STR simulations. The different curves are in correlation to Table 3.1. The current value where the bulk material resistance plays a role in the total resistance measurements is seen here.

3.3.1 Influence of value of Rce on temperature evolution

In order to verify the results, temperature profiles were examined from simulations in the low and high current ranges. Figure 3.5 shows temperature profiles at two different maximum

currents from STR 4 and STR 5. The temperature evolution is centered about the contact interface in the lower maximum current range (maximum current of 4.2 kA from Figure 3.4). The temperature contours from STR 4 and STR 5 are also very similar in this range regardless of the presence of the contribution of bulk material resistance. Regarding the higher current range (maximum current of 17.7 kA), there is noticeably more heating from STR 4 than STR 5 and the temperature contours are significantly different. This is due to the bulk resistance heating in the sheet, which is much more significant in this temperature range. From the simulation results, it is again proposed only Rce contributions are present in the total resistance curve in the lower maximum current range.

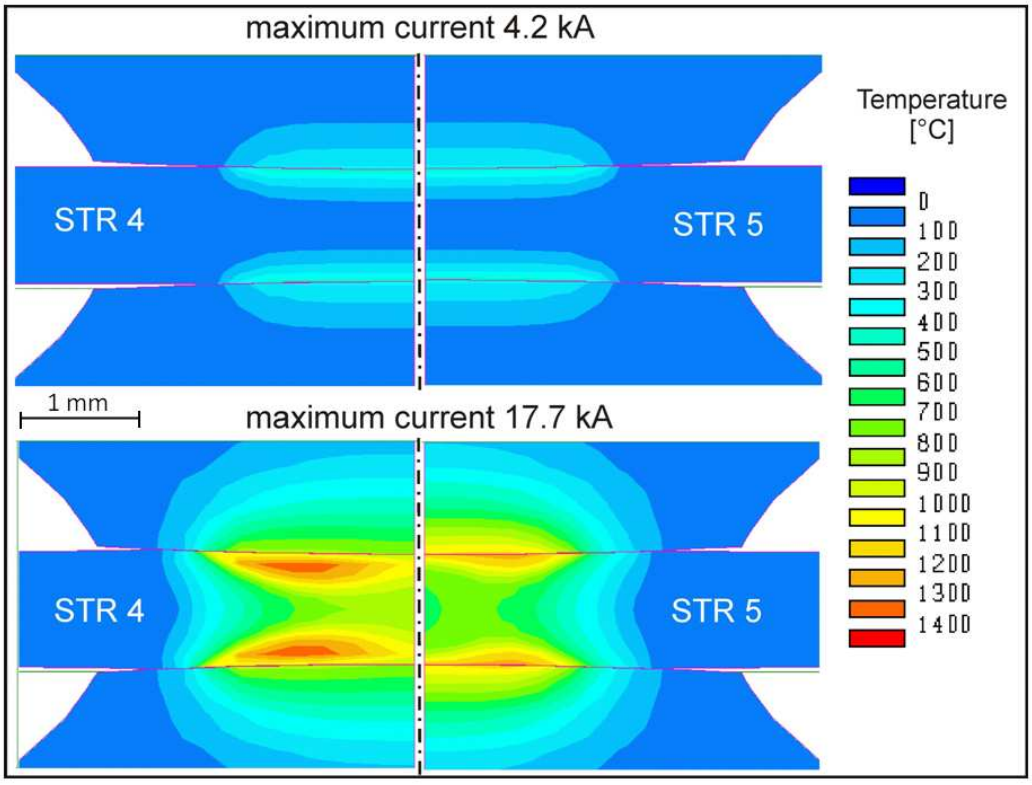

Figure 3.5: RSW SYSWELD simulation for single sheet showing temperature isotherms at two different current values for different Rce Curves A and B (STR4 and STR 5, see Figure 3.4)

The influence of the value of the Rce curve is also seen in Figure 3.6, which displays the temperature evolution at the E/S contact interface at the peak in the first half wave of welding current in the lower maximum current range from STR 1 and STR 4. As the maximum current

increases, the temperature difference at the contact interface between STR 1 and STR 4 is always increasing. These results only verify what was shown in Figure 3.5.

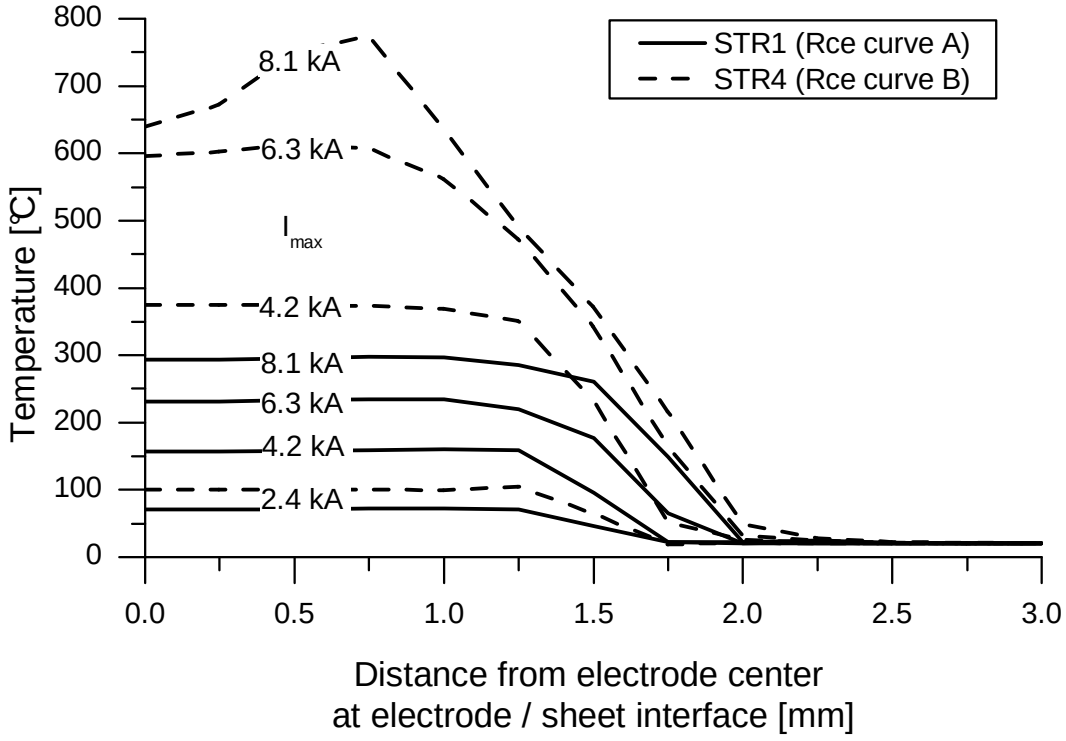

Figure 3.6: SYSWELD simulation showing temperature measurements at E/S interface for STR 1 and STR 4, see Figure 3.5.

3.4 Comparison of experimental and simulation results

The overall objective of this section is to compare the experimentally measured total resistance values and the numerically simulated total resistance values. In most cases, the comparison of experimental and numerical data is performed with the goal to achieve good matching. However, in this special case, it is performed to compare the valid current ranges in which the measurement is acceptable, as well as to see the influence of the input Rce curve on the numerical data.

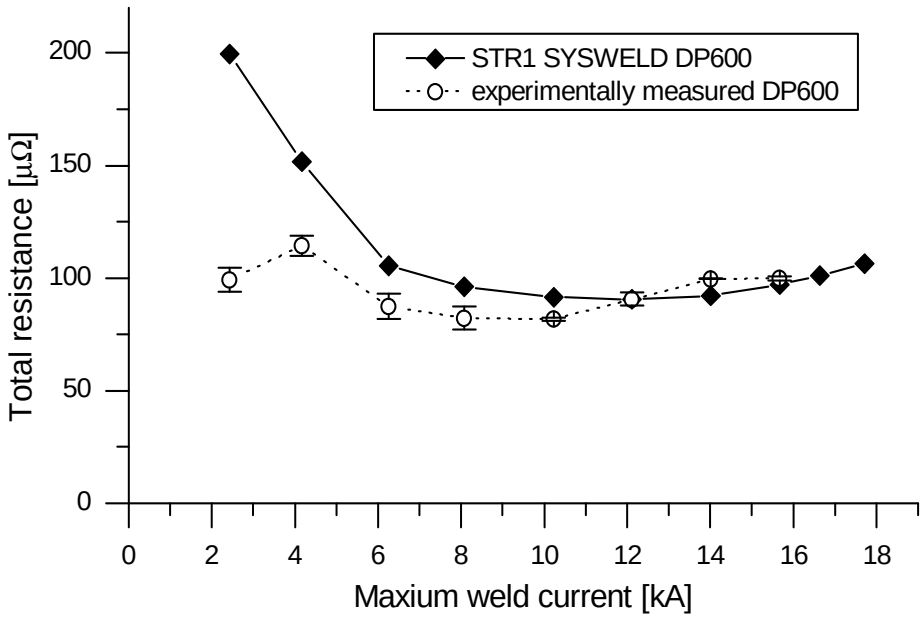

Figure 3.7: Total resistance curve from experimental and simulation for uncoated DP600 steel.

The experimentally measured curve (from Figure 2.6) is compared to STR 1 in Figure 3.7 for DP600 steel-copper contact. The experimental data show similar but lower resistance values compared to the simulation. According to the numerical results, the total resistance data for STR 1 represent the Rce with only room temperature bulk resistance effects until around 10 kA. Since the experimental data is lower than the numerically simulated data, it can be said the experimental total resistance data corresponds to the Rce at the E/S interface at least up to 10 kA. From the experimental results, an increase in the total resistance is also seen after 10 kA. At this point, the contribution of the bulk material resistance, which increases with temperature, outweighs the contribution of the Rce. Thus the peak measured in the experimental data is an actual peak in the Rce curve and the experimental measurement technique is thus accurate in measuring the shape of the Rce curve.

There is good matching between experimental and simulated data at higher welding currents but not at lower currents. The main reason for the difference between experimental and numerical total resistance values in the lower current range is the difference in the input Rce curve and the actual Rce curve. Rce curve A in Figure 3.3 shows the input Rce curve from SYSWELD for uncoated DP600 steel-copper contact at the E/S interface. This is an always

decreasing Rce curve until flattening occurs. In reality, as determined by the experimental measuring technique and validated with the numerical simulation, the actual shape of the Rce curve for uncoated DP600 steel-copper contact at the E/S interface has a peak in the curve at lower temperatures. If the actual Rce curve were input in the RSW simulation, then there would be very good matching between the experimental and numerical data in Figure 3.7.

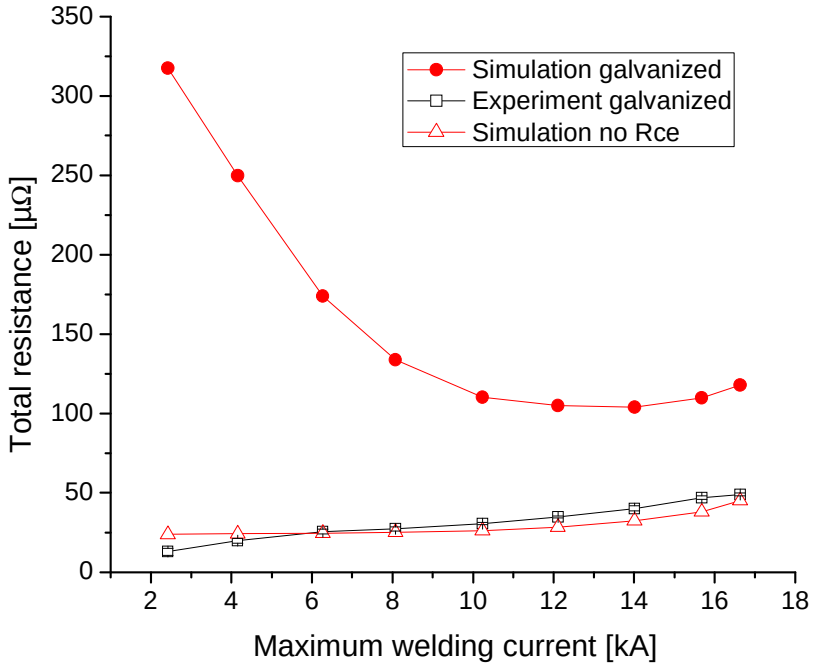

Figure 3.8: Comparison of total resistance results for galvanized steel-copper contact to simulations with and without Rce.

The numerical results for galvanized steel and low carbon steel-copper contact are shown in Figures 3.8 and 3.9, respectively and are compared to experimental total resistance results. The SYSWELD input Rce curve for galvanized steel-copper contact was used for the numerical results shown with red circles. The red triangles represent simulations with a near zero value of Rce, or simulations with only bulk material resistance effects. The total resistance values from the simulation of galvanized steel with the input Rce curve are significantly higher than the experimental results. The reason for this is the large value of the Rce curve used in the simulation. When this input Rce curve is set to near-zero, the experimental values and the simulation values show much better fitting and are almost identical. Thus, the Rce at the E/S interface for galvanized (and electrogalvanized) steels is negligible. This result was also

proposed elsewhere [81, 82] but has not been universally accepted in the RSW community. For uncoated low carbon steel-carbon contact the numerical results are again significantly higher than the experimental data. These findings support the need to have accurate Rce data in simulation programs.

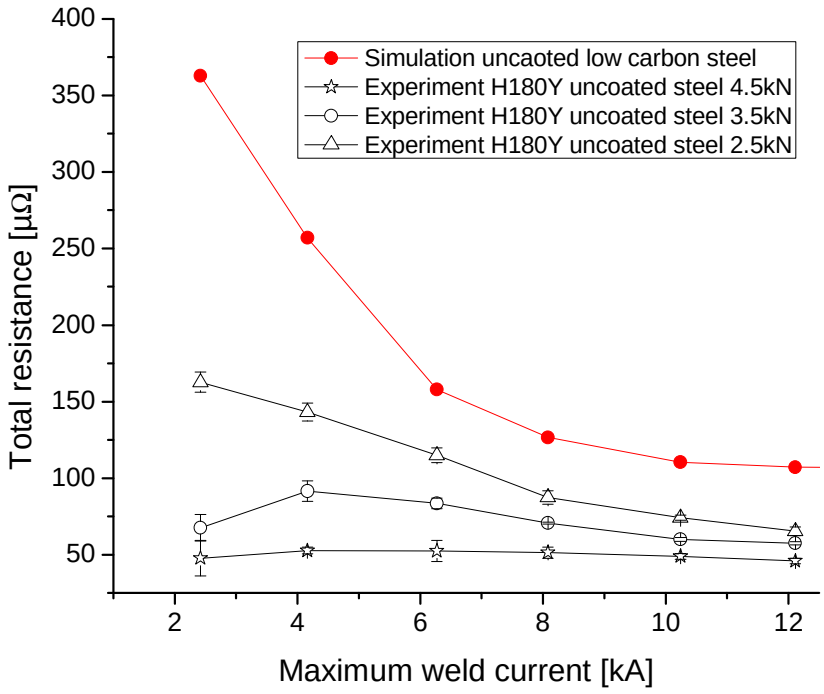

Figure 3:9: Comparison of low carbon steel-copper contact with numerical simulation.

3.5 Summary and conclusions

The FEM program SYSWELD was used to perform RSW simulations to verify the accuracy of the experimental measurement technique which was proposed in Chapter two. The input Rce and bulk material resistivity curves were manipulated in the simulation in order to discover at which current value the bulk resistance played a role in the total resistance measurements. In doing so, a current range was found in which the Rce could be measured with total resistance in the welding electrodes. Overall, it was determined with the numerical analysis that the newly proposed method for experimentally measuring the Rce during welding is very accurate regarding the shape and values of the Rce curve in the low to medium range of applied

currents. Increasing the value of the Rce led to a decrease in the valid current range where the Rce could be evaluated without the bulk material resistance coming into play.

The numerical results were compared to the experimental results for the materials investigated in this work. In all cases, the input Rce curves from the SYSWELD database did not accurately represent the shape and the values of the Rce curve, causing mismatching in the total resistance values. Specifically, the Rce at the E/S interface for DP600 steel-copper contact had a peak at lower temperatures. Also, the Rce for galvanized and electrogalvanized coated steel-copper contact was found to be negligible.

The overall goal of this work is to extract Rce vs. temperature curves from these experimental total resistance values. In order to do this, however, the total resistance must be converted to Rce, and the temperature must be known at the E/S interface. The next chapter will involve a numerical optimization procedure to determine the values of the Rce and to estimate the contact interface temperature.

Chapter 4: The numerical optimization of the contact interface temperature using finite element modeling

4.1 Introduction

The main goal of this chapter is the estimation and optimization of the unit area Rce (with the units Ohm m^2) curves as a function of interface temperature at both the electrode-sheet (E/S) and sheet-sheet (S/S) interfaces for the materials investigated in this work. This is a continuation of the previous two chapters in which the shape of the Rce curve was experimentally measured as a function of welding current. Here, the finite element method will be used to first separate the bulk material resistance contribution from the total resistance values. Then, the contact interfacial temperature at the E/S and S/S will be optimized for both single sheet and double sheet welding experiments. The main idea of this procedure is to vary the contact interface temperature in the input Rce curve in SYSWELD using a stepwise, trial and error approach to match the simulated total resistance to the experimental total resistance. The exact numerical procedure will be introduced and discussed for zinc coated steels. It will be shown the proposed numerical procedure is applicable for all material/coating combinations provided a databank of the investigated material as well as the experimental resistance values.

The newly proposed Rce curves as a function of temperature for copper-steel and copper-zinc coated steel combinations at the E/S interface, and steel-steel and zinc-zinc combinations at the S/S interface will then be calculated and compared to previous Rce curves from literature. The validity of this technique will be discussed with regards to the accuracy of the results. Additionally, the influence of interfacial pressure due to a change in welding force on the results and shape of the curve will be discussed. The newly determined curves will be used in a RSW simulation and the results will be compared to experiment with regards to the shape and size of the HAZ and molten zone.

4.2 Model definition and numerical procedure

A summary of the SYSWELD simulation routine can be found in Chapter two while a detailed explanation of the model definitions, boundary conditions, and the coupling between electro-kinetics, heat transfer, and metallurgy can be found elsewhere [3]. The weak coupling thermal simulation option was used in this numerical optimization procedure. Simulations were

performed with a modified RSW interface as described in Appendix A which allowed the user to input a threshold for the electro-thermal contact between the flat sheet and curved electrode surface to determine the actual contact radius of the electrode [83]. Special attention was taken to ensure the initial contact radii in the simulation program at the E/S and S/S interfaces matched exactly to the experimental radii measured with the stereoscope. The new RSW interface also allowed for the implementation of actual current waveforms into the simulation. The two-dimensional axis-symmetrical mesh is shown in Figure 4.1 with an electrode geometry matching the electrodes from the welding experiments. A total of 55 contact elements were used across the length of the electrode contact radius. The element length along the contact radius was small (0.05 mm) in order to account for small increases in the contact radius.

RSW simulations were performed on a single and double sheet for low carbon, DP600, and zinc coated steel materials using real time, one period effective current values of 0.5 to 9.5 kA, exactly like in the experimental welding procedure from Chapter two. The voltage drop was recorded during the time of the peak of the first half wave of welding current at the top of the electrode and across the contact interfaces. The average temperatures across the contact interfaces were also taken from the simulation and analyzed at the peak in the first half wave of welding current.

Simulations were performed with a near zero Rce value at the contact interfaces to act as a reference point for the numerical optimization procedure. A stepwise trial and error procedure was then implemented, starting with the lowest welding current setting, to optimize the average interface temperature and thus the Rce curve so the resistance values from the simulation matched the total resistance values from the experiment. The contribution of the bulk material resistance was numerically separated from the total resistance to get the estimated Rce value. A detailed description of the procedure will now be given below in the next section with reference to the experimental and simulation results.

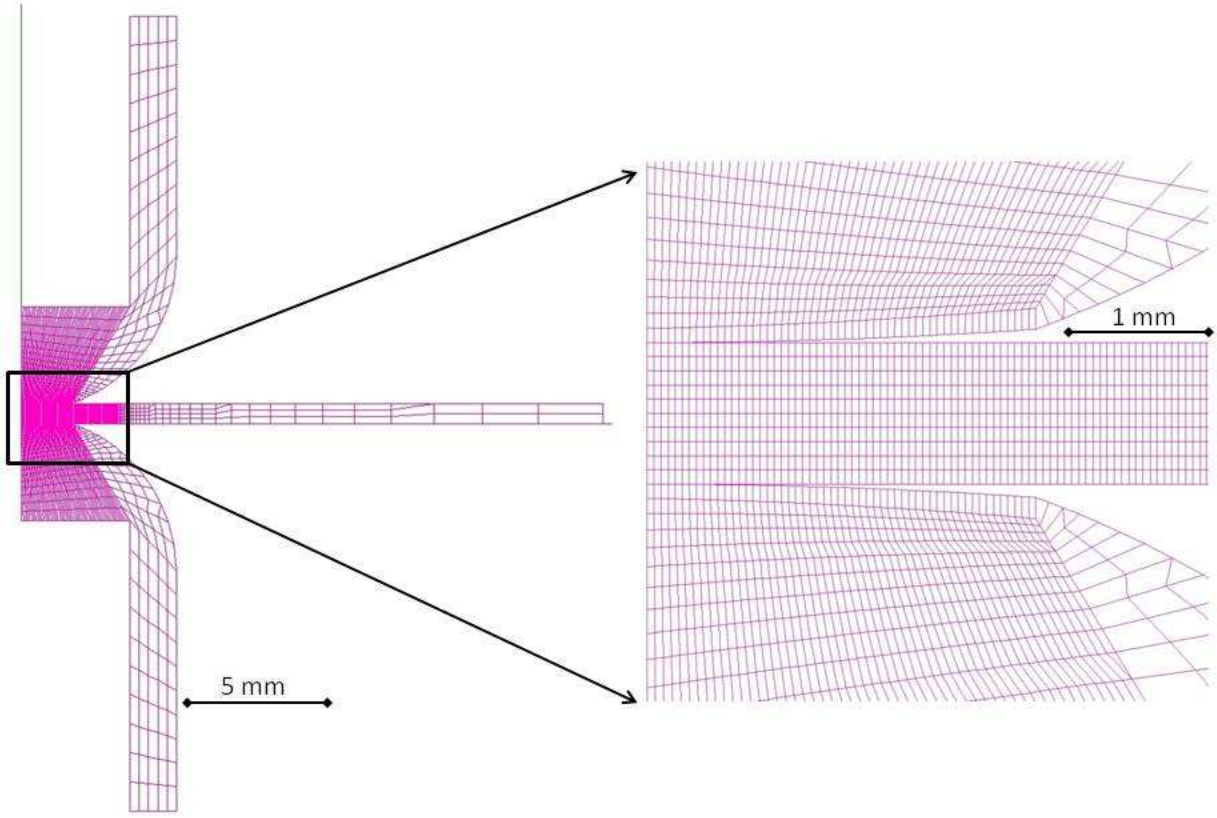

Figure 4.1: Overview of the mesh used in the RSW simulation

4.3 Results and discussion of Rce curve optimization: galvannealed steel-copper contact

The procedure to optimize the input Rce curve in the simulation will first be described with galvannealed low carbon steel-copper contact at the E/S interface. Afterwards the procedure will be applied to the S/S interface. Finally, the results will be presented for the remaining materials that were investigated in Table 2.1 and then compared to the Rce curves from literature.

The experimentally measured total resistance data is shown in Figure 4.2 for galvannealed steel-copper contact along with the simulated total resistance values from SYSWELD in red. The SYSWELD simulation was performed with a near zero value of Rce. The overall goal of the numerical optimization technique was to alter the input Rce vs.

temperature curve in a stepwise approach to match the total resistance values in the simulation to the experimental values for each current setting. In order to change and optimize the input Rce curve, the following three parameters must be known for each current setting:

- the actual Rce value
- the actual contact area
- the interface temperature when the voltage drop measurement occurred (at the peak of the first half wave of AC)

The actual Rce resistance value was first estimated at room temperature to give a starting point for the analysis. At higher current values, the bulk material resistance contribution was numerically separated from the experimental total resistance to give the Rce value, which will be explained in more detail. The contact area was taken from experimental stereoscope measurements and combined with the Rce values to make the unit area Rce value. Finally, the interface temperature was optimized with a numerical procedure and the help of FEM and will later be discussed.

4.3.1 Determination of room temperature Rce as starting point

In order to begin the stepwise procedure for optimizing the Rce curve, a starting point must be chosen at room temperature. It was assumed the first current input in the experimental procedure (0.5 kA effective current) was sufficiently low enough to induce an interface temperature around room temperature at the peak of the first half wave of current. This assumption was numerically checked with SYSWELD in the following manner. Using a trial and error approach, a constant Rce value was input in the simulation and the total resistance was numerically measured. Depending on the total resistance values, this constant Rce value was either raised or lowered until the total resistance from simulation matched that from the experiment, as shown with the arrow in Figure 4.2. The constant Rce value which matched the simulation data to the experiment data was around 7E-11, as shown in Figure 4.3. Therefore, if a simulation was performed with the unit area Rce value from Figure 4.3, the simulated total resistance from Figure 4.2 would match that from the experiment.

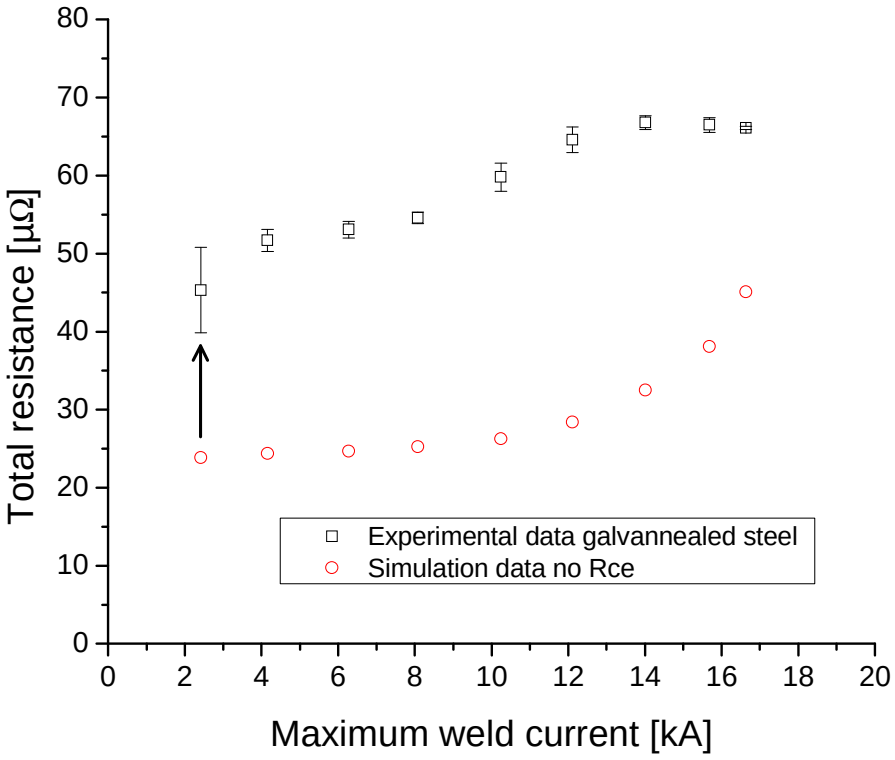

Figure 4.2: Comparison of experimentally measured and simulated total resistance values at 2.5 kN welding force for galvannealed steel-copper contact. The input unit area Rce curve was changed to match the numerical and experimental total resistance values.

One very important detail must now be discussed which is the basis for the interface temperature optimization. It is not necessary for the curve shown in Figure 4.3 to extend until the melting point of the material when performing a RSW welding simulation at the first current step, 0.5 kA effective current. Rather, it is only necessary to define this curve until the maximum average temperature of the contact interface at the time of the voltage drop measurement, or at the peak in the first half wave of current application. The average temperature is the average between two adjacent nodes on the electrode and sheet contact surface. This average contact interface temperature at the peak of the first half wave is shown in Figure 4.4. The values are sufficiently close to room temperature. Therefore, an assumption can be made here for a starting point (20°C, 7E-11 Ohm m^2), which will be the starting point for the input unit area Rce curve in SYSWELD.

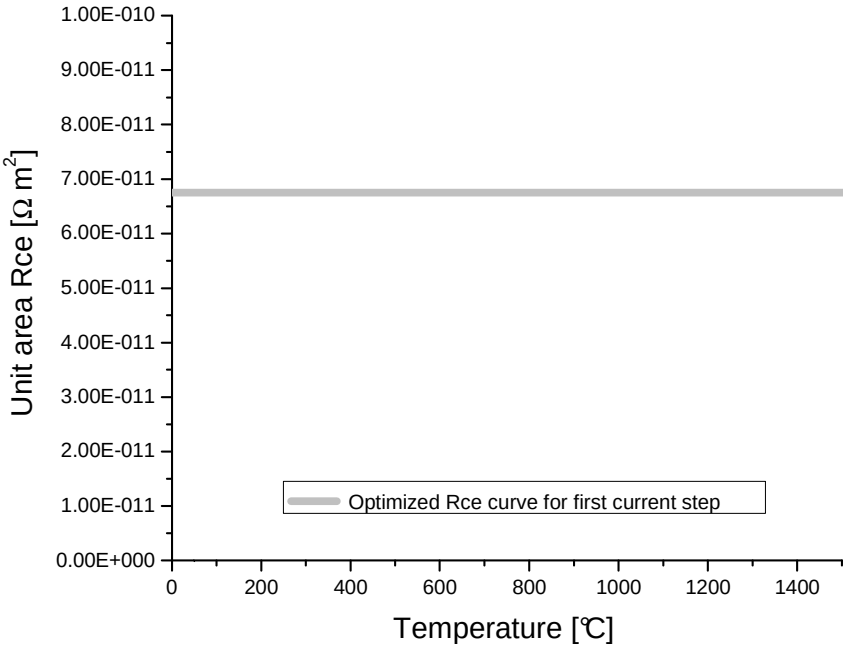

Figure 4.3: Optimized Rce curve for first current step. Value is constant until melting temperature of steel.

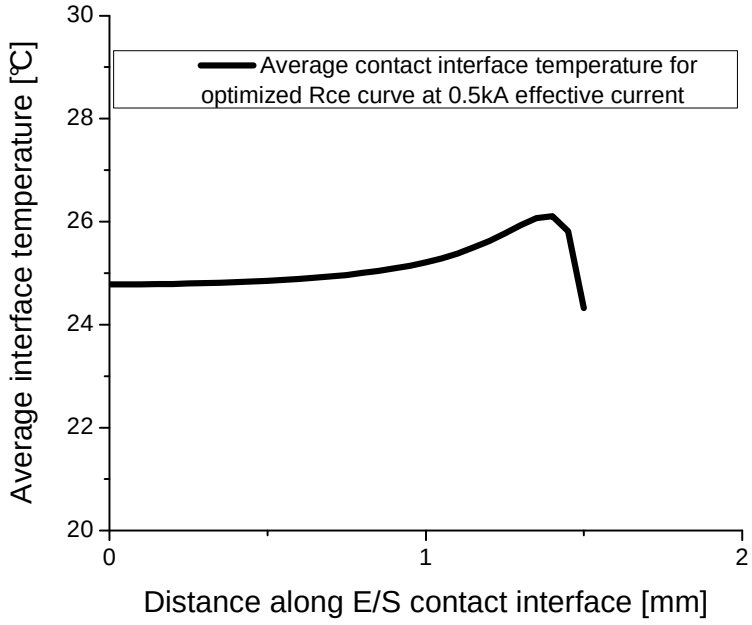

Figure 4.4: Average temperature across the E-S contact interface at 0.5 kA with optimized Rce curve. This temperature was taken at the peak in the first half wave of welding current.

4.3.2 The separation of the bulk material resistance and Rce from the total resistance

As mentioned above, in order to optimize the Rce curve for the next current setting (1.5 kA effective current), the following three variables must be known: the Rce value, the contact area, and the interface temperature. This section will explain how the Rce value was estimated for the input Rce curve. For the Rce value, an important assumption was made in order to make an accurate estimation. It was assumed the bulk resistance contribution from the previous current step in the analysis (0.5 kA in this case) was very close to the bulk resistance contribution in the existing current step in the experiment. In other words, because the welding current increase between current steps was relatively low, the bulk material resistance contribution between successive current steps is similar.

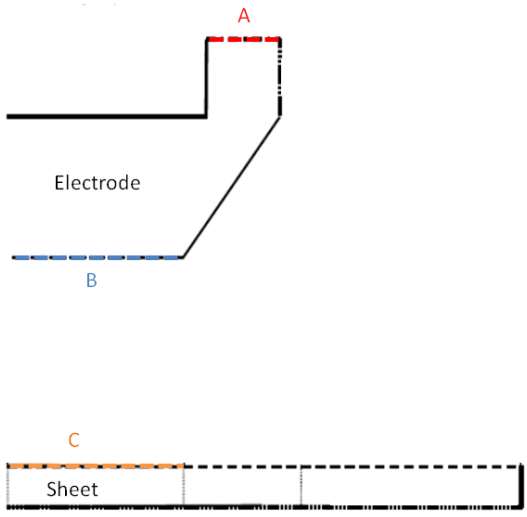

Figure 4.5: Schematic representation of important surface element groups used in the analysis numerical calculation of the total resistance, Rce, and bulk material resistance. Group A: application of welding current, Group B: electrode contact surface, Group C: sheet contact surface [68].

The bulk material resistance increase at a given current step is numerically determined in the following way. Figure 4.5 shows the group of important skin elements on the electrode and sheet used in the simulation routine for calculating the total resistance, the Rce, and the bulk material resistance. At the peak of the first half wave of current application, the voltage drop was taken at the following three groups of skin elements: A, B, and C. Group A is where the current is applied. Group B is the contact surface of the electrode. Group C is the contact surface of the sheet. The average voltage drop was then determined from the results at the nodes, with special

attention to take only the nodes which are in thermal-electrical contact for the latter two element groups. The total resistance is calculated using Ohm's law, the peak in the first half wave of welding current and the average voltage drop across group A. The Rce contribution (at one E/S interface) is also calculated using Ohm's law where the voltage is the difference in the average voltage drop across group B, and group C. The Rce contribution subtracted from the total resistance would give the numerical bulk material resistance contribution for that current step. It can be seen that, for a current step *n*:

$$R_{bulk_n}^{simulation} = R_{tot_n}^{simulation} - 2R_{ce_n}^{simulation} \tag{4.1}$$

This equation seems rather obvious because the total resistance is just the sum of the Rce at the two E/S interfaces, and the bulk material resistance contributions of the electrodes and sheet.

Once the bulk material resistance contribution is determined for the first current setting, it is possible to move to the next currents setting (1.5 kA effective current). The estimated Rce value to be input in the unit area Rce curve in the simulation was taken as the experimentally measured total resistance value from the existing current setting minus the numerically calculated bulk resistance value from the previous step, multiplied by the experimental contact area. This is represented in the following equation:

$$R_{ce_n}^{simulation} = (R_{tot_n}^{experiment} - R_{bulk_{n-1}}^{simulation})\, A_n^{experiment} \tag{4.2}$$

Where $R_{bulk_{n-1}}^{simulation}$ was previously determined in Eq. (4.1). Again, for Eq. (4.2) to be accurate, the bulk resistance increase with increasing current step must be very small.

4.3.3 The optimization of the interface temperature of unit area Rce curve

The interface temperature is the final unknown variable and must be optimized again in a trial and error approach. Figure 4.6 shows three hypothetical Rce curves (A, B, C) used in the numerical procedure for the optimization at the 1.5 kA effective current setting. All curves have the same room temperature Rce value as a starting point, as found from the previous optimization at 0.5 kA effective current. They also share the same peak unit area Rce from the assumption explained above in Eq. (4.2). Directly after the peak in Rce, there is a sharp discontinuity and the curves immediately drop to a near-zero value. The reason for this immediate drop is to assist in the determination of the optimum interface temperature. This drop allows the simulation program to tell the user when an underestimation of the contact interface

temperature occurs. If there exists a temperature on the E/S interface above the maximum temperature of the unit area Rce curve, then the Rce is near-zero or negligible at this region in the FE mesh. This situation will be represented by a drop in the total resistance value in the simulation. Thus, the optimized average interface temperature for the input unit area Rce curve is that which exists just above the maximum average interface temperature at the peak of the current application.

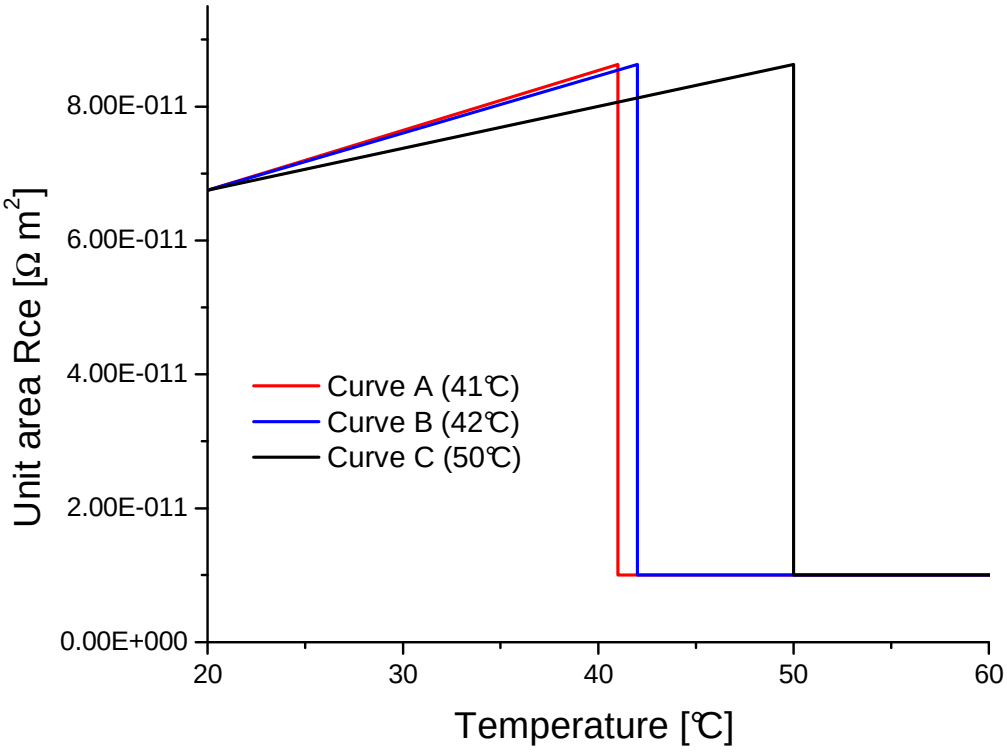

Figure 4.6: Proposed Rce curves for optimization of the interface temperature in the second current step. The only difference between the curves is the interface temperature. The immediate drop in the Rce values after maximum results in a large drop in total resistance when an underestimation in the interface temperature occurs. Each curve was tested in the simulation and the total resistance was numerically calculated and compared to the experimental values.

In the following explanation, the procedure for the selection of the optimum contact interface temperature will be discussed while referring to Figures 4.6 and 4.7. Figure 4.7 displays the average contact interface temperature measured at the peak in current for each proposed Rce curve (color coded to Figure 4.6 with solid lines) in relation to the maximum estimated interface temperature (color coded with dotted line). The Rce curve B (blue) in Figure 4.6 represents the

optimized unit area Rce curve because the interface temperature, as shown by the solid blue line in Figure 4.7, is just below the maximum Rce temperature of 42 °C, as shown by the dotted blue line. For Rce curve C from Figure 4.6, the average interface temperature, which is represented by the solid black line in Figure 4.7, is well below the proposed Rce temperature of 50 °C. Thus, 50 °C is an overestimation of the contact interface temperature for this current step. Considering the Rce curve A the average interface temperature extends just above the dotted line, or just above 42 °C, at the edge of the contact interface, causing a situation where this portion of the contact interface has a near-zero Rce contribution due to the drop in the unit area Rce curve after this temperature. This condition greatly affects the total resistance value measured in the electrodes due to the thermal/electrical coupling in the FE simulation, as will be shown next.

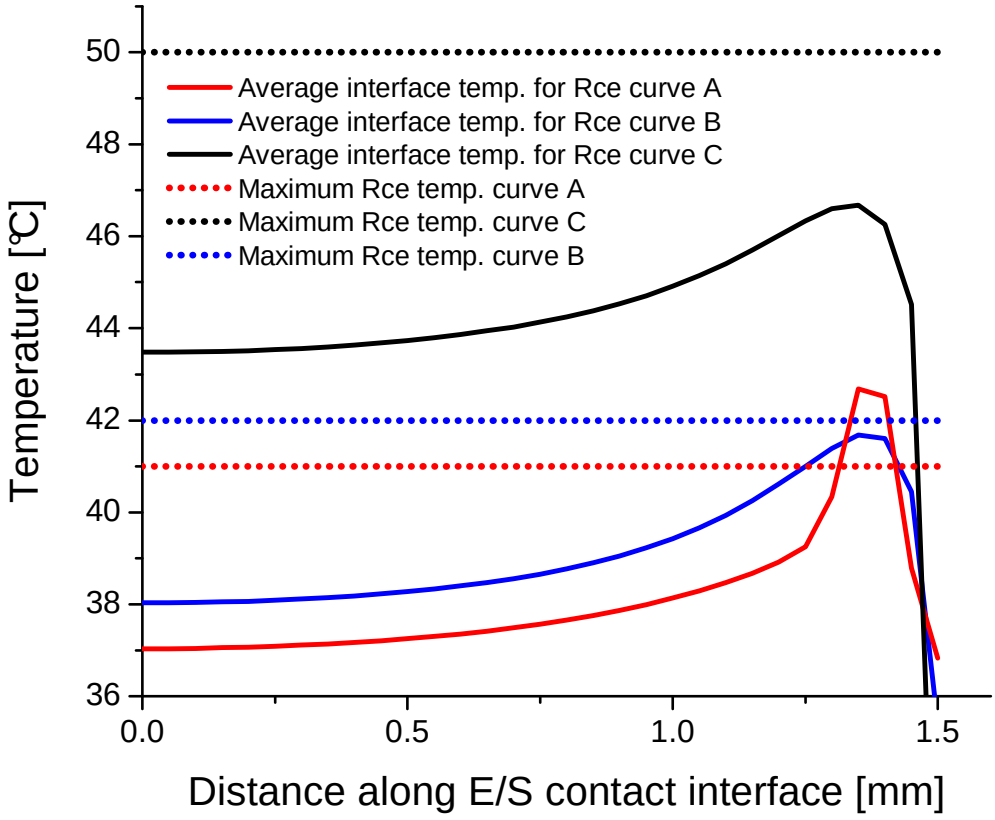

Figure 4.7: Average contact interface temperature taken from the numerical simulation at the peak in the first half wave of welding current for Rce curves A, B, C. The temperature at the maximum of the Rce curves are shown with dotted lines and color coded. When the average interface temperature is high than the maximum Rce temperature, there exists a zero-resistance value in the FE mesh at this point.

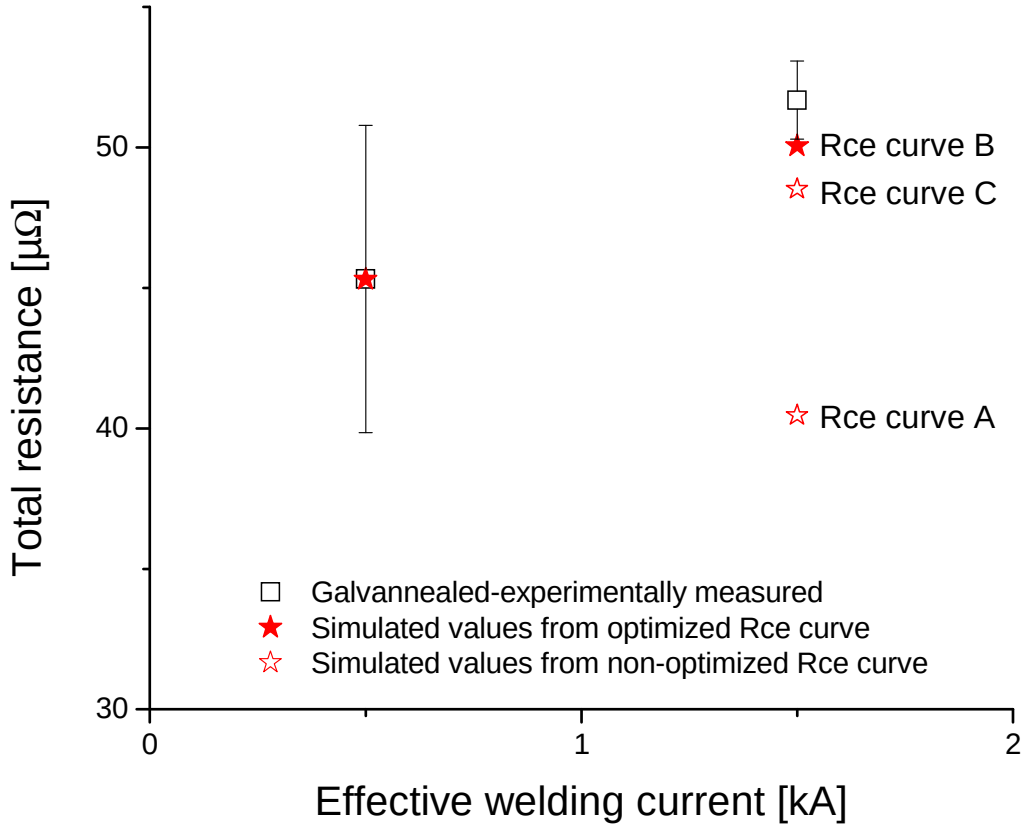

Figure 4.8: Comparison of experimental and numerically simulation resistance values for galvannealed-copper contact in the low current range. The filled red stars represent values from the optimized Rce curves.

Figure 4.8 compares the experimental total resistance values with the optimized total resistance values from the simulation in the low current range. At 1.5 kA, the total resistance values for the three proposed unit area Rce curves in Figure 4.6 are labelled and shown. As expected, the optimized interface temperature, or Rce curve B, has a numerical total resistance value that is closest to the experimental value. At 41 °C, or with the Rce curve A, the simulated total resistance drops suddenly to a value around 40 μOhm. In other words, although Rce curve A and Rce curve B are very close, their simulated total resistances are significantly different. Again, this is due to the trend shown in Figure 4.7, where the E/S interface temperature exceeds the maximum temperature of the Rce curve. This situation results in a portion of the FE mesh on the E/S interface with a negligible Rce contribution (the voltage drop in this portion of the mesh

is much lower due to a negligible Rce). This situation is reflected in a much lower total resistance value in the welding electrodes. Regarding Rce curve C, the numerical total resistance value does not fall within error of the experimental values. In this case, there is an overestimation of the interface temperature which results in a smaller slope in the unit area Rce curve and thus lover Rce values at the same temperature setting compared to Rce curve B (see Figure 4.6). Therefore, the total resistance is lower for this curve compared to Rce curve B.

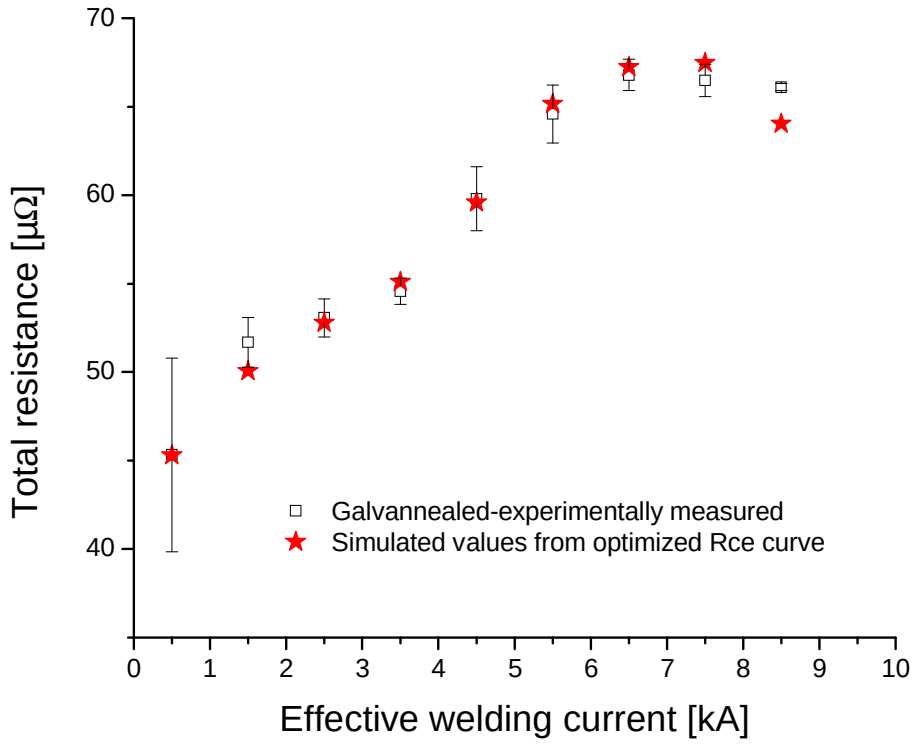

Figure 4.9: Comparison of experimental and numerical optimized total resistance values for galvannealed-copper contact. Very good matching was found after the numerical optimization procedure.

4.3.4 Discussion of the validity of numerical results

The procedure presented in sections 4.3.2 and 4.3.3 was then performed at each current step to optimize the entire unit area Rce curve. The results of the numerical optimization procedure for galvannealed steel are shown in Figure 4.9. All of the red stars represent the total resistance value with optimized Rce curves. The simulated resistance values fall well within the error bars apart from those at effective currents of 1.5 and 8.5 kA. The possible reasons for these

discrepancies will now be discussed. Due to the nature of the optimization procedure, each simulated data point and thus each optimized Rce curve is very dependent on the experimentally measured resistance values from the previous current step (see Eq. (4.2)). At 0.5 kA, there exists the most scatter in the experimental reading. This scatter is most likely the reason for the initial disagreement between experimental and simulation data. In the last current step, the reason for the disagreement is most likely due to an inaccurate estimation of the bulk resistance at higher current values. Thus, Eq. (4.2) becomes less accurate at higher currents due to an increase in the bulk material resistance between the current steps. Figure 4.10 shows the actual simulated increase in bulk resistance from the optimized Rce curves in this analysis using Eq. (4.1) for each current step. It is seen that, in the lower current range, the bulk resistance increase in almost negligible. As the current increases, the bulk resistance contribution also increases, which could lead to some inaccuracy in the method of optimization.

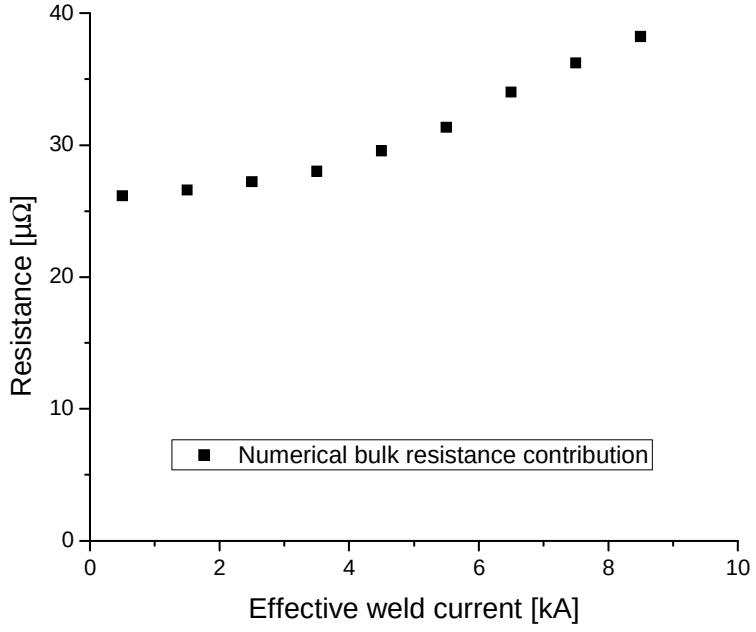

Figure 4.10: Simulated increase in bulk material resistance contribution for each current step after the completion of the numerical optimization procedure for galvannealed steel-copper contact. An increase in the bulk material resistance at higher currents could be the reason for some error in the optimization procedure. Numerical results are taken from equation (4.1).

The proposed unit Rce curve for galvannealed steel-copper contact after completion of the numerical optimization procedure is shown in Figure 4.11. The interface pressure is estimated at around 350 MPa, but is not constant in every welding current step due to electrode sink in. The curve has a continuously increasing resistance with increasing temperature until a peak is reached at around 360 °C. As mentioned earlier, an increase in the Rce could be attributed to an increase in the surface resistivity due to constriction resistance effects. An increasing Rce until a peak is reached before the melting of the coating was also experimentally measured by Rogeon et al. [53]. The shape of the curve matches very closely to the shape of the experimentally measured total resistance values as a function of welding current.

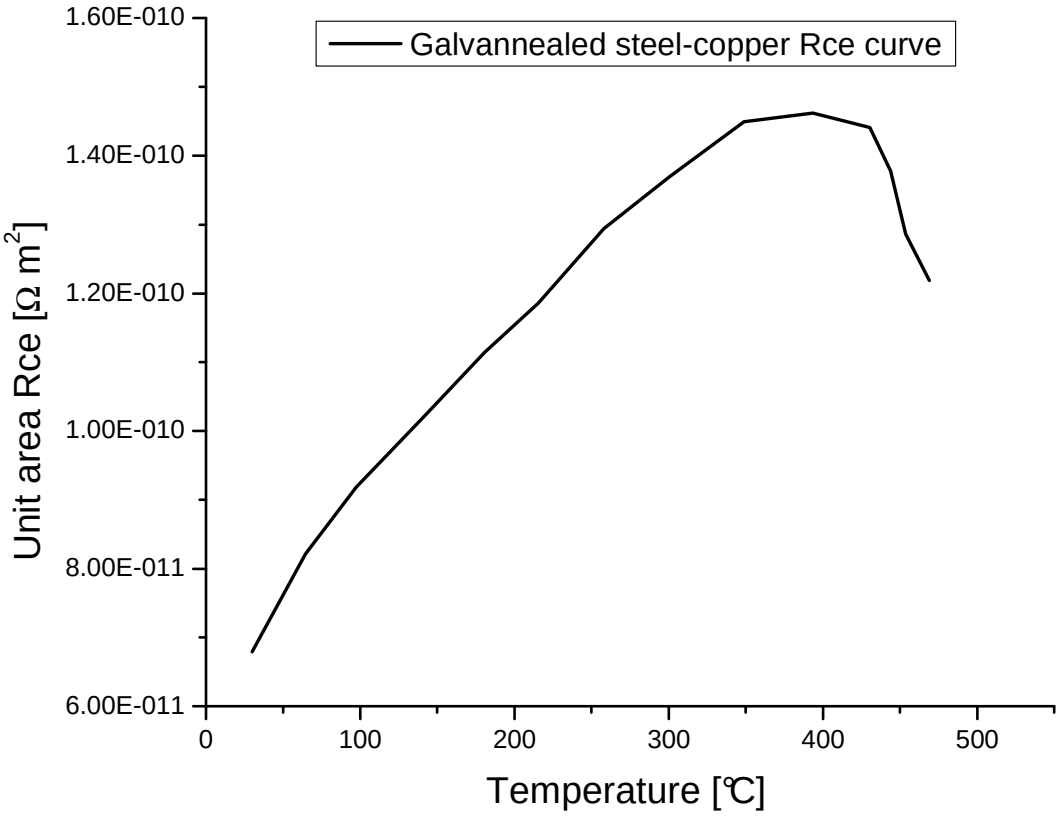

Figure 4.11: Proposed Rce curve for galvannealed steel-copper contact using the numerical optimization procedure. The estimated contact pressure was around 350 MPa. A curve smoothing procedure was applied.

4.3.5 The influence of contact area on the numerical optimization procedure

There is a very strong influence of the E/S contact area on the value of Rce. Therefore, the contact area must be accurately estimated from the experiment. Figure 4.12 shows an experimental stereoscope image of the contact surface taken at the end of one period of current application. Four different diameter measurements were taken for each current setting, and the results are shown in Figure 4.13. Also seen in Figure 4.13 are the simulated E/S contact radii. The experimental contact radii remain constant until an effective current of 3.5 kA. Thus, electrode sink-in of the curved electrode is not significant in the lower current range and the initial contact radii after impact is the same at the first half wave of current application in this current range. Also, the simulated contact radii are the same as the experimental up to 3.5 kA effective welding current. However, at 4.5 kA, the electrode first begins to sink into the sheet and the contact radii increase with each successive welding current step in the experiment. However, in order for the resistance values in the simulation to closely match those from the experiment, it was required to set the simulated contact radii to a lower value than the experimental results. It is important to note the experimental contact radii were measured after one period of current application, or after the second half wave, and the resistance measurements that were being compared and optimized occurred at the peak of the first half wave. It is therefore reasonable to believe the actual contact radii at the peak in the first half wave of welding current to be very close to the proposed contact area used in simulation and shown in Figure 4.13 in red.

Figure 4.12: Stereoscope top down image of contact surface at the end of one period of current application

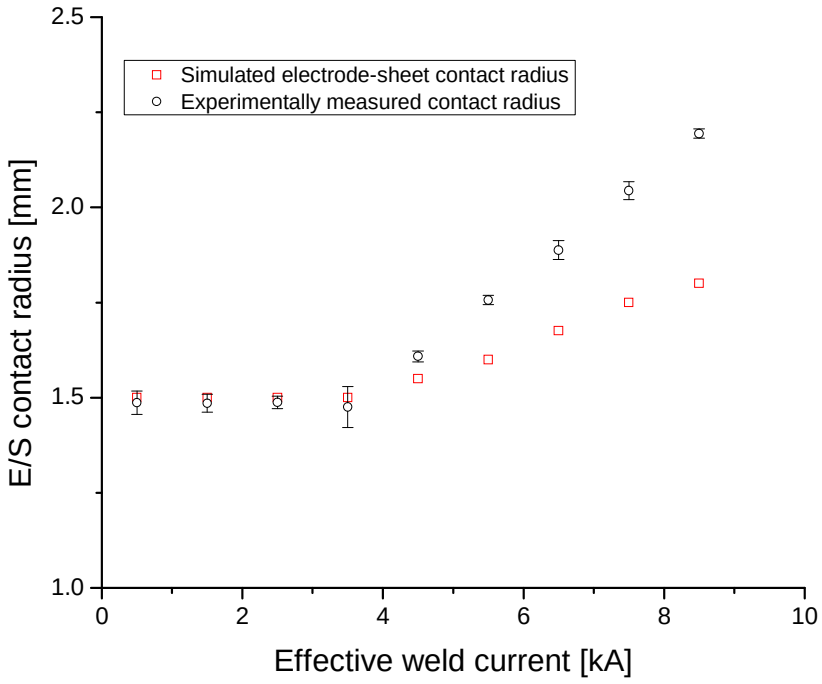

Figure 4.13: Experimentally measured and numerically simulated E-S contact radii for galvannealed material.

4.4 Application of optimization procedure to sheet/sheet contact interface for galvannealed steel

Determining the Rce curve at the S/S interface using the proposed numerical procedure is more complicated than for just the E/S interface. It is first essential the unit area Rce curve at the E/S interface is determined with the numerical optimization procedure. The room temperature Rce value is determined the same way as in the single sheet experiments. However, the input Rce value for the next current step follows a different equation, as shown here:

$$R_{ce}(S/S)_n^{simulation} = (R_{tot}{}_n^{experiment} - R_{bulk}{}_{n-1}^{simulation} - kR_{ce}(E/S)_{n-1}^{simulation})\, A_n^{experiment} \quad (4.3)$$

In principle, this equation is similar to Eq. (4.2) for the single sheet experiments, but there is an added component that must be subtracted from the experimental total resistance, namely $R_{ce}(E/S)$. Not only must the bulk resistance contribution be numerically determined at the peak of the first half wave of welding current, as explained before in section 4.3.2, but also the contribution of the Rce at the E/S interface. There is also an added correction factor *k*, which considers that the increase or decrease in the Rce contribution at the E/S interface between subsequent welding current steps is not negligible but it is rather significant in most cases. If there was no correction factor in the equation, it is possible the input Rce at the S/S interface is either overestimated or underestimated, depending on whether the Rce at the E/S interface is decreasing or increasing, respectively. The constant *k* is usually between 0.8 and 1.2 for good fitting to experimental data, and equals 1 when the Rce at the E/S interface does not increase between current steps or is negligible (as is the case for galvanized steels as will be later shown). For increasing Rce, *k* is greater than one while for decreasing Rce, *k* is less than one. In case of galvannealed steels, *k* is around 1.1.

The experimental total resistance data for double sheet experiments on galvannealed low carbon steel is shown in Figure 4.14. The data has a characteristic increase in the total resistance which is similar to the single sheet results in Figure 4.2. The simulated total resistance results are also shown in red after the numerical optimization procedure was performed. The optimized interface temperature was determined in the same manner as described above for the single sheet experiments. The simulation data show good correlation in the lower current range. However, as the current increases, there is mismatch between the optimized resistance from simulation and experimental data. There are two possible explanations for the mismatch. One is that the

correction factor *k*, whose value is determined by the slope of the Rce curve, is not accurate and must be adjusted according to the change in slope of the Rce curve. The other explanation involves the increase in bulk material resistance. As previously mentioned for the single sheet analysis, as the current increases, the increase in the bulk material resistance between subsequent steps also increases (Figure 4.10). Regarding the double sheet experiments, there is a greater contribution from the added sheet as well as from the added S/S interface heating contribution.

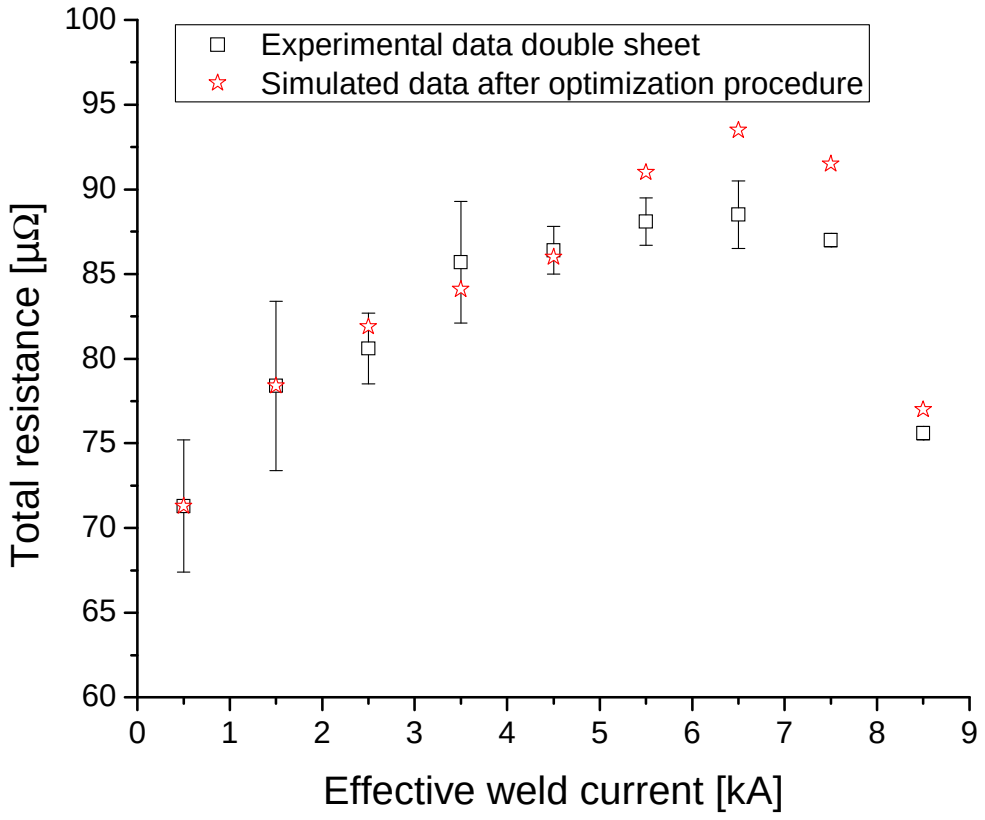

Figure 4.14: Experimental and simulated total resistance data for double sheet welding experiments for galvannealed steels. Simulation data after the optimization procedure is shown in red.

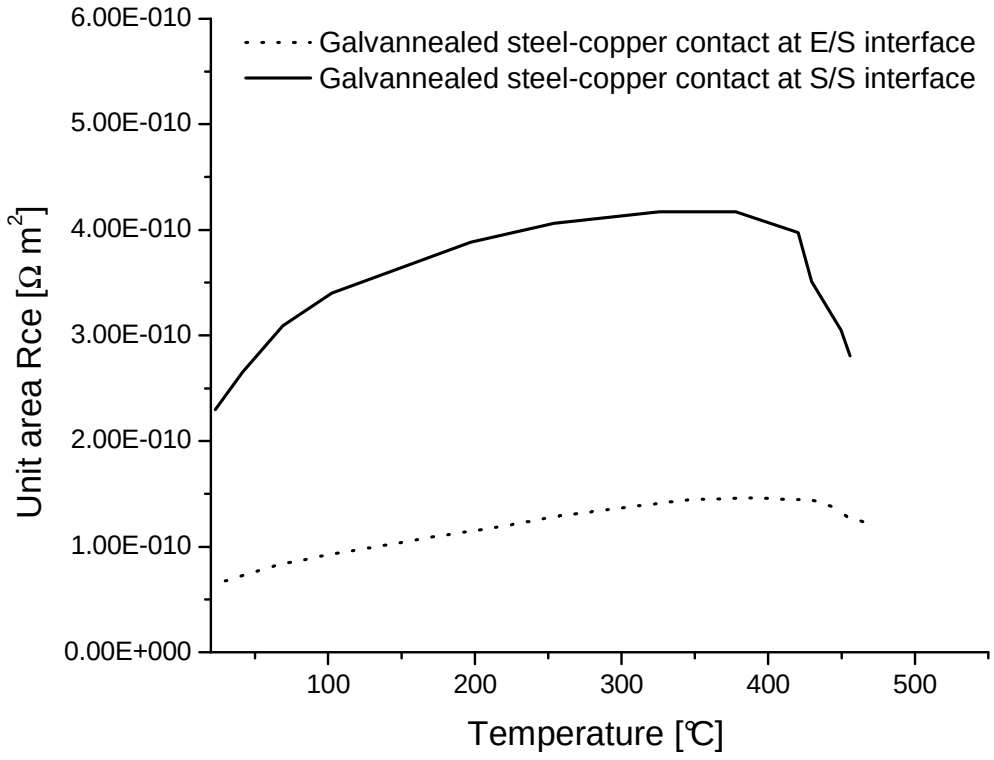

Figure 4.15: Rce curve at S/S for galvannealed steel compared to curve at the E/S interface. A curve smoothing procedure was applied.

The numerically optimized Rce curve at the S/S interface for galvannealed low carbon steel is shown in Figure 4.15. The Rce curve at the E/S interface is also shown for comparison. The shape of the curves is similar and they are both increasing until a peak is reached before the melting of the coating.

4.5 Galvanized and electrogalvanized low carbon steel numerical optimization

It was previously determined in Chapter 3 that the Rce at the E/S interface for galvanized and electrogalvanized low carbon steel was negligible. Therefore, this section will discuss the S/S interface for these materials. The total resistance data for double sheet experiments is shown for galvanized and electrogalvanized low carbon steel. Only one data set was produced for the two materials because their total resistance values were almost identical. The simulation data is also shown in the curve in red after the numerical optimization procedure was performed. A

decreasing trend is present for the total resistance data as seen in Figure 4.16. Eq. (4.3) was used in the determination of the input Rce value in this example as well. However, considering the assumption that the Rce at the E/S interface is negligible for the investigated materials, there is no contribution from the term $R_{ce}(E/S)$. Almost all of the simulated resistance data fall within the standard deviation of the resistance measurements from the experiment. The numerically determined Rce curve for galvanized and electrogalvanized low carbon steel is given in Figure 4.17 with a characteristic exponentially decreasing shape. It is interesting to note that in all cases, the shape of the total resistance curve is the same as the shape of the Rce curve at the S/S interface.

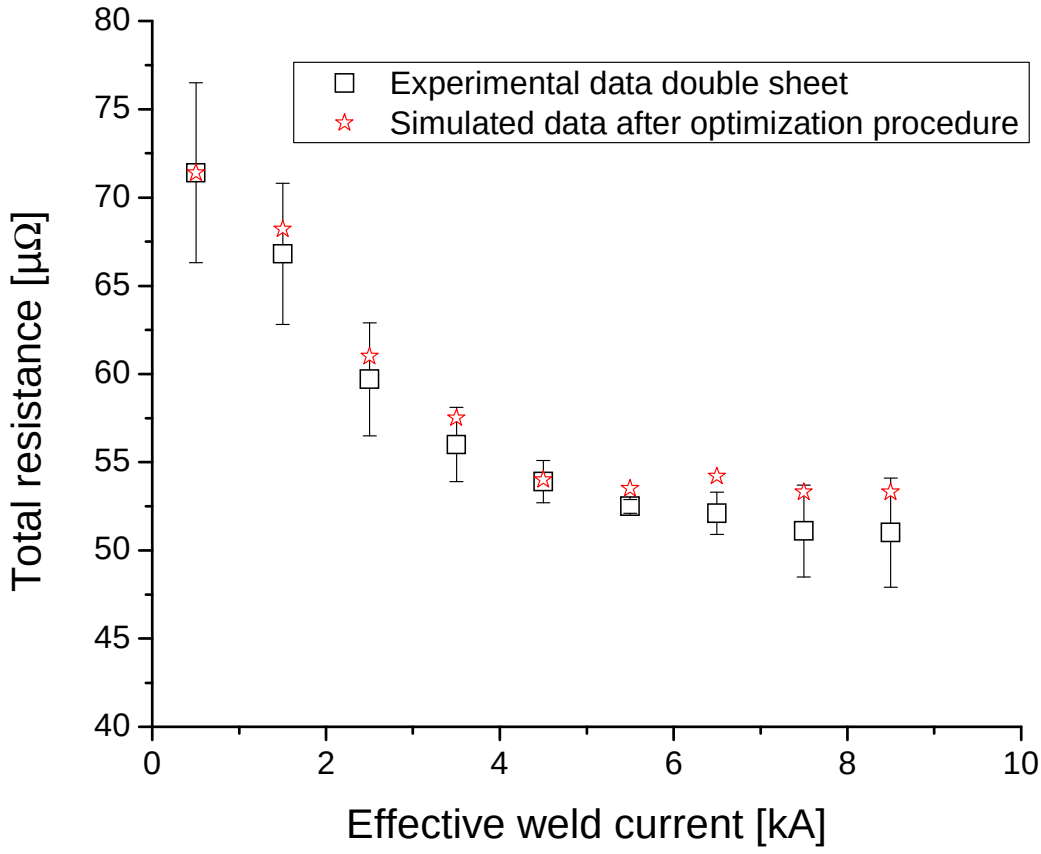

Figure 4.16: Experimental and simulated total resistance data for double sheet welding experiments for galvanized and electrogalvanized steels. Simulation data after the optimization procedure is seen in red.

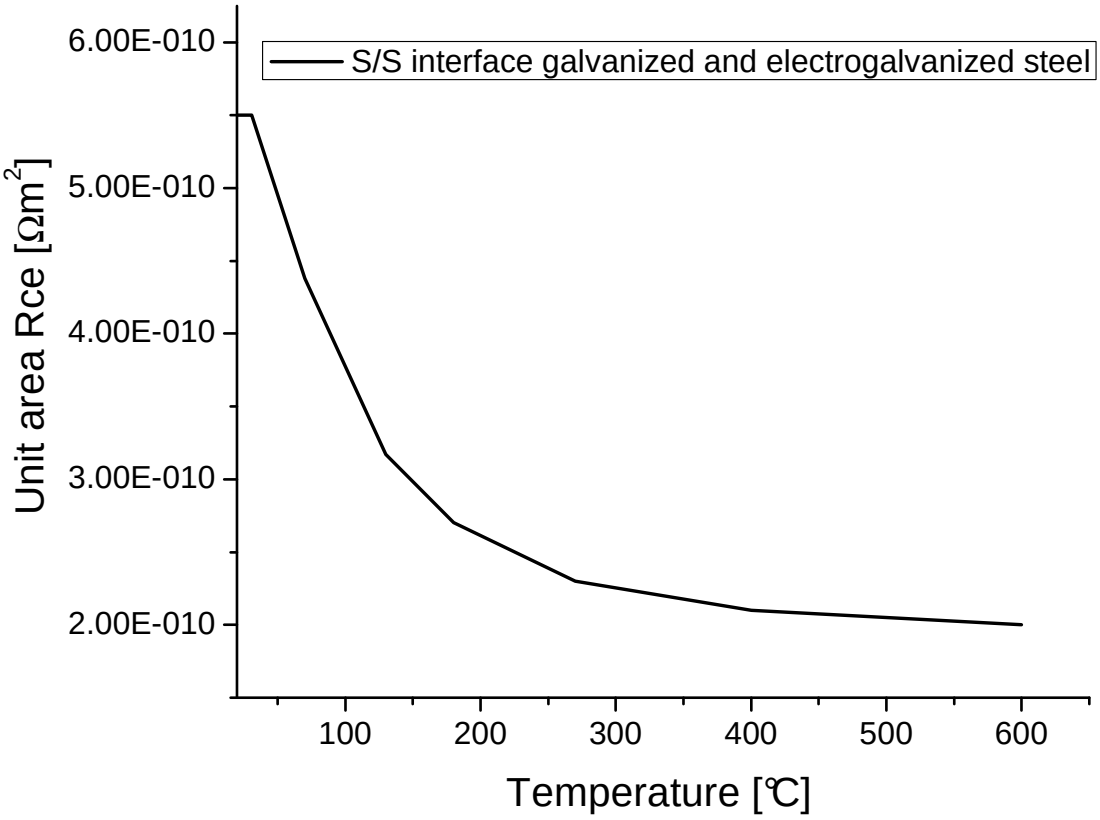

Figure 4.17: Numerically determined Rce curve for galvanized and electrogalvanized coated steels at the S/S interface after optimization procedure.

4.6 Comparison of results to literature

The results from the numerical optimization procedure will now be compared with literature. Most of the curves taken from literature were measured with the ex-situ technique as described in Chapter 1. Figure 4.18 displays Rce curves for low carbon galvanized steels at the S/S interface. The numerically determined curve using the present analysis has the lowest value of Rce, which could be due to the significantly higher interfacial pressures during the testing procedure. The input curve from SYSWELD, as shown in red, is more than an order of magnitude higher. This could be a reason for a potentially large source of error in the simulation of the RSW process. The shape of the curve measured by Thieblemont [52] is similar to the numerically determined curve, although its values are still much higher. Rogeon et al. [53] measured an increasing curve until a peak was reached just before the melting point of the zinc

coating. A similar curve shape was found with for galvannealed steel-copper contact, as seen in Figure 4.15. Overall, there is a large discrepancy in the Rce shape and values from the different authors.

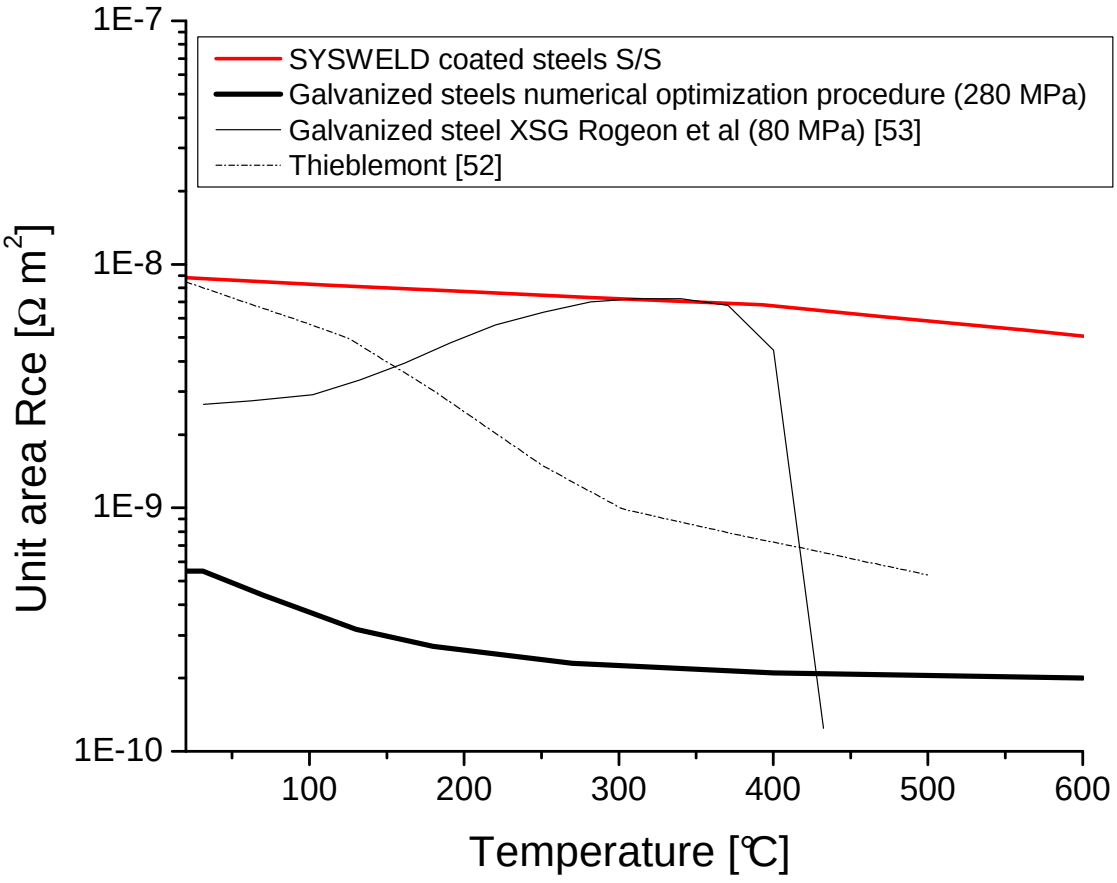

Figure 4.18: Comparison of numerical determined Rce curve with those from literature. All curves are for galvanized low carbon steel at the S/S interface.

4.6.1 Uncoated steel contact and the E/S interface

The numerical optimization procedure described was utilized for uncoated material combinations as well (see Table 2.1). The results for blank, low carbon steel and DP600 at the E/S interface from the numerical optimization procedure are shown in Figure 4.19 and compared to literature and also from the SYSWELD simulation program for different interface pressures. Two different Rce curves for low carbon steel-copper contact are presented (blue and green curve) at different welding forces to investigate the influence of interfacial pressure. At higher

interface pressures, the Rce curve is significantly lower for copper-low carbon steel contact. There exists a peak in the Rce curve at higher interface pressures at around 75 °C. The reason for the peak in the curve as well as lower values at the higher interface pressure could be attributed to an oxide layer on the surface of the steel. As explained by Crinon et al. [44], the oxide film resistance is still present at lower interface pressures and thus the Rce curve begins at a high resistance value and exhibits an exponential-like decrease with increasing temperature. As the interfacial pressure increases with welding force, the oxide layer is immediately broken down with the application of the electrodes during the squeezing stage of welding. This may allow for constriction effects to take place in the presence of true metal-to-metal contact, as explained by Bowden et al. [50]. The influence of welding force can be accounted for with this proposed technique and should be accounted for in RSW process models.

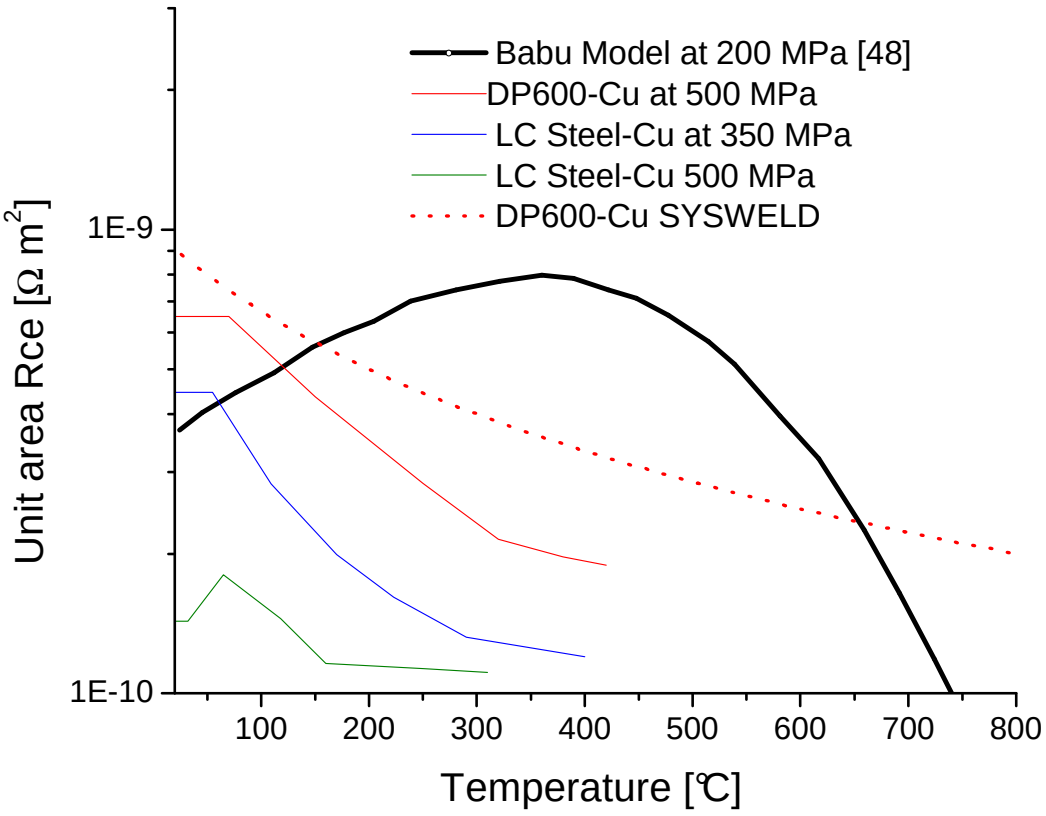

Figure 4.19: Comparison of simulated results of uncoated steels at the E/S interface using numerical optimization procedure with literature.

Babu et al. [48] also proposed a peak due to the competitive nature of bulk material resistance and Rce. An increasing Rce may also be due to difficulty in asperity deformation in the lower temperature ranges, which would increase the constriction resistance effects. The peak in the modelled curve is located at a higher temperature than the proposed curve with the numerical optimization procedure.

Regarding DP600, the proposed curve is compared to the input curve from SYSWELD. Although the interfacial pressure is not given, these curves share similar starting and ending resistance values, although the temperature of flattening for the proposed curve is lower than the input Rce curve from SYSWELD. More exact comparisons can be made with knowledge of the interfacial pressure.

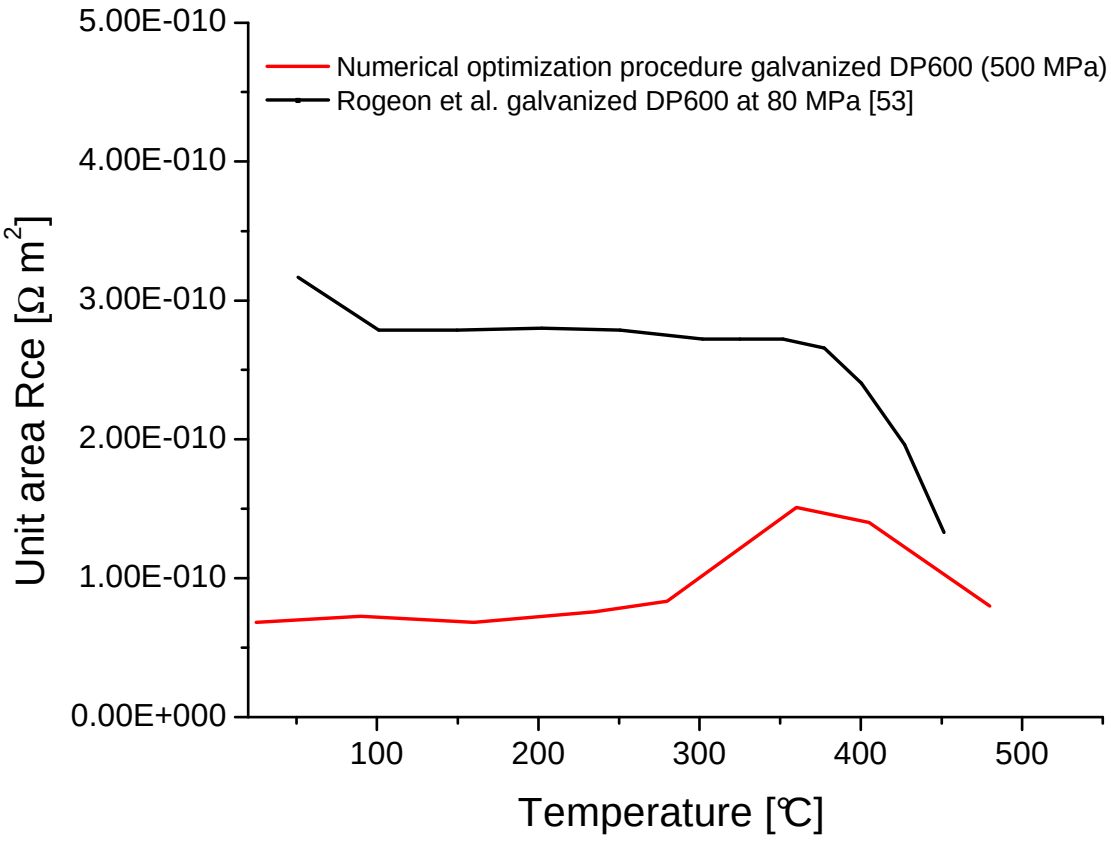

Figure 4.20: Numerically determined Rce at the E/S interface for galvanized DP600 steel with comparison to literature.

4.6.2 Galvanized DP600 steel

A galvanized, DP600 steel, as shown in Table 2.1, was also analyzed in this work to determine the influence of the base metal on the Rce curve. Figures 4.20 and 4.21 show results of the numerical optimization procedure for determining the Rce curve performed on galvanized, DP600 steel at the E/S and S/S interface, respectively. Unlike that for galvanized low carbon steel, the Rce for this material at the E/S interface was measurable and was compared to results from literature. The reason for the presence of Rce for this material could be related to the presence of a harder base with higher yield stress in DP600 steel. This proposed Rce curve has an increasing trend until a peak is reached before the melting of the coating, similar to that of the galvannealed material. The peak was discovered at lower temperature values at the S/S interface compared to that of literature.

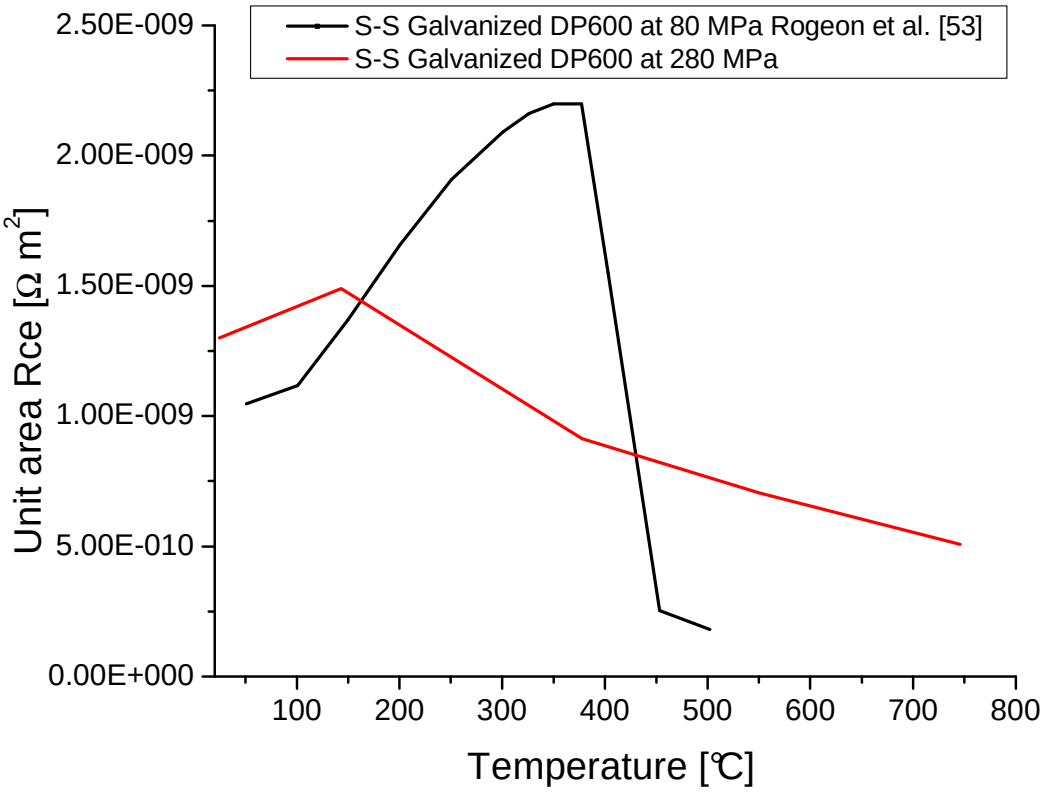

Figure 4.21: Numerically determined Rce at the S/S interface for galvanized DP600 steel with comparison to literature.

4.8 Simulation results with new Rce curves: coated DP600

A RSW thermal simulation was performed with the newly proposed Rce curves for galvanized DP600 steel and compared to an experimental cross section. The results are compared to experiment and shown in Figure 4.22, with the experimental and simulated fusion zone estimated in red. The size and shape of the molten zone are in good agreement with the experimental data. The radii of the heat affected zones are also similar, although the shape of the simulated heat affected zone is noticeably different. This could be due to the simulation procedure, where electrode sink-in was not considered in the analysis. Thus, the electrode radius remained constant and the outer edge of the electrode was not able to conduct heat away from the weld, resulting in the simulated shape of the heat affected zone.

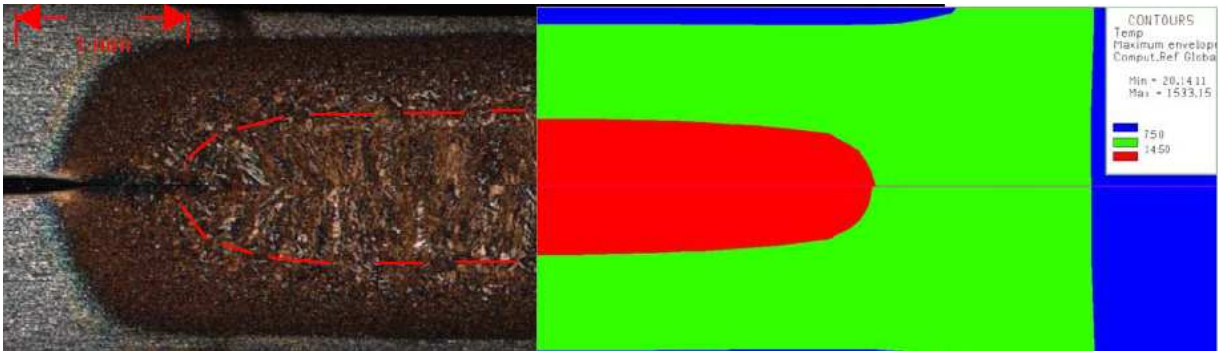

Figure 4.22: Results from a RSW simulation using new Rce curves for galvanized DP600 steel

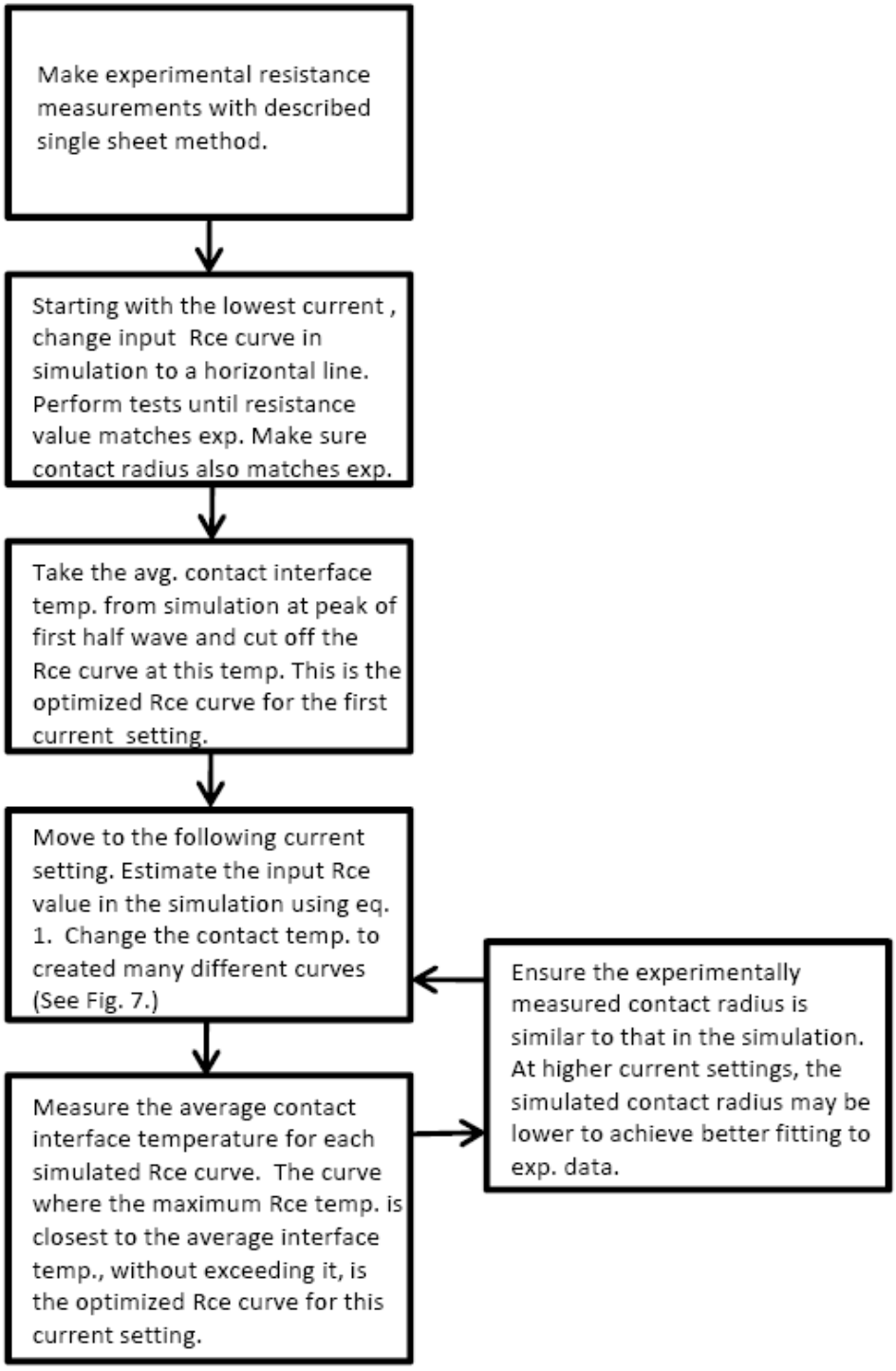

Figure 4.23: Flow chart of proposed numerical optimization technique

4.9 Summary and conclusions

A numerical optimization procedure was proposed to estimate the unit area Rce as a function of temperature at the E/S and S/S interfaces during RSW for different material combinations using an experimental-cum-theoretical approach. A summary of the procedure is given in Figure 4.23. In this procedure, FEM was first used to separate the contribution of the bulk material resistance from the total resistance. This, combined with in-situ experimental total resistance data, allowed for the estimation of the unit area Rce value in the following current step. Then, a trial and error approach was taken to optimize the interfacial temperature in the unit area Rce curve, which allowed for good matching of simulated and experimental total resistance data. The following conclusions were made in the analysis:

- The estimated Rce curve for galvannealed materials at the E/S and S/S interface was found to be increasing until a peak was reached at higher temperatures just before the melting point of the coating. This increase Rce trend was previously proposed in literature but not universally accepted for zinc coated steels.
- The Rce for galvanized and electrogalvanized low carbon steel at the E/S interface was found to be negligible. However, this may be dependent on the base material, as experiments with galvanized DP600 proved otherwise. The Rce curve for galvanized and electrogalvanized materials at the S/S interface was found to have decreasing characteristics. The Rce values for these two coating were also found to be the same.
- A peak in the Rce curve was also found for copper-low carbon steel contact, a result which was determined to be dependent on the interface pressures and was only found at higher interface pressures. The interface pressure has a large influence on the shape of the Rce curve and should be considered in all process models.
- The results of the newly propose technique for measuring the Rce at both interfaces were compared to experimentally measured curves from literature with varying results. It is postulated that in some cases, the curves in literature do not represent the actually curve present during real welding conditions. RSW simulation with the newly proposed curves were performed and compared to an experimental cross section with very good agreement.

Overall, the results of this dissertation represent an alternative method for estimating the unit area Rce curve as a function of interface temperature. Although the FEM program SYSWELD was used in an unconventional way during the analysis, it still enabled for reasonable estimations of the interface temperature. Even if the interface temperature is not calculated, the experimental technique can be used to determine the influence of surface characteristics on the Rce which allows for a better understanding of important process factors such as weld diameter, weldability lobes, product repeatability, welding current ranges, and electrode wear.

Appendix A: Overview of the newly developed spot welding interface

The new spot welding interface, which deals with the pre-processing, creation and modification of a spot welding simulation project, will now be described as well as the important improvements made to the old interface. The previous SYSWELD spot welding advisor had two possibilities to investigate the coupling at the E/S interface: weak and strong coupling option. In the weak coupling option, the thermal analysis is performed during the current application and then the mechanical analysis is first performed at the end of the current application. In the strong coupling option, the mechanical analysis is coupled with thermal analysis during the current application, which accounts for the electrode sink-in and evolution of contact radius at the E/S interface. The new interface allows for easy integration of user defined electrical, thermal and mechanical coupling parameters to change the iteration time and electrode contact radius at the E/S and S/S interfaces.

The spot welding advisor in SYSWELD is a SIL (SYSWORLD interface language) interface to manage the pre-processing, processing and post-processing of spot welding simulation in SYSWELD [79]. A comparison of the input dialogue sequence between the old and new interface can be seen in Figure A1. The sequence of definition of the required data for the pre-processing was restructured, modified and extended, which allowed for a more user friendly modification of the important calculation parameters. The input dialogue now consists of six main groups: file management, meshing, material and contact resistances, electrical load, mechanical load, and calculation parameter.

In addition to the old dialogue it is now possible to select the type of applied current: alternating current (AC), direct current (DC) or user defined current function from an external file (defined by simplified FORTRAN). Furthermore, the time function of the mechanical load can be imported from an external input file with a time-force table. In the last, newly added dialogue window, as seen in Figure A2, the user can define main calculation parameters. There are four analysis options the user can choose: thermal analysis, thermal analysis with a subsequent mechanical calculation respectively weak coupling, strong coupling pressure controlled, and strong coupling distance controlled. Each option will now be briefly described.

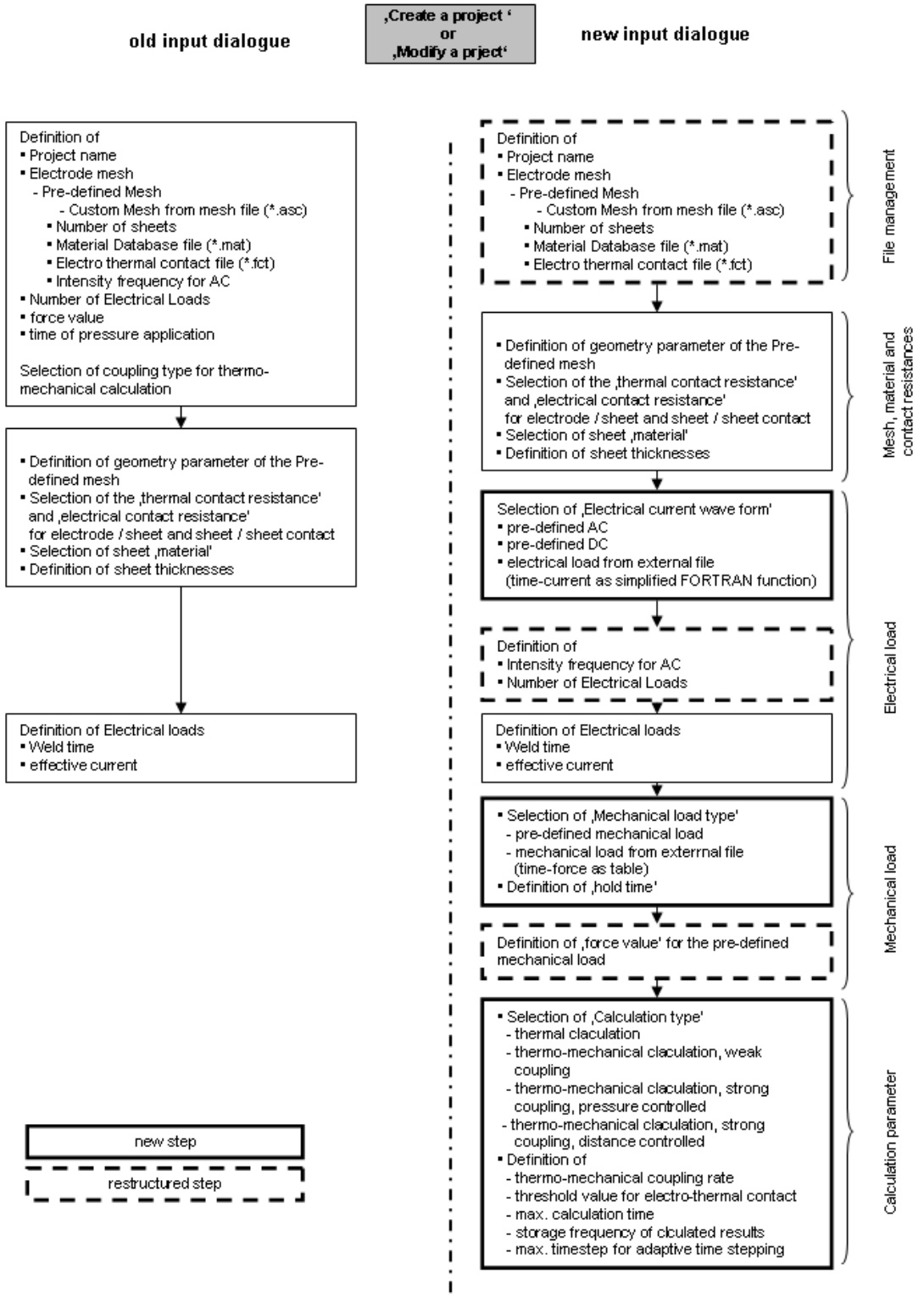

Figure A1: Input dialogue sequence of old and new spot welding interface

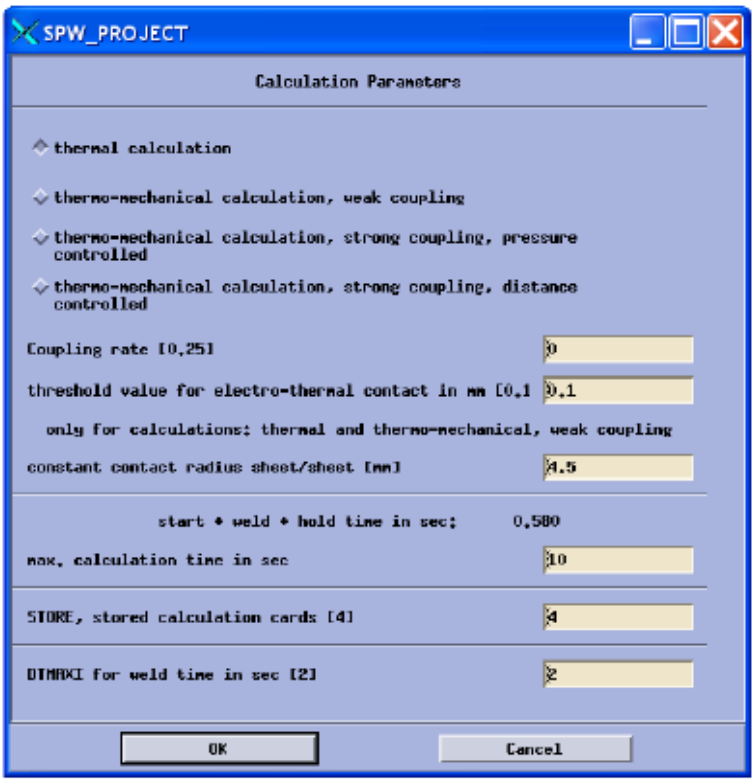

Figure A2: Dialogue window from newly created RSW interface used for definition of important calculation and contact parameters

A1.1 Calculation options

For the electro-thermal calculations, the electro-thermal contact is established if the distance between the opposing surface elements is lower than a user defined threshold value at the E/S interface. At the S/S interface the radius value can be input into the dialogue box and does not change with welding time.

For the weak coupled thermo-mechanical calculation, subsequent to the thermal calculation a mechanical calculation is carried out at the end of the current application.

For the strong coupled thermo-mechanical calculation, pressure controlled, the electro-thermal contact surface (E/S contact radius) is recalculated and defined from the mechanical contact surface (all nodes having a normal contact force difference of zero) at each coupling step with a threshold value of zero. In this simulation option, the threshold value is not significant in the determination of the E/S electrical contact surface, rather the maximum pressure along the interface. Hence the user defined contact radius in not significant.

For the strong coupled thermo-mechanical distance controlled simulations, the electro-thermal contact is established similar to the thermal analysis. If the distance between the opposing surface elements is lower than a threshold value, there is electro-thermal contact.

In addition to the analysis options, it is possible to define and alter the following parameters:

- coupling rate (and iteration time respectively) for the strong coupled simulations
- maximum calculation time respectively the cooling time after the removal of the electrodes. This option allows saving computation time if you are e.g. only interested in the processes during the welding process and not in the residual stresses after cooling. In the old spot welding advisor, the standard value was 50 seconds.
- storage frequency of the calculated results; of interest for accurate studies of the process parameters especially in the early stages of the weld process
- maximum time step for adaptive time stepping to increase the accuracy and time resolution of the results, especially for only thermal analysis
- threshold value for electro-thermal contact definition of thermal analysis, weak coupled thermo-mechanical analysis and strong coupled thermo-mechanical analysis, distance controlled
- actual contact radius at the S/S interface

In the past, the type of current wave form and the type of analysis were defined in the spw_interface.cmd file, which had to be edited manually. The defined values of the new parameters are added in addition to the spot welding project file (*.spw) for traceability of the simulation and its parameters.

References

1) N. T. Williams and J. D. Parker: Review of resistance spot welding of steel sheets: Part 1: Modelling and control of weld nugget formation, International Materials Review, 2004, 49, 2, 45-77.

2) ASM Handbook, Vol. 6: Welding, Brazing, and Soldering, ASM International, Materials Park, OH, 1993, 833.

3) E. Feulvarch, P. Rogeon, V. Robin, G. Sibilia, and J. M. Berfheau: Resistance spot welding process: Experimental and numerical modeling of the weld growth mechanisms with consideration of contact conditions, Numerical Heat transfer, Part A, 2006, 49, 345-367.

4) M. Janota and H. Neumann: Share of spot welding and other joining methods in automobile production, Welding in the World, 2008, 52, 12-16.

5) P. Howe and S. Kelley: A comparison of the resistance spot weldability of bare, hot-dipped, galvannealed, and electrogalvanized DQSK sheet steels, Society of Automotive Engineers, Inc. Doc. 880280, 1988.

6) ISO Standard FDIS 14327, Resistance welding: Procedure for determining the weldability lobe for resistance spot, projection, and seam welding, Geneva, Switzerland, 2001.

7) A. R. Marder: The Metallurgy of Zinc-Coated steel, Progress in Materials Science, 2000, 45, 5, 193-271.

8) F. E. Goodwin, editor: Zinc-based steel coating systems: production and performance, Warrendale, PA, TMS, 1990.

9) G. Krauss and D. K. Matlock, editors: Zinc-based steel coating systems: metallurgy and performance, Warrendale, PA, TMS, 1994.

10) S. Ritsche and J. Strutzenberger: Punktschweißen von FVZ Öberflächen, Internal report number B3E_F_128_2002_B.

11) J. Mackowiak and N. R. Short: Metallurgy of zinc coatings, International Metallurgical Reviews, 1979, 1.

12) C. E. Jordan and A. R. Marder: A model for galvanneal morphology development, The Physical Metallurgy of Zinc Coated Steels, Warrendale, PA, TMS, 1994, 197.

13) ASM Handbook, Vol. 2: Properties and Selection: Nonferrous Alloys and Special-Purpose Materials, ASM International, Materials Park, OH, 1990, 527-542.

14) R. Holliday, J. D. Parker, and N. T. Williams: Relative contribution of electrode tip growth mechanisms in spot welding zinc coated steels, Welding in the World, 1996, 37, 4, 186-193.

15) R. J. Holliday, J. D. Parker, and N. T. Williams: Electrode deformation when spot welding coated steels, Welding in the World, 1995 35, 3, 160-164.

16) J. D. Parker, N. T. Williams, and R. J. Holliday: Mechanisms of electrode degradation with spot welding coated steels, Science and Technology of Welding and Joining, 1998, 3, 2, 65-74.

17) C. L. White, F. Lu, M. Kimchi, and P. Dong: Resistance spot welding electrode wear on galvannealed steels, Zinc-Based Steel Coating Systems: Production and Performance, 1998, 219-228.

18) T. Dupuy, A. Clad, H. Oberle, and Y. Bienvenu: The degradation of electrodes by spot welding zinc coated steels, IIW Doc. N III-1107-98, 2004, 1-12.

19) P. Howe and C. Chen: Coating composition effects and other factors affecting electrode life of hot-dipped galvanized and galvannealed steels, Sheet Metal Welding Conference IX, Sterling Heights, MI, 2000

20) J. E. Gould and W. Peterson: Analytical modelling of electrode wear occurring during resistance spot welding, Science and Technology of Welding and Joining, 2008, 13, 3, 248-253.

21) F. Lu and P. Dong: Model for estimating electrode face diameter during resistance spot welding, Science and Technology of Welding and Joining, 1999, 4, 5, 285-289.

22) F. W. McBee: Electrode tip life in spot welding galvanized steels, Welding Journal, 1950, 10, 531s-535s.

23) P. Howe and S. C. Kelley: Coating weight effect on the resistance spot weldability of electrogalvanized sheet steels, Welding Journal, 1998, 12, 271s-280s.

24) E. Baril and G. L'Esperance: Studies of the morphology of the Al-rich interfacial layer formed during the hot dip galvanizing of steel sheet, Metallurgical and Materials Transactions A, 1999, 30A, 681-695.

25) Y. Morimoto, E. McDevitt, and M. Meshii: Characterization of the Fe-Al inhibition layer formed in the initial stages of hot-dip galvannealing, ISIJ International, 1997, 37, 9, 906-913.

26) M. Koester, B. Schuhmacher, and D. Sommer: The influence of the zinc content on the lattice constants and structure of the intermetallic compound Fe_2Al_5, Steel Research, 2001, 72, 9, 371-375.

27) M. L. Giorgi, J. B. Guillot, and R. Nicolle: Theoretical model of the interfacial reactions between solid iron and liquid zinc-aluminum alloy, Journal of Materials Science, 2005, 40, 2263-2268.

28) P. Toussaint, L. Segers, R. Winand, and M. DuBois: Mathematical modelling of Al take-up during the interfacial inhibition layer formation in continuous galvanizing, ISIJ International, 1998, 38, 9, 985-990.

29) H. Matasuda, Y. Matasuda and M. Kabasawa: Effects of aluminum in the Zn coating on electrode life in welding galvanized steel sheet, Welding International, 1996, 10, 8, 605-613.

30) J. Faderl, W. Maschek, and J. Strutzenberger: Spangle size and aluminum pick up for hot dip zinc coatings, Galvatech ’95 conference proceedings, 675-685.

31) Y. Hisamatsu: Galvatech ’89, Proceedings on the International conference on zinc and zinc alloy coated steel sheet, ISIJ, Tokyo, 1989, 3.

32) C. E. Jordan and A. R. Marder: Fe-Zn phase formation in interstitial-free steels hot-dip galvanized at 450°C Part 1: 0.00 wt % Al-Zn baths, Journal of Materials Science, 1997, 32, 5593-5602.

33) C. E. Jordan and A. R. Marder: Effect of substrate grain size on Iron-Zinc reaction kinetics during hot-dip galvanizing, Metallurgical and Materials Transactions A, 1997, 28A, 2683-2694.

34) P. Howe and C. Chen: The effects of coating composition, substrate, and welding machine on the resistance spot welding behavior of hot-dip galvanized and galvannealed sheet steels, Society of Automotive Engineers, 1999-01-3213.

35) K. Nishiguchi and K. Matsuyama: Influence of current wave form on nugget formation phenomena when spot welding thin steel sheets, Welding in the World, 1987, 25, 11/12, 222-244.

36) W. Li, E. Feng, D. Ceranec, and G. Grzadzinski: Energy consumption in AC and MFDC resistance spot welding, Sheet Metal Welding Conference XI, 2004, Sterling Heights, MI.

37) P. Podrzaj, I. Polajnar, J. Diaci, and Z. Kariz: Influence of welding current shape on expulsion and weld strength of resistance spot welds, Science and Technology of Welding and Joining, 2006, 11, 3, 250-254.

38) T. Dupuy and D. Fardoux: Spot welding zinc-coated steels with medium frequency direct current, Sheet Metal Welding Conference IX, Sterling Heights, MI., 2000.

39) K. Matsuyama: Polarity effects in DC resistance spot welding, Sheet Metal Welding Conference X, Sterling Heights, MI., 2002.

40) H. Tang, W. Hou, S. J. Hu, H. Y. Zhang, Z. Feng, and M. Kimchi. Influence of welding machine mechanical characteristics on the resistance spot welding process and weld quality, Welding Journal, 2003, 5, 116s-124s.

41) T. Dupuy: Influence of the mechanical characteristics of a pedestal spot welding machine, Proceedings of the 4th International Seminar on Advances in Resistance Welding, Wels, 2006, 62-74.

42) H. Tang, W. Hou, S. J. Hu, and H. Zhang: Force characteristics of resistance spot welding of steels, Welding Journal, 2000, 7, 175s-183s.

43) P.S. James, H. W. Chandler, and J. T. Evans: The effect of mechanical loading on the contact resistance of coated aluminum, Materials Science and Engineering, A, 1997, 230, 194-201.

44) E. Crinon and J. T. Evans: The effect of surface roughness, oxide film thickness, and interfacial sliding on the electrical contact resistance of aluminum, Materials Science and Engineering A, 1998, 242, 121-128.

45) M. Rashid, S. Fukumoto, and J. B. Medley. Influence of lubricants on electrode life in resistance spot welding of aluminum alloys, Welding Journal, 2007, 3, 62s-70s.

46) Holm, R. 1967. Electrical Contact Handbook, Springer-Verlag, Berlin, 4th Edition.

47) J. A. Greenwood: Constriction resistance and the real area of contact, British Journal of Applied Physics, 1966, 17 1621-1632

48) S. S. Babu, and M. L. Santella: Empirical model of effects of pressure and temperature on electrical contact resistance of metals, Science and Technology of Welding and Joining, 2001, 6, 3, 126-132.

49) F. J. Studer: Contact resistance in spot welding, Welding Journal, 1939, 18, 10, 374s-380s.

50) F. P. Bowden, F. R. S. and J. B. P. Williamson: Electrical conduction in solids, Influence of the passage of current on the contact between solids, Proceedings of the Royal Society A, 1958, 246, 1-12.

51) D. Richard, M. Fafard, R. Lacroix, P. Clery, and Y. Maltais: Carbon to cast iron electrical contact resistance constitutive model for finite element analysis, Journal of Materials Processing Technology, 2003, 132, 119-131.

52) E. Thieblemont: PhD Thesis, Institute National Polytechnique de Lorraine, Nancy, 1992.

53) P. Rogeon, P. Carre, G. Sibilia, and G. Saindrenan: Characterization of electrical contact conditions in spot welding assemblies, Journal of Materials Processing Technology, 2008, 195, 1-3, 117-124.

54) G. Le Meur, B. Bourouga, and T. Dupuy: Measurement of contact parameters at electrode/sheet interface during resistance spot welding process, Science and Technology of Welding and Joining, 2003, 8, 6,415-122.

55) P. Rogeon, R. Raoelison, P. Carre, and F. Dechalotte: A microscopic approach to determine electrothermal contact conditions during resistance spot welding process, Journal of Heat Transfer, 2009, 131.

56) G. Le Meur, B. Bourouga, and J. Bardon: Microscopic analysis of interfacial electrothermal phenomena-definition of a heat generation factor, International Journal of Heat and Mass Transfer, 2006, 29, 387-401.

57) M. Vogler and S. Sheppard: Electrical contact resistance under high loads and elevated temperatures, Welding Journal, 1993, 6, 231s-238s.

58) P. H Thornton, A. R. Kraus and R. G. Davies: Contact resistances in spot welding, Welding Journal, 1996, 75, 12, 402s-412s.

59) DVS2929-3: Method for determining the transition resistance-application for steels, 2010.

60) W. F. Savage, E. F. Nippes, and F. A. Wassell: Static contact resistance of series spot welds, Welding Journal, 1977, 11, 365s-370s.

61) S. A. Gedeon, C. D. Sorensen, K. T. Ulrich, and T. W. Eagar: Measurement of dynamic electrical and mechanical properties of resistance spot welds, Welding Journal, 1987, 12, 378s-385s.

62) Q. Song, W. Zhang, and N. Bay: An experimental study determines the electrical contact resistance in resistance welding, Welding Journal, 2005, 73s-76s.

63) Y. Cho and S. Rhee: Quality estimation of resistance spot welding by using pattern recognition with neural networks, IEEE Transactions on Instrumentation and Measurement, 2004, 53, 2, 330-334.

64) O. Kasap. Electronic Materials and Devices. McGraw-Hill Companies, 102-119, 2002.

65) EN ISO 5821: Resistance welding – Spot welding electrode caps, 2009.

66) EN ISO 5182: Resistance welding – Materials for electrodes and ancillary equipment, 2009.

67) M. D. Gugel, C. L. White, M. Kimchi, and K. Pickett: The effect of aluminum content in HDG coating on the wear of RSW electrodes, Sheet Metal Welding Conference VI, 1994.

68) ESI Group, Spot Welding Advisor User's Manual, Paris, France, 2004.

69) Z. Feng, S. S. Babu, M. L. Santella, B. W. Riemer, and J. E. Gould, An incrementally coupled electrical-thermal-mechanical model for resistance spot welding, Proceedings of the 5th International Conference on Trends in Welding Research, Pine Mountain, Georgia, 1998.

70) Y. P. Lei and Y. W. Shi: Numerical treatment of the boundary conditions and source terms on a spot welding process with combining buoyancy-marangoni-driven flow, Numerical Heat Transfer B, 1994, 26, 4, 455-471.

71) J. M. Bergheau, G. Manglialenti, and F. Boitout: Contribution of numerical simulation to the analysis of heat treatment and surface hardening processes, Proceedings of Heat Treatment 98, 18th ASM Heat Treating Society Conference and Exposition, Rosemont, IL, 1998.

72) J. B. Leblond and J. C. Devaux: A new kinetic model for anisothermal metallurgical transformations in steel including effect of austenite grain size, Acta Metallurgical, 1984, 32, 1, 137-146.

73) D. P. Koistinen and R. E. Marburger: A general equation prescribing the extent of austenite-martensite transformation in pure Fe-C alloys and plain carbon steels, Acta Metallurgical, 1959, 7, 417-426.

74) Y. Ueda and T. Yamakawa: Analysis of thermal elastic-plastic stress and strain during welding by finite element method, Transactions of Japanese Welding Society, 1971, 12, 2, 90–100.

75) K. J. Bathe: Finite Element Procedure, Prentice-Hall, Englewood Cliffs, NJ, 1996.

76) V. Robin, A. Sanchez, T. Dupuy, J. Soigneux, and J. M. Bergheau: Numerical simulation of spot welding with special attention to contact conditions, Mathematical Modelling of Weld Phenomena 6, The Institute of Materials, London, 2002.

77) E. Feulvarch, V. Robin, and J. M. Bergheau: Resistance spot welding simulation: a general finite element formulation of electrothermal contact conditions, Journal of Materials Process Technology, 2004, 153-154, 436-441.

78) C. Srikunwong, T. Dupuy, and Y. Bienvenu: Influence of electrical-thermal physical properties in resistance spot welding modelling, Mathematical Modelling of Weld Phenomena 7, The Institute of Materials, London, 2005.

79) ESI Group, SYSTUS Heat Transfer Reference Manual, Paris, France, 2007.

80) W. Ernst, M Galler, R. Vallant, N. Enginger, and C. Sommitsch: Modification of coupling parameters for a more accurate numerically coupled simulation of the resistance spot welding process. Proceedings of SYSWELD Forum, Weimar, Germany, 2009.

81) M. Galler, W. Ernst, R. Vallant, and N. Enzinger: A Simulation based determination of the electrical contact resistance, Mathematical Modelling of Weld Phenomena 9, TU Graz, 2010, p. 883-900.

82) Z. Han, J. Orozco, J. E. Indacochea, and C. H. Chen: Resistance spot welding: A heat transfer study, Welding Journal, 1989, 9, 363s-371s.

83) D. J. Browne, H. W. Chandler, J. T. Evans, P. S. James. J. Wen, and C. J. Newton: Computer simulation of resistance spot welding in aluminum: part II, Welding Journal, 1995, 12, 417s-422s.